



HAL
open science

New preparation of ceramic coatings by low-pressure plasma spray

Chen Song

► **To cite this version:**

Chen Song. New preparation of ceramic coatings by low-pressure plasma spray. Materials Science [cond-mat.mtrl-sci]. Université Bourgogne Franche-Comté, 2018. English. NNT : 2018UBFCA009 . tel-01876692

HAL Id: tel-01876692

<https://theses.hal.science/tel-01876692>

Submitted on 18 Sep 2018

HAL is a multi-disciplinary open access archive for the deposit and dissemination of scientific research documents, whether they are published or not. The documents may come from teaching and research institutions in France or abroad, or from public or private research centers.

L'archive ouverte pluridisciplinaire **HAL**, est destinée au dépôt et à la diffusion de documents scientifiques de niveau recherche, publiés ou non, émanant des établissements d'enseignement et de recherche français ou étrangers, des laboratoires publics ou privés.

SPIM

Thèse de Doctorat



école doctorale sciences pour l'ingénieur et microtechniques

UNIVERSITÉ DE TECHNOLOGIE BELFORT-MONTBÉLIARD

Potentialité de préparation de revêtements en céramiques par la projection plasma sous basse pression

SONG Chen

N° d'ordre:

Année : 2018

Université de Technologie de Belfort-Montbéliard

Ecole doctorale Sciences physiques pour

l'Ingénieur et Microtechniques

THESE

Présentée pour obtenir le grade de

Docteur de l'Université de Technologie de Belfort-Montbéliard

en Sciences pour l'Ingénieur

**Potentialité de préparation de revêtements
céramiques par la projection plasma sous basse
pression**

SONG Chen

Soutenance le 25 Juin 2018

Devant le jury

Rapporteurs

M. Michel VARDELLE, Professeur des universités, Université de Limoges

M. Gang JI, Chargé de recherche au CNRS, HDR, Université de Lille

Examineur

Mme. Isabelle SOCHET, Professeur des universités, INSA Centre Val de Loire

M. Christian CODDET, Professeur des universités, Université de Technologie de Belfort-Montbéliard

M. Hanlin LIAO, Professeur des universités, Université de Technologie de Belfort-Montbéliard

Acknowledgement

Firstly, I sincerely thank the members of the jury for participating in my graduation defense. They reviewed the thesis very seriously and gave me a lot of valuable comments. Besides, I would like to extend my sincere gratitude to the supervisor, Professor Han-lin LIAO, for my great benefit from his profound knowledge, innovative idea as well as rigorous research attitude in the field of thermal spray. Furthermore, I gratefully acknowledge to Professor Ke-song ZHOU and Professor Min LIU for their instructive advice and useful suggestions on the experiment.

Secondly, I would like to thank all my colleagues in the LERMPS laboratory (UTBM, Belfort, France) and Guangdong Institute of New Materials (GINM, Guangzhou, China). Particularly, I want to appreciate the technical team in the LERMPS laboratory, especially thank the help of Christian ADAM and Charles BERNAGE when building up the low-pressure spraying system with a new bi-cathode plasma torch. Besides, I would like to give thanks to the thermal spraying group in the GINM, especially for the experimental assistance from Chun-ming DENG, Shao-peng NIU, and Zi-qian DENG in China. Moreover, I want to appreciate Emmanuelle ARCENS, Min KUANG, and Yun YE for the XRD, SEM, and EBSD analysis.

Thirdly, I am very grateful for the financial support provided by the China Scholarship Council. Without this funding, I cannot complete the Ph.D. research work in France.

Last but not least, my thanks would go to my parents and fiancée for their loving considerations and great confidence in me all through these years.

Thank you very much!

CONTENTS

CONTENTS	I
List of Figures	IV
List of Tables	X
Introduction	XI
Chapter 1 Literature Review	1
1.1 Low-Pressure Plasma Spray.....	1
1.1.1 Introduction to Atmospheric Plasma Spray	1
1.1.2 Origin and Evolution of Low-Pressure Plasma Spray.....	4
1.1.3 Principle of Low-Pressure Plasma Spray	6
1.1.4 Characteristics of Low-Pressure Plasma Spray.....	7
1.1.5 Plasma Torches Used in Low-Pressure Plasma Spray	10
1.1.6 Coatings Prepared by Low-Pressure Plasma Spray	13
1.2 Low-Pressure Suspension Plasma Spray.....	18
1.2.1 Introduction to Suspension Plasma Spray	18
1.2.2 Why Use Low-Pressure Suspension Plasma Spray.....	28
1.2.3 Challenge for the Plasma Torch Used In Low-Pressure Suspension Plasma Spray	29
1.2.4 Coating Prepared by Low-Pressure Suspension Plasma Spray.....	30
1.3 Low-Pressure Reactive Plasma Spray.....	33
1.3.1 Introduction to Reactive Plasma Spray	33
1.3.2 Why Use Low-Pressure Reactive Plasma Spray	36
1.3.3 Coatings Prepared by Low-Pressure Reactive Plasma Spray	37
1.4 Objectives of the Thesis	40
References	42
Chapter 2 Experimental and Testing Equipment	53
2.1 Experimental Equipment.....	53
2.1.1 LPPS Equipment	53
2.1.2 PS–PVD Equipment.....	58

2.2 Testing Equipment.....	59
2.2.1 Optical Emission Spectroscopy	59
2.2.2 X-Ray Diffraction.....	62
2.2.3 Optical and Scanning Electron Microscopy	64
2.2.4 Nanoindentation	65
References.....	67
Chapter 3 Elaboration and Characterization of YSZ Coatings Prepared by	
Low-Pressure Plasma Spray.....	69
3.1 Introduction	69
3.2 Experimental Procedures	71
3.2.1 Spraying Material	71
3.2.2 Coating Preparation	71
3.2.3 Characterization.....	73
3.3 Results and Discussions	73
3.3.1 Plasma Jet Diagnostics	73
3.3.2 SEM Analysis.....	75
3.3.3 XRD Analysis.....	84
3.3.4 Nanoindentation Results.....	86
3.4 Conclusions	88
References	89
Chapter 4 Elaboration and Characterization of YSZ Coatings Prepared by	
Low-Pressure Suspension Plasma Spray.....	93
4.1 Introduction	93
4.2 Experimental Procedures	95
4.2.1 Spraying Material	95
4.2.2 Suspension Preparation	96
4.2.3 Coating Preparation	97
4.2.4 Characterization.....	98
4.3 Results and Discussion	99
4.3.1 YSZ Coatings with the Set 2,3,4 Parameters.....	99
4.3.2 YSZ Coatings with the Set 1 and Set 5 Parameters.....	102

4.4 Conclusions	117
References	118
Chapter 5 Elaboration and Characterization of TiN Coatings Prepared by Low-Pressure Reactive Plasma Spray.....	123
5.1 Introduction	123
5.2 Experimental Procedures	125
5.2.1 Spraying Material.....	125
5.2.2 Coating Preparation.....	125
5.2.3 Characterization	127
5.3 Results and Discussions	127
5.3.1 Plasma Jet Diagnostics	127
5.3.2 XRD Analysis	128
5.3.3 Microstructural Analysis.....	129
5.3.4 Nanoindentation Results	131
5.4 Conclusions	132
References	134
Conclusions and Perspectives.....	137
Abstract	141
Résumé	143

List of Figures

Figure 1.1 Schematic of APS using a DC plasma torch: the plasma gas coming from the base of the cathode is heated by the arc between the cathode and the anode, then the sprayed-particles are injected into the plasma jet and transported to the substrate to form a coating [6]...... 2

Figure 1.2 Schematic of a typical plasma-sprayed coating. 3

Figure 1.3 LPPS equipment from the early 1970s [12]...... 4

Figure 1.4 The plasma jets for different LPPS processes and representative micrographs of the resulting coatings [15]...... 6

Figure 1.5 Schematic diagram of the LPPS process. 7

Figure 1.6 Radial profiles of the jet velocity (A) and temperature (B) taken at an axial distance of 775 mm for 10 and 2 mbar. Plasma conditions: 1500 A, Ar–H₂ (100/3 slpm) [19]. 9

Figure 1.7 Radial profiles of the particle velocity (A) and temperature (B) taken at an axial distance of 975 mm for 10 and 1.5 mbar. Plasma conditions: 1500 A, Ar–H₂ (100/3 slpm) [19]. 9

Figure 1.8 Images of the plasma jets expanding at different pressures (a) 95 kPa (950 mbar/APS), (b) 5 kPa (50 mbar/VPS/LPPS), and (c) 0.1 kPa (1 mbar/PS–PVD) [17]. 8

Figure 1.9 3D model and parts of the F4-VB torch (1: Cathode F4, 2: Rear gun body, 3: O-ring, 4: Cover, 5: Front lock ring, 6: Powder injector, 7: Injector mounting ring, 8: Plug nut, 9: Flat spring, 10: Rear securing ring, 11: Anode, 12: Anode holder, 13: Middle gun body, 14: Gas distribution ring, 15: Insulating intermediate body, 16: Cap screw, 17: Insulating set screw) [29]. 11

Figure 1.10 3D model and parts of the O3CP torch (1: Anode retainer, 2: Powder injector, 3: O-ring, 4: Anode, 5: Cap screw, 6: Middle gun body, 7: Gas distribution ring, 8: Anode extension, 9: Insulator housing, 10: Cathode, 11: Electrode holder, 12: Retainer ring, 13: Rear gun body, 14: Plasma gas fitting, 15: Closure stud, 16: Negative insulator boot, 17: Negative insulator nut) [30]. 12

Figure 1.11 LPPS family bridges the gap between PVD, CVD and conventional thermal spray technologies [31]. 13

Figure 1.12 CoNiCrAlY coatings prepared by (a) axial plasma spray, (b) HVOF, (c) VPS [35]. 14

Figure 1.13 Cross section of a dense and gas-tight YSZ electrolyte layer between the porous electrodes for SOFCs [36]...... 15

Figure 1.14 The microstructures of columnar YSZ coatings: (a) EB–PVD, (b) PS–PVD [31]...... 16

Figure 1.15 The microstructure of columnar TBC top coating (a) on the leading edge of the turbine blade, (b) on the pressure face of the turbine blade [31].	16
Figure 1.16 (a) The PS-CVD process exhibits a broad, diffuse plasma jet with high enthalpy and high ionization rates. Note the injection ring for gaseous precursors. (b) A film of SiO _x , approximately 2.5 μm thick, applied to a silicon substrate using PS-CVD in less than 3 min coating time [15].	17
Figure 1.17 Evolution of crystals size at thermal spraying of different feedstocks: (a) agglomerated nano-particles, and (b) conventional micro-particles [49].	19
Figure 1.18 Schematic diagram of the SPS [50].	20
Figure 1.19 Schematic of suspension droplet treatment when containing attrition-milled particles [56].	21
Figure 1.20 Schematic of suspension droplet treatment when containing aggregates and agglomerates [56].	22
Figure 1.21 Schematic of particle trajectories within the plasma jet core and its fringes with the corresponding coating [57].	23
Figure 1.22 Stokes number for in-flight particles and the effect on deposition [58].	23
Figure 1.23 Fracture of a YSZ coating obtained by SPS [69].	25
Figure 1.24 Cross sections (left side) and surfaces (right side) microstructures of YSZ coatings with 2.5 wt.% solid phase deposited on different substrates prepared by (a) sandblasting, sample; (b) laser treatment, sample; (c) grinding [70].	26
Figure 1.25 Cross sections (left side) and surfaces (right side) microstructures of YSZ coatings with 10 wt.% solid phase deposited on different substrates prepared by (a) sandblasting, sample; (b) laser treatment, sample; (c) grinding [70].	27
Figure 1.26 Dependence of droplet impact on substrate asperity on droplet momentum [74].	27
Figure 1.27 Schematic of the Northwest Mettech Axial III torch with central injection [76].	30
Figure 1.28 The configuration of the tri-cathode torch with the axial injection mode [82].	31
Figure 1.29 The cross-sectional morphologies of YSZ coatings deposited by LP-SPS at 150 mm: (a) low magnification, (a') high magnification [45].	31
Figure 1.30 Surface morphology of YSZ coatings deposited by LP-SPS at 150 mm [45].	31
Figure 1.31 A diagram of the cathode and anode plasma gun setup [83].	32

Figure 1.32 The presence of unmelted YSZ particles in the cross section image [83].	32
Figure 1.33 Schematic diagram of RPS without reaction gas.	33
Figure 1.34 Schematic diagram of RPS with reaction gas [88].	34
Figure 1.35 (a) The cross-sectional morphology of the RPS TiN coating, (b) XRD pattern of the RPS TiN coating [98].	35
Figure 1.36 (a) XRD patterns for coatings sprayed with given chamber pressures, (b) variation of nitrogen content in collected particles with spraying pressure [92].	36
Figure 1.37 Cross section of the coating (left), XRD of the powders and the coating (right) [87].	37
Figure 1.38 SEM observations of Ti-TiN coating cross sections elaborated by VLPPS [100].	38
Figure 1.39 XRD pattern obtained on Ti coating and Ti-TiN coatings elaborated by VLPPS from different spraying parameters [100].	38
Figure 1.40 XRD pattern of the FeAl coating [101].	39
Figure 1.41 (a) Cross-sectional microstructure of the FeAl coating, (b) high-magnification image of the black frame in (a); (c) and (d) the corresponding Al and Fe elements mapping in (b) [101].	39
Figure 2.1 The LPPS system made by the LERMPS [3].	54
Figure 2.2 The 3D model (top) and three-view drawing (bottom) of the bi-cathode plasma torch designed for LPPS.	57
Figure 2.3 The MultiCoat™ hybrid plasma-coating system at GINM [4].	59
Figure 2.4 Jobin-Yvon Triax 190 optical emission spectrometer.	61
Figure 2.5 Schematic of the OES measuring process in the LPPS system [6].	61
Figure 2.6 (a) Destructive and (b) reinforcing interactions between x-rays and the crystalline material. Reinforcement occurs at angles that satisfy Bragg's law [10].	62
Figure 2.7 (a) Diagram of a diffractometer, showing powder sample, incident, and diffracted beams (b) The diffraction pattern obtained from a sample of gold powder [10].	63
Figure 2.8 The schematic of the load-displacement curve for an instrumented nanoindentation test [15].	65
Figure 2.9 The schematic of the unloading process showing parameters characterizing the contact geometry [15].	65
Figure 3.1 Morphology of Metco 6700 YSZ powder.	71

Figure 3.2 Schematic diagram of the YSZ coatings prepared by the LPPS system.	72
Figure 3.3 The plasma jets with YSZ powders using Set 1 (left) and Set 2 (right).	74
Figure 3.4 The OES patterns of pure plasma jets using Set 1 (left) and Set 2 (right).	75
Figure 3.5 The OES patterns of plasma jets with YSZ powders using Set 1 (left) and Set 2 (right).	75
Figure 3.6 The surface morphologies of YSZ coatings deposited at different spraying distances of (a) 350 mm, (b) 450 mm, and (c) 550 mm using Set 1. Images (a')–(c') show the corresponding high magnification.	76
Figure 3.7 The cross-sectional morphologies of YSZ coatings deposited at different spraying distances of (a) 350 mm, (b) 450 mm, and (c) 550 mm using Set 1. Images (a')–(c') show the corresponding high magnification.	78
Figure 3.8 The cross-sectional morphologies of YSZ coatings deposited on the substrate parallel to the plasma jet at different spraying distances of (a), (a') 350 mm; (b), (b') 450 mm; and (c), (c') 550 mm using Set 1.	79
Figure 3.9 The surface morphologies of YSZ coatings deposited at different spraying distances of (a) 350 mm, (b) 450 mm, and (c) 550 mm using Set 2. Images (a')–(c') show the corresponding high magnification.	80
Figure 3.10 The cross-sectional morphologies of YSZ coatings deposited at different spraying distances of (a) 350 mm, (b) 450 mm, and (c) 550 mm using Set 2. Images (a')–(c') show the corresponding high magnification.	82
Figure 3.11 The surface and cross-sectional morphologies of YSZ coatings deposited on the substrate parallel to the plasma jet at different spraying distances of (a), (a') 350 mm; (b), (b') 450 mm; and (c), (c') 550 mm using Set 2.	83
Figure 3.12 The XRD patterns of YSZ powder and as-sprayed coatings deposited using Set 1 (left) and Set 2 (right).	84
Figure 3.13 The percentages of the M and T' phase in the YSZ powders and the as-sprayed coatings deposited by Set 1 and Set 2.	86
Figure 3.14 The crystallite sizes of the YSZ powders and the as-sprayed coatings deposited by Set 1 and Set 2.	86

Figure 3.15 The load-displacement curves of the cross-sectional YSZ coatings deposited by Set 1 (left) and Set 2 (right).	87
Figure 3.16 The hardness and Young's modulus of the cross-sectional YSZ coating deposited by Set 1 (left) and Set 2 (right).	88
Figure 4.1 The morphology of the YSZ powders.	95
Figure 4.2 The experimental system of suspension plasma spraying YSZ at low pressure.	98
Figure 4.3 The plasma jets with YSZ suspensions at the spraying distance of 450 mm using Set 2,3,4.	101
Figure 4.4 The YSZ coatings deposited at the spraying distance of 450 mm using Set 2,3,4.	101
Figure 4.5 The plasma jets with YSZ suspensions using Set 1 and Set 5.	102
Figure 4.6 The OES patterns of pure plasma jets using Set 1 and Set 5.	103
Figure 4.7 The OES patterns of plasma jets with YSZ suspension using Set 1 and Set 5.	104
Figure 4.8 The surface morphologies of YSZ coatings deposited at different spraying distances of (a) 180, (b) 200, and (c) 220 mm using Set 1. Images (a')–(c') show the corresponding high magnification.	105
Figure 4.9 The cross-sectional morphologies of YSZ coatings deposited at different spraying distances of (a) 180, (b) 200, and (c) 220 mm using Set 1. Images (a')–(c') show the corresponding high magnification.	107
Figure 4.10 The surface morphologies of YSZ coatings deposited at different spraying distances of (a) 350, (b) 450, and (c) 550 mm using Set 5. Images (a')–(c') show the corresponding high magnification.	108
Figure 4.11 The cross-sectional morphologies of YSZ coatings deposited at different spraying distances of (a) 350, (b) 450, and (c) 550 mm using Set 5. Images (a')–(c') show the corresponding high magnification.	110
Figure 4.12 The cross-sectional morphologies of YSZ coatings on the (a) side and (b) back of the substrate deposited at the spraying distance of 450 mm using Set 5. Image (b') is the EDS result of (b).	111
Figure 4.13 The XRD patterns of YSZ powders and sprayed coatings deposited at different spraying distances using Set 1 (top) and Set 5 (bottom).	112

Figure 4.14 The contents of the T and T' phase in the YSZ powders and the sprayed coatings deposited at different spraying distances using Set 1 and Set 5.	113
Figure 4.15 The crystallite sizes of the YSZ powders and the sprayed coatings deposited at different spraying distances using Set 1 and Set 5.	114
Figure 4.16 The load-displacement curves of cross-sectional YSZ coatings deposited by Set 1 and Set 5.	116
Figure 4.17 The hardness and Young's modulus of cross-sectional YSZ coatings deposited by Set 1 and Set 5.	116
Figure 5.1 The morphology of the Ti powders.	125
Figure 5.2 The schematic diagram for preparing TiN coating using LP-RPS.	126
Figure 5.3 The OES patterns of the plasma jet with Ti powders at 500 and 900 mm	128
Figure 5.4 The XRD patterns of the raw Ti powders and as-sprayed coatings.	129
Figure 5.5 The cross-sectional morphologies of the coatings at (a) 500mm and (b) 900 mm. The corresponding inverse pole figure (IPF) + image quality (IQ) maps at (c) 500mm and (d) 900 mm.	131
Figure 5.6 Load-displacement curves of the TiN coatings at 500 mm, 900 mm and the Ti-6Al-4V substrate.	132

List of Tables

<i>Table 2.1 Parts list of the bi-cathode plasma torch</i>	58
<i>Table 2.2 Technical specifications for the Jobin-Yvon Triax 190.</i>	61
<i>Table 3.1 Chemical composition of Metco 6700 YSZ powder.</i>	71
<i>Table 3.2 LPPS operating parameters.</i>	72
<i>Table 4.1 The chemical composition of YSZ powders.</i>	96
<i>Table 4.2 The main characteristics of water and ethanol.</i>	96
<i>Table 4.3 The different spraying parameters for SPS YSZ coatings.</i>	98
<i>Table 5.1 Chemical composition of the Ti powders.</i>	125
<i>Table 5.2 LP-RPS parameters.</i>	126
<i>Table 5.3 Mechanical properties of the TiN coatings and the Ti-6Al-4V substrate.</i>	132

Introduction

As an emerging thermal spray technology, the low-pressure plasma spray (LPPS) offers the opportunity to bridge the thickness gap between traditional thermal spray and thin film coating processes. Moreover, the LPPS offers the ability to create the uniform coatings with different microstructures. The deposition can be achieved not only from liquid splats but also from nano-sized clusters and the vapor phase. To further develop the potential of the LPPS process, this study attempted to combine the LPPS technology with another two thermal spraying processes: suspension plasma spray (SPS) and reactive plasma spray (RPS). With the novel integrated processes, the nanoscale coatings with unique microstructures and high performance were expected to achieve. In detail, this study included the following contents:

- First of all, a new bi-cathode plasma torch was designed for the LPPS process based on the commercial F4 type plasma torch. The new plasma torch had an axial injection mode and its maximum input power could reach 81 kW. With different feeding carriers, either the suspension (containing submicron particles) or the micro-sized powders could be injected into the plasma center under low pressure. As a result, the heat and mass transfer between the plasma jet and the sprayed materials could be enhanced, which was beneficial to achieve high-quality coatings with high deposition efficiency.
- Secondly, by using this axial bi-cathode plasma torch, the yttria-stabilized zirconia (YSZ) coatings were deposited under different low pressures from the agglomerated YSZ powder and the YSZ suspension. Different spraying parameters were carried out to study the effects on the plasma jet as well as the morphology, phase structure, mechanical property of the YSZ coatings.
- Furthermore, by applying the O3CP plasma torch, the titanium nitride (TiN) coatings were *in-situ* synthesized on the Ti-6Al-4V alloys using the reactive plasma spray under very low pressure. The influences of the spraying distances on the vaporization degree, the nitriding effect and the microstructure of the TiN

coatings were discussed. Besides, the mechanical properties of the TiN coatings and the Ti-6Al-4V substrate were investigated.

- Finally, the results of the YSZ and TiN coatings prepared under low pressure were concluded. Moreover, the perspectives of the future work on LPPS process were proposed.

CHAPTER 1

Literature Review

Chapter 1 Literature Review

1.1 Low-Pressure Plasma Spray

1.1.1 Introduction to Atmospheric Plasma Spray

1.1.1.1 Brief Description of Atmospheric Plasma Spray

The atmospheric plasma spray (APS) process, invented around 1960, has been one of the most versatile and widely used thermal spray processes. This process can deposit a relatively thick coating (a few hundred micrometers up to a few millimeters thick) on a substrate to improve its surface performance, such as thermal barrier, wear resistance, corrosion resistance, biological activity and electromagnetic effects [1]. Compared with other thermal spray processes, APS has its unique advantages include [2]:

- It can produce a plasma jet with a higher temperature over 8000 K at atmospheric pressure, allowing the melting of any powder materials [1]. Particularly, APS is suitable for spraying coatings of refractory metals and ceramics, including ZrO_2 , B_4C , and tungsten. Such a wide range of optional materials enables APS to prepare a variety of coatings and meet different needs.
- It can spray powders with a broader particle size range, typically 5–100 μ m, compared with HVOF spraying. In addition, many types of substrate material, including metals, ceramics, plastics, glass, and composite materials can be coated using APS.
- The velocity of sprayed-powders can reach 200–500 m/s, making the quality of coatings better than other conventional thermal processes such as flame or arc spraying. Moreover, the spraying process is simple to operate and has a high deposition rate (up to a few kilograms per hour) [3].

In consequence, APS has been commonly used in many industrial areas including aeronautics, industrial gas turbines, automotive, materials mining and processing, biomedical and electronics [3,4].

1.1.1.2 Principle and Coating Characteristics of Atmospheric Plasma Spray

The schematic diagram of the APS using a DC plasma torch is illustrated in Figure 1.1. The DC plasma torch consists of a cathode (usually a rod or button-type design) and a cylindrical anode nozzle. With the plasma gases (Ar, H₂, N₂ or He) injected at the base of the cathode, DC power is applied to the cathode. Then a high-frequency arc is ignited between the cathode and the anode. The powerful arc strips the gas molecules of their electrons to form a plasma plume. As the unstable plasma ions recombine back to the gaseous state, enormous energy is released. Thus a high-temperature plasma jet with high velocity is formed. The peak temperatures at the torch exit can be 12000–15000 K, and the peak velocities range from 500 to 2500 m/s (subsonic velocities at these temperatures), depending on the torch design, plasma gases, and spraying parameters [5]. After that, the sprayed powders are delivered radially into the hot plasma jet. The angle of injection can be either perpendicular to or with a small angle against the plasma jet. Then the injected powders will be heated, accelerated by the plasma jet, and form a coating.

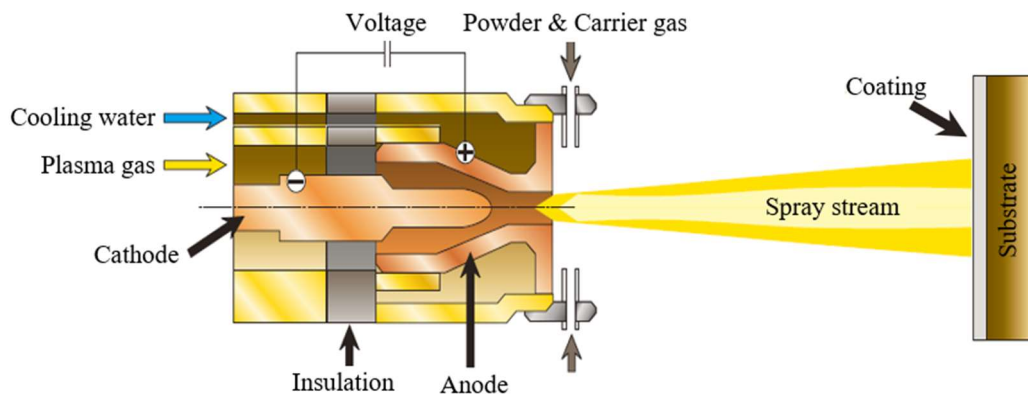


Figure 1.1 Schematic of APS using a DC plasma torch: the plasma gas coming from the base of the cathode is heated by the arc between the cathode and the anode, then the sprayed-particles are injected into the plasma jet and transported to the substrate to form a coating [6].

However, due to the plasma jet has large gradients of both temperature and velocity, the injected powders with different particle sizes have various trajectories. Consequently, their melting states can be divided into fully melted, partially melted, and unmelted. When the fully melted powders strike the substrate, they encounter a significant deformation and cooling. Thus, well-flattened pancakes or flower lamellae (often called “splats”) are produced and tightly adhere to the substrate or previously deposited coating. The individual splat is generally thin (1 to 20 μm) and with a very high cooling rate ($>10^6$ K/s for metals). In contrast, when the partially melted or unmelted powders impact the substrate, they cannot be well-flattened and closely stick the substrate or previously deposited coating, which increases the porosity of resulting coating (typically between 0 and 10%). The porosity has the size of a few micrometers and will lower the deposit’s cohesive strength.

Furthermore, when the metallic powders are sprayed by APS, they easily react with O_2 or N_2 in the air during flight, leading to the formation of oxide or nitride films on the surface of particles. As they impact the substrate, these films will be fractured and included in the coating as oxide or nitride inclusions [7]. A schematic of a typical plasma-sprayed coating is presented in Figure 1.2.

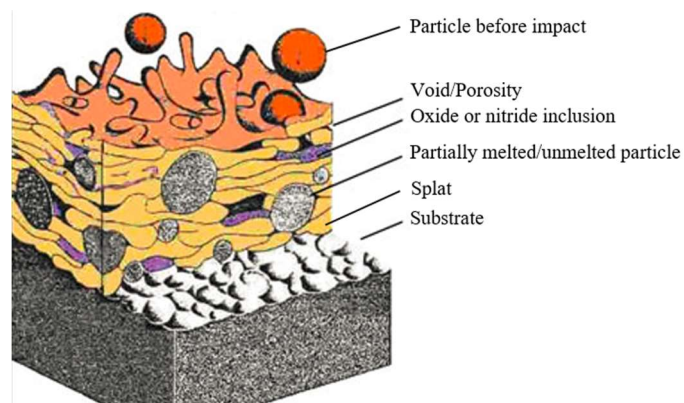


Figure 1.2 Schematic of a typical plasma-sprayed coating.

1.1.2 Origin and Evolution of Low-Pressure Plasma Spray

With a continually expanding range of applications, traditional APS coatings cannot meet the service requirements in harsh environments, such as higher temperatures of operation, wear and corrosion under extreme conditions, and longer lifespan of parts and devices. This is mainly because there are numerous voids, oxide or nitride inclusions existing in their lamellar microstructure. Moreover, due to the small spray spot, traditional APS process is not suitable for depositing coatings over a large area.

To overcome these problems and enhance the coating quality, a low-pressure plasma spray (sometimes called vacuum plasma spray) process was first proposed by Eric Muehlberger in 1974 [8]. The technique puts the APS process inside a low-pressure chamber (see Figure 1.3), which enables to produce extremely dense coatings with virtually no oxide inclusions. A few years later, the LPPS technique was used to deposit hot corrosion-resistant coatings [9] and pure coatings of copper [10] or tantalum [11] for electronics applications.

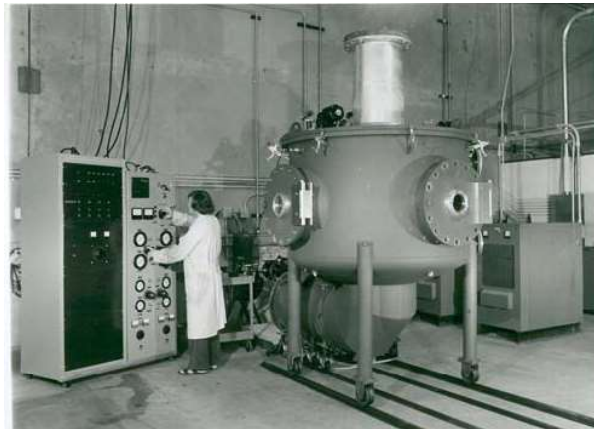


Figure 1.3 LPPS equipment from the early 1970s [12].

In 1998, Eric Muehlberger explored a modified low-pressure plasma spray system to rapidly deposit uniform thin coatings of metallic oxides or other materials over large substrates, on the order of a square meter [13]. The modified LPPS system was operated at higher than average power levels and much lower than normal chamber pressures (<1000 Pa). Under these conditions, new forms of deposition are

possible. Since that time, a new process called very low-pressure plasma spray (VLPPS) has officially joined the thermal spray community.

Nowadays, the big family of LPPS technologies can be divided into two parts depending on the different spraying pressures. One is the traditional VPS/LPPS process operated under the pressure of 5–20 kPa. The other is the VLPPS process running under the lower pressure, typically less than ~800 Pa. According to the use of different feedstock materials, the VLPPS process can be further divided into three processes [14]:

- *Plasma Spray–Thin Film (PS–TF)*, a process using fine powder feedstock similar to conventional plasma spray but at significantly reduced chamber pressures, which makes it possible to coat thin and dense layers that are predominantly deposited from molten or semi-molten droplets.
- *Plasma Spray–Physical Vapor Deposition (PS–PVD)*, a process using specially designed agglomerated powder feedstock, which is vaporized by a high power plasma torch, with deposition occurring primarily or entirely from the vapor phase.
- *Plasma Spray–Chemical Vapor Deposition (PS–CVD)*, a process using liquid or gas precursors as feedstock material, which is deposited from the vapor phase and thus allows the production of CVD-like coatings (<10 μm) at higher deposition rates.

Figure 1.4 illustrates the plasma jets for the different LPPS process technologies and representative micrographs of the resulting coatings. Compared with the more expensive and much slower PVD and CVD processes, the LPPS process offers possibilities to produce reliable coatings on large areas at rapid deposition rates. Therefore, the LPPS coating process has been successfully used over the past 40 years and continues to enjoy worldwide acceptance today.

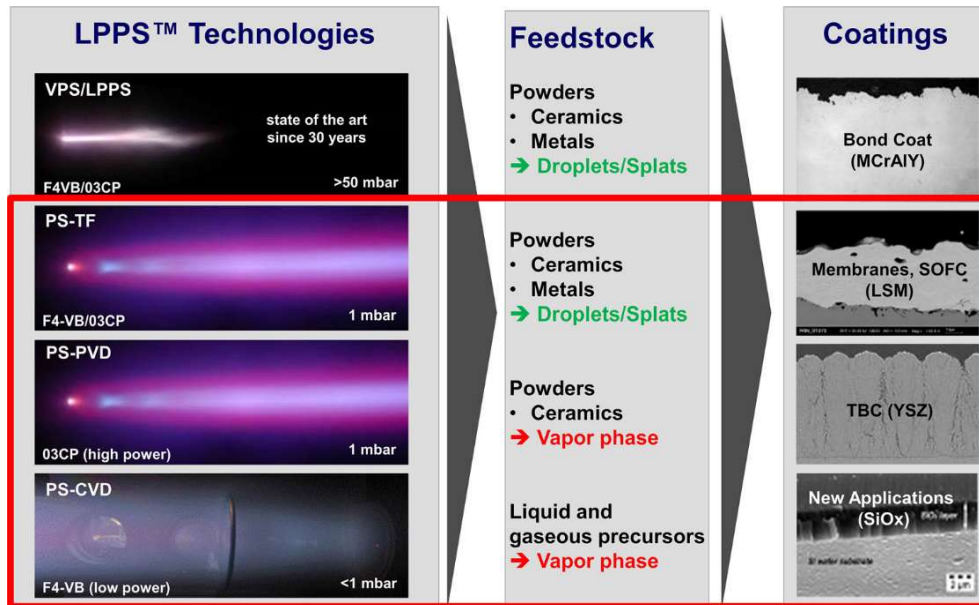


Figure 1.4 The plasma jets for different LPPS processes and representative micrographs of the resulting coatings [15].

1.1.3 Principle of Low-Pressure Plasma Spray

Generally, the LPPS process uses the DC plasma torch. Thus its principle of plasma generation is the same as that of the APS process. However, the LPPS equipment and process are more complicated than those of APS. Figure 1.5 represents the schematic of LPPS installation. The LPPS system needs a sizeable water-cooling chamber with the associated pumping installation to provide a controlled atmosphere of both low pressure and gas content. To adapt to the low-pressure environment, the robotic system needs an additional pressurizer and water-cooling device for moving the torch. Besides, all cables inside the chamber should be shielded to resist the heat radiation and particle flux. Before starting the spray process, the chamber is pumped down to a pressure of a few Pascal and then backfilled with high purity argon and pumped down again to the desired operating pressure. Moreover, a transfer arc can be generated between the torch (as an anode) and the substrate (as a cathode), which makes it possible to clean the substrate surface of its oxide layer, leading to an excellent bonding by diffusion when spraying metals or alloys onto metallic substrates [5].

All of these required features raise the cost of a VPS system significantly, and this increase can be an order of magnitude compared to an APS system with comparable power. For this reason, the applications for LPPS-coated parts are different from those of APS-coated parts and are generally limited to high added value components. Even so, the LPPS process is still considered simpler, faster and more economical than the PVD and CVD processes at similar power usage [5].

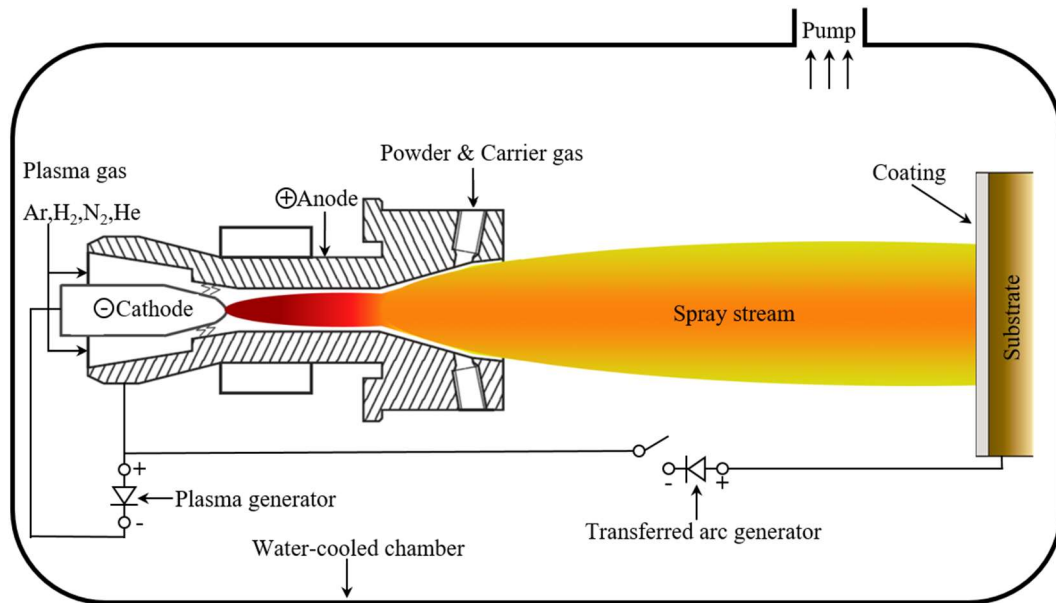


Figure 1.5 Schematic diagram of the LPPS process.

1.1.4 Characteristics of Low-Pressure Plasma Spray

Owing to the weak collision and large dimensions under low pressure, the plasma jet of LPPS exhibits quite different properties from APS, which will influence the coating structures and properties [16]. The detailed characteristics of LPPS are as follows:

1) The controlled atmosphere is able to prevent oxidation or contamination of the powders and deposits in-flight and on the substrate, especially for spraying metal or alloy powders.

2) The plasma jet under low pressure extends to become much wider and longer than that of APS. This expanding effect becomes more pronounced as the pressure decreases. Figure 1.6 shows the different plasma lengths under different pressures.

Compared to the APS (95 kPa), the LPPS operated under 5 kPa enlarges the plasma jet from 50 up to 500 mm in length and from 10 up to 40 mm in diameter. When the pressure decreases to 0.1 kPa, the PS-PVD expands the plasma jet to more than 2 m long and 200–400 mm in diameter. A larger plasma jet results in a bigger spray spot, which makes the particle velocity and temperature more homogeneously distributed over the cross section of the jet. Moreover, the longer plasma jet compensates the insufficient heating capacity and prolongs the heating time of particles, leading to less superheating of the particle surfaces and lower temperature differences between the particle surfaces and the particle centers. Therefore, the particles can be uniformly heated, accelerated and rapidly deposited over large substrates [17,18].

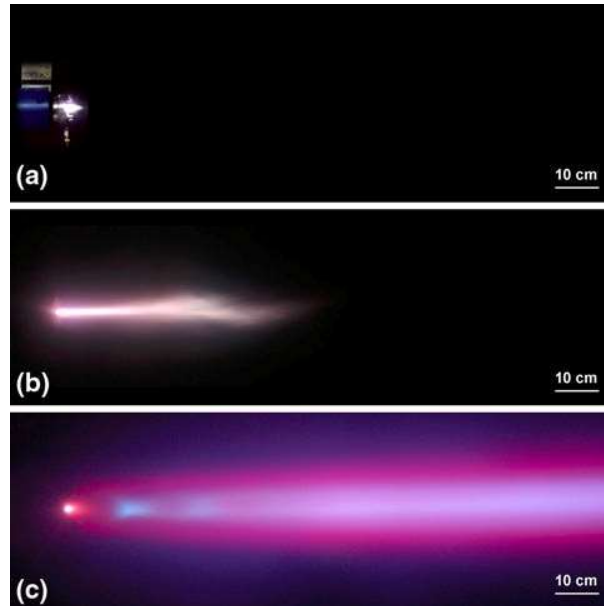


Figure 1.6 Images of the plasma jets expanding at different pressures (a) 95 kPa (950 mbar/APS), (b) 5 kPa (50 mbar/VPS/ LPPS), and (c) 0.1 kPa (1 mbar/PS-PVD) [17].

3) With a decreasing pressure, the plasma jet velocity and temperature of LPPS increase. For example, Figure 1.7 [19] shows that a significant increase in plasma velocity and temperature as the pressure is reduced from 10 mbar to 2 mbar at an axial distance of 775 mm (as measured with an enthalpy probe). However, the decreasing pressure lengthens the mean gas free path thereby lowers the heat and momentum transfer from the plasma to the YSZ particles. As a result shown in Figure 1.8, the

velocity and temperature of the YSZ particle are slightly higher at 10 mbar (as measured with a DPV 2000 system).

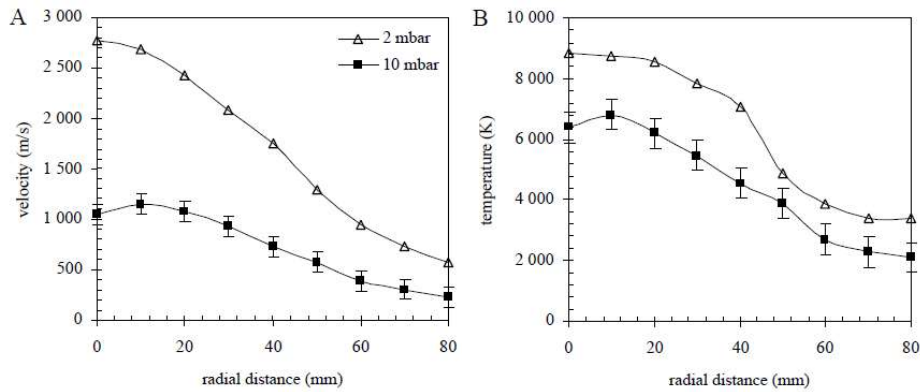


Figure 1.7 Radial profiles of the jet velocity (A) and temperature (B) taken at an axial distance of 775 mm for 10 and 2 mbar. Plasma conditions: 1500 A, Ar-H₂ (100/3 slpm) [19].

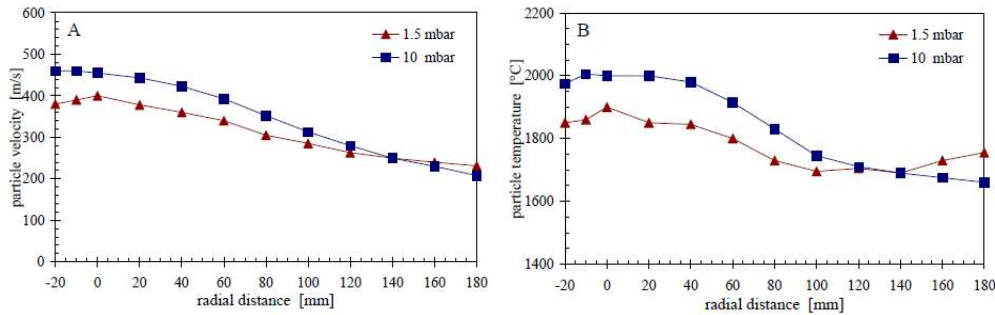


Figure 1.8 Radial profiles of the particle velocity (A) and temperature (B) taken at an axial distance of 975 mm for 10 and 1.5 mbar. Plasma conditions: 1500 A, Ar-H₂ (100/3 slpm) [19].

4) For the low-pressure plasma jet reaching supersonic speeds inside the nozzle, shock diamonds are usually observed outside the nozzle. These shock diamonds lead to sudden velocity reductions and can result in a dispersion of the particle trajectories. The use of a properly designed de Laval nozzle can significantly improve the results by avoiding the shock structures immediately downstream of the anode nozzle exit [20].

5) By adjusting the operating pressure and spraying parameters, LPPS can achieve different microstructural coatings, including lamellar, columnar, or hybrid structures, which are deposited from liquid, gas, or mixed phase, respectively.

1.1.5 Plasma Torches Used in Low-Pressure Plasma Spray

Similar to the APS process, the LPPS process usually employs the DC plasma torch, as described in Section 1.1.3. However, unlike the APS torch that applies a standard anode nozzle with a straight exit, the LPPS torch uses a designed de Laval nozzle with a diverging exit. The different layouts can be distinguished between Figures 1.1 and 1.5. The diverging exit can diminish the plasma shock wave under low pressure, which makes the plasma jet longer and more homogeneous. This increases the particle velocities up to 800–900 m/s (twice as high as with standard torches) and focuses the particle into a direction more parallel to the torch axis [21,22], resulting in a higher deposition efficiency [23]. As a consequence, the torch current and power level can be reduced. In fact, almost all the industrial low-pressure plasma torches use this de Laval nozzle, including the most commonly used F4-VB torch and O3CP torch (Oerlikon Metco, Switzerland). Figure 1.7 and Figure 1.8 show the 3D models and parts of the two torches, respectively.

For the F4-VB torch, it is capable of operating at power levels up to 55 kW by using the maximum current of 700 A [24]. Different types of anode nozzles can be selected to achieve plasma jets with different shapes and lengths, and this gives flexibility for spraying different powders. Besides, the internal diameter of the anode nozzle can be 6, 7 or 8 mm, on which 1–4 powder injectors can be installed to achieve different feeding rates and deposition efficiencies. Based on the above features, the F4-VB torch is ideal to deposit dense coatings for applications in the turbine manufacturing, chemical processing, and medical industries.

For the O3CP torch, it allows operation at high power levels up to 180 kW (3000 A) with a high total gas flow of up to 200 slpm. Several nozzle designs with a straight or curved powder injector are available to optimize process conditions. As a result, a high enthalpy plasma stream with a length of more than 1.5 m and 200–400 mm in diameter will be achieved. At appropriate parameters, it is even possible to evaporate the powder feedstock material, achieving advanced microstructures and non-line-of-

sight deposition under a very low-pressure atmosphere [24]. Moreover, based on the above characteristics, the O3CP torch is suitable for mass production of uniform coatings on a large substrate, even with complex geometries and shadowed areas [25-28].

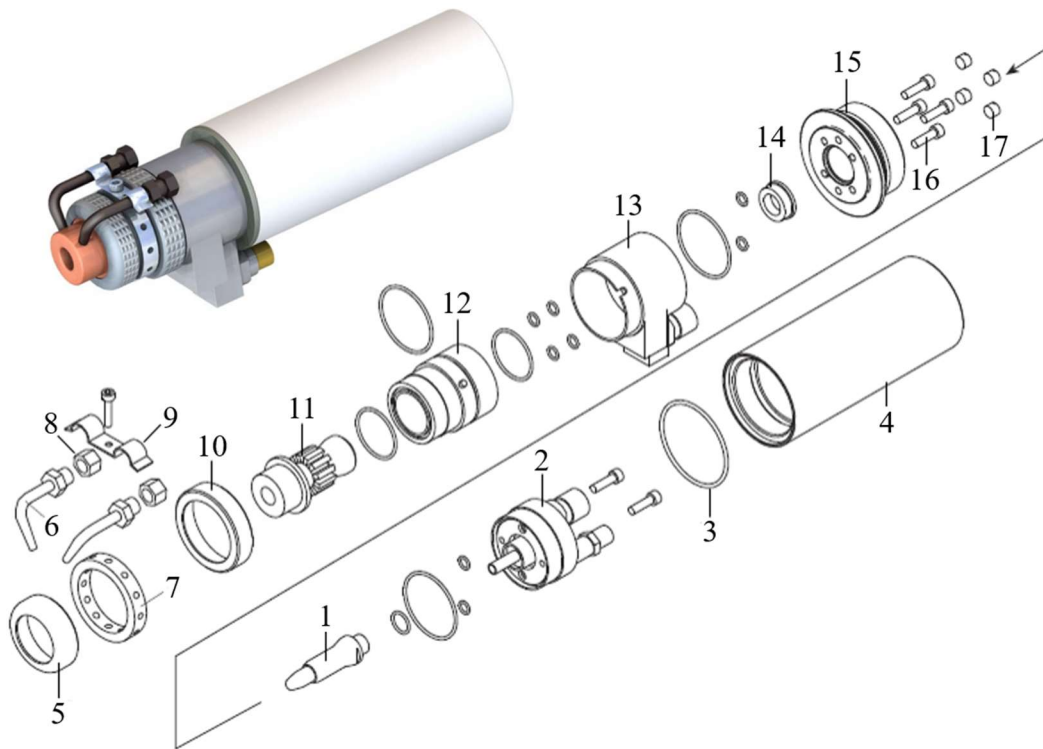


Figure 1.9 3D model and parts of the F4-VB torch (1: Cathode F4, 2: Rear gun body, 3: O-ring, 4: Cover, 5: Front lock ring, 6: Powder injector, 7: Injector mounting ring, 8: Plug nut, 9: Flat spring, 10: Rear securing ring, 11: Anode, 12: Anode holder, 13: Middle gun body, 14: Gas distribution ring, 15: Insulating intermediate body, 16: Cap screw, 17: Insulating set screw) [29].

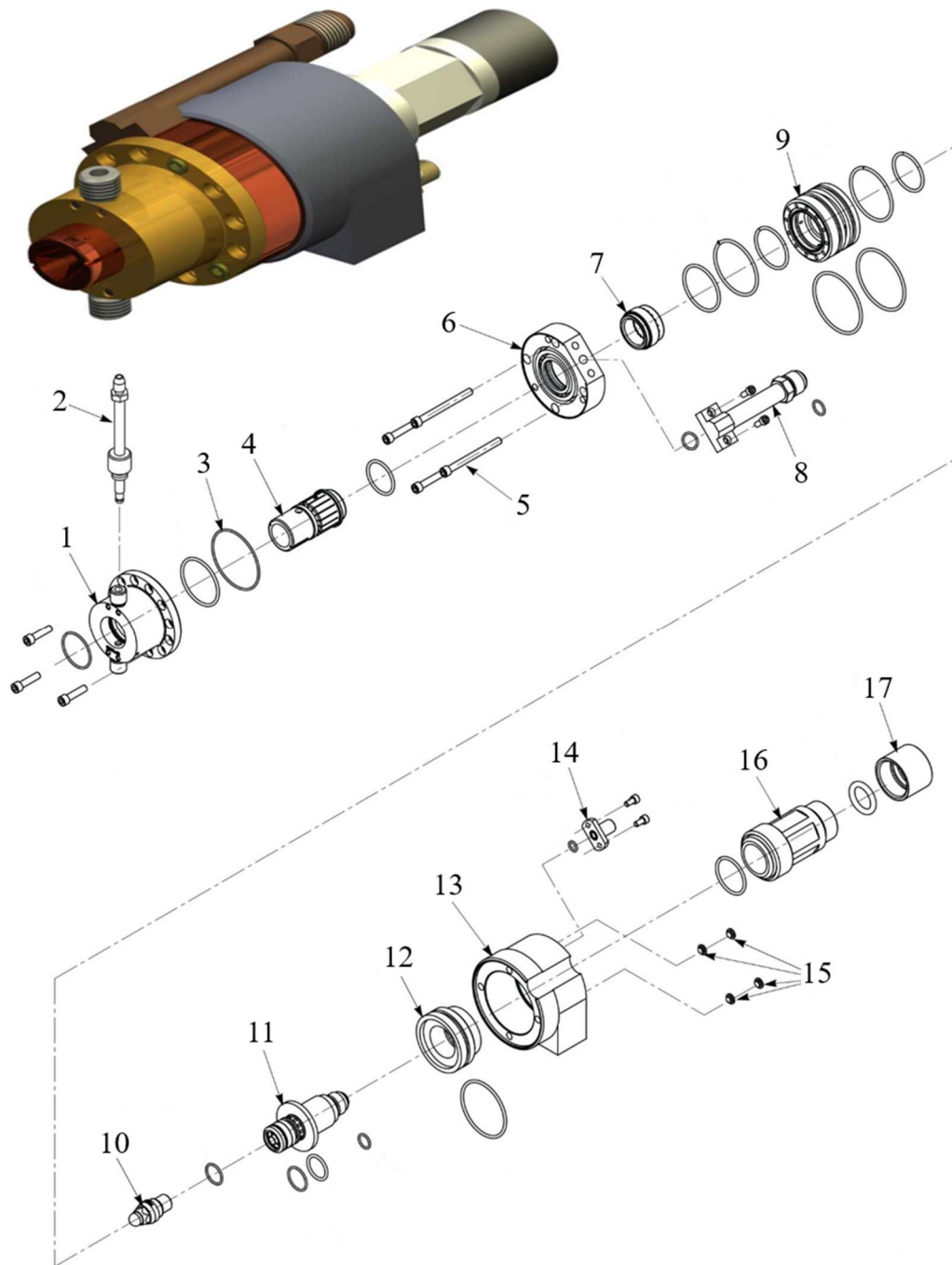


Figure 1.10 3D model and parts of the O3CP torch (1: Anode retainer, 2: Powder injector, 3: O-ring, 4: Anode, 5: Cap screw, 6: Middle gun body, 7: Gas distribution ring, 8: Anode extension, 9: Insulator housing, 10: Cathode, 11: Electrode holder, 12: Retainer ring, 13: Rear gun body, 14: Plasma gas fitting, 15: Closure stud, 16: Negative insulator boot, 17: Negative insulator nut) [30].

1.1.6 Coatings Prepared by Low-Pressure Plasma Spray

The LPPS technologies can rapidly produce uniform coatings over comparatively large areas with thicknesses of 1 to 100 μm . Depending on different torch powers and operating pressures, the coatings can be deposited in different forms, including very fine molten droplets, vapor phase or a mixture of the two. Accordingly, the resulting coatings will have a dense laminar structure, porous columnar structure, or a mixture of them. Therefore, the LPPS technologies offer the capability to bridge the gap between traditional thermal spray coatings and thin film processes such as PVD and CVD [31], as shown in Figure 1.9. The following sections will introduce these coatings prepared by different preparation techniques.

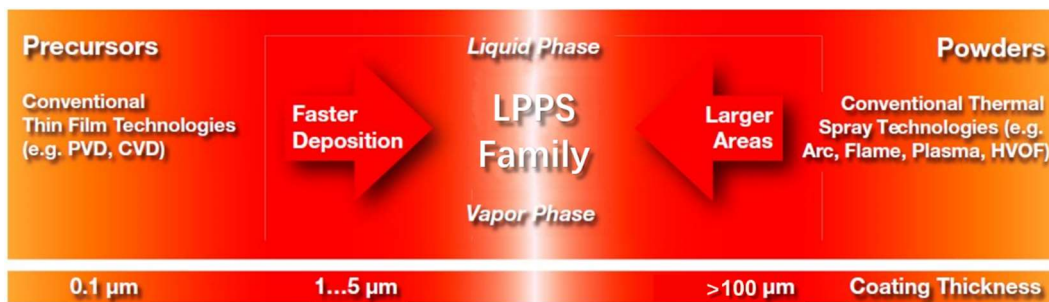


Figure 1.11 LPPS family bridges the gap between PVD, CVD and conventional thermal spray technologies [31].

1.1.6.1 Coatings Prepared by Traditional VPS/LPPS

Traditional VPS/LPPS is operated under pressures of 5–20 kPa and is one of the most suitable processes for depositing coatings with extremely low oxide levels. Its great success is the preparation of bond coats (MCrAlY coatings) for thermal barrier coatings (TBCs) in aero-engines [32-34]. Figure 1.10 compares the CoNiCrAlY coatings obtained with axial plasma spray, HVOF, and VPS processes. All the coatings have laminar structures, which are deposited from the droplets. However, concerning the AxPS and HVOF coatings, the VPS coating has lower porosity, less unmelted particles, and a lower degree of oxidation. Due to the reduced air resistance and oxygen content, the VPS plasma jet is high-speed and the kinetic energy coupled

with the enthalpy of the plasma gives the best compromise for very dense and oxide-free coatings [35].

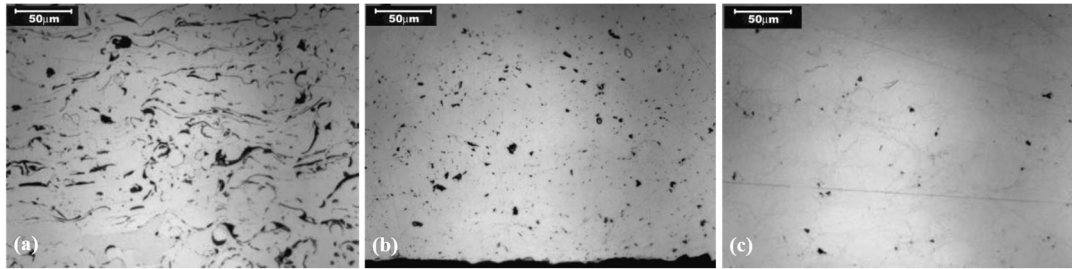


Figure 1.12 CoNiCrAlY coatings prepared by (a) axial plasma spray, (b) HVOF, (c) VPS [35].

1.1.6.2 Coatings Prepared by PS–TF

Similar to the LPPS, the PS–TF process uses powder materials and applies them as classical thermal spray liquid splats onto the substrate. However, the PS–TF is operated under lower pressures, typically between 100–200 Pa. Therefore, the plasma jet of the PS–TF is broader, longer, and faster than that of the LPPS. Therefore, thin and dense metallic or ceramic coatings with thicknesses between 10 and 60 μm can be produced quickly on large substrates. Moreover, the resulting coatings have not only low internal stresses but also exhibit low porosity, with tiny pores that are not interconnected. Due to these advantages, PS–TF is an ideal process to produce gas-tight layers as functional coatings, such as electrolyte coatings used in solid oxide fuel cells (SOFCs) and oxygen transport membranes (OTM) applied in gas separation applications [31,36].

Figure 1.11 shows a cross section of a dense and gas-tight YSZ electrolyte layer prepared by PS-TF. The YSZ layer with a thickness of 26 μm and 2% porosity was obtained. The contact of the anode/electrolyte interface was excellent, while that of the cathode/electrolyte interface still needs improvement. However, this did not affect its excellent cell performance. The cell test at 817°C illustrated that the current density was 1.380 A/cm² at 0.7 V corresponding to a power density of 0.976 W/cm². These values are higher than known from the literature for solid oxide fuel cells with thermally sprayed functional layers [36,37].

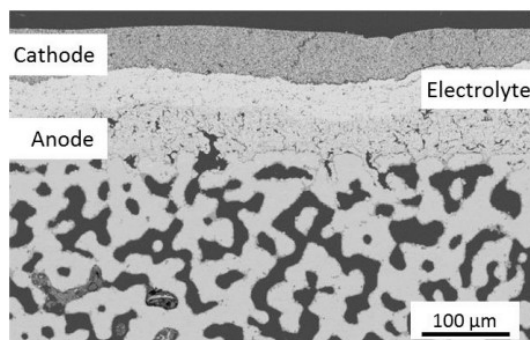


Figure 1.13 Cross section of a dense and gas-tight YSZ electrolyte layer between the porous electrodes for SOFCs [36].

1.1.6.3 Coatings Prepared by PS–PVD

As an enhanced PS–TF, the PS–PVD process is operated at pressures of 50–200 Pa and equipped with the O3CP plasma torch with higher electrical input power up to 180 kW. The combination of high energy and very low pressure allows PS–PVD to either melt the powder feedstock material for deposition as liquid splats or to vaporize the feedstock material for deposition as a condensate. The ability to vaporize feedstock material enables PS–PVD to produce columnar-structured YSZ coatings for turbine applications such as TBCs, which is very similar to those produced using the electron beam-physical vapor deposition (EB–PVD) (see Figure 1.12). However, unlike EB–PVD that has the drawbacks of high investment costs and low deposition rates, the PS–PVD process allows the production of thick columnar-structured YSZ coatings (100–300 μm) at a significantly higher deposition rate. Moreover, the simple gun and part motions in the PS–PVD process ensure a homogeneous temperature distribution over the target surface. This, combined with an expanding plasma jet and low working pressure, makes it possible to deposit the columnar YSZ coatings on the parts with complex geometries, even for the shadowed areas and areas that are not within the line of sight (see Figure 1.13).

The PS–PVD YSZ coatings exhibit excellent endurance in furnace cycle testing, in some cases exceeding that of EB–PVD coatings by a factor 1.3–2.7 [17,38]. Thermal conductivity testing also indicates that the PS–PVD YSZ coatings have a very low, stable thermal conductivity of 0.8–1.5 W/(m·K). However, the erosion

resistance of PS–PVD coatings is significantly lower than those produced using EB–PVD, but it is comparable with, and even 4–5 times higher than the erosion resistance of APS TBCs with a ceramic top coat porosity of 15 % [39]. Overall, these test results are quite favorable, indicating that PS–PVD YSZ coatings can provide excellent in-service results for TBCs, in addition to potentially reduced coating application costs.

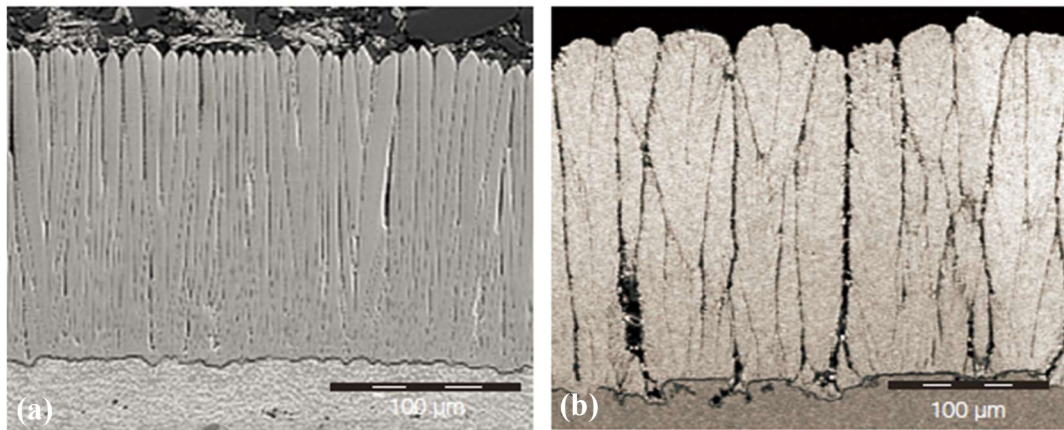


Figure 1.14 The microstructures of columnar YSZ coatings: (a) EB–PVD, (b) PS–PVD [31].

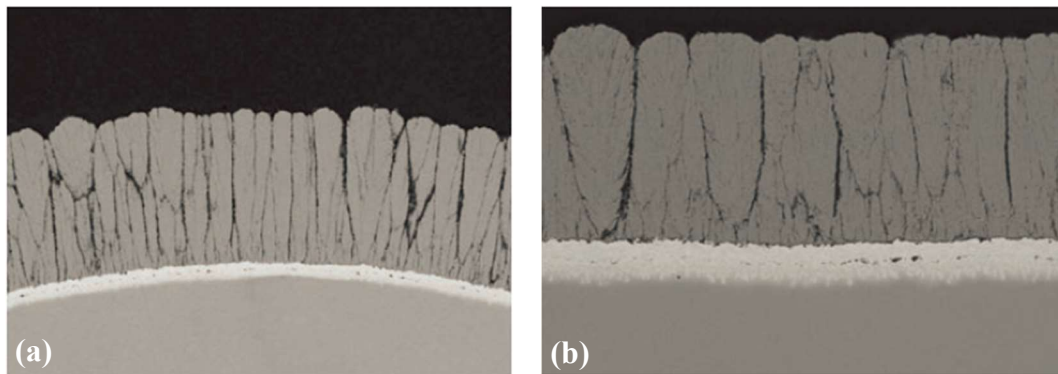


Figure 1.15 The microstructure of columnar TBC top coating (a) on the leading edge of the turbine blade, (b) on the pressure face of the turbine blade [31].

1.1.6.4 Coatings Prepared by PS–CVD

Unlike the higher-energy PS–PVD, the PS–CVD process uses a plasma gun operating at low power (< 10 kW), low gas flows and low pressures (< 100 Pa). It uses the liquid or gaseous precursors as reactive components to chemically react with other feedstock elements or compounds to create the deposition. The precursor materials can be injected either inside the plasma torch or downstream into the plasma jet using a gas injection ring (see Figure 1.14a) [40]. While low-power, PS–CVD

takes advantage of the high enthalpy and high ionization rate of the plasma jet for the full reaction and the vapor deposition. It allows the production of dense, full-coverage films with thicknesses of 0.3 to 10 μm . Compared with the conventional CVD processes, the deposition rates of PS-CVD are much higher, which makes it a cost-effective technology of coating application when thin, sub-micron dense coatings are required [41].

One of the most promising applications for PS-CVD is to produce silicon oxide (SiO_x) films. Thin, non-porous SiO_x films can be applied in microelectronics and optoelectronics due to their chemical resistance, optical transparency, electrical insulation characteristics and compatibility with crystalline silicon substrates. PS-CVD can prepare such films on silicon wafers or steel components by using hexamethyldisiloxane (HMDSO or $\text{C}_6\text{H}_{18}\text{OSi}_2$) in an oxygen-enriched plasma jet (see Figure 1.14b). The deposition rate and efficiency can reach 35 nm/s and 50 %, respectively. Other possibilities for films applied using PS-CVD include the application of thin films of pure metals such as silver, aluminum or copper. Thin films of metallic oxides can also be applied. For example, Al_2O_3 can be applied for electrical insulation or ZnO applied as a transparent conductive oxide (TCO) film.

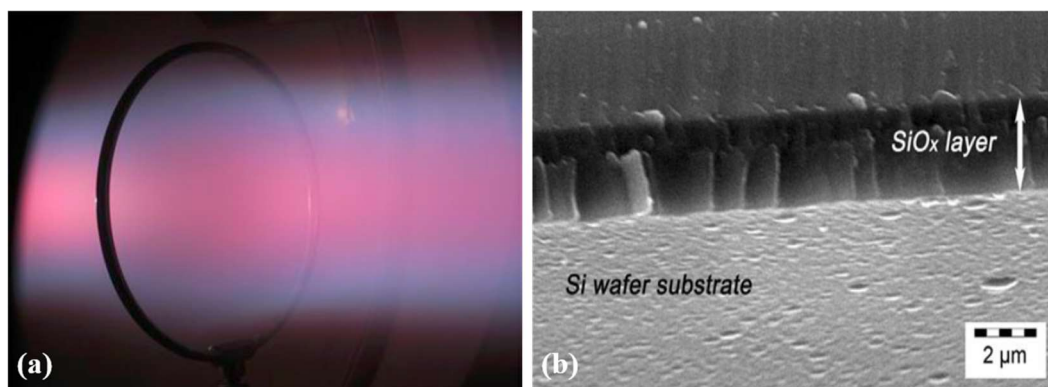


Figure 1.16 (a) The PS-CVD process exhibits a broad, diffuse plasma jet with high enthalpy and high ionization rates. Note the injection ring for gaseous precursors. (b) A film of SiO_x , approximately 2.5 μm thick, applied to a silicon substrate using PS-CVD in less than 3 min coating time [15].

1.2 Low-Pressure Suspension Plasma Spray

1.2.1 Introduction to Suspension Plasma Spray

1.2.1.1 Principle of Suspension Plasma Spray

For the past 30 years, numerous study and research have focused on nanostructured coatings due to their improved mechanical and physical properties, such as lowering thermal conductivity, increasing strength and toughness, and reducing apparent density. These advantages make the nanostructured coatings widely used in different fields of application, like thermal barrier coatings (TBCs), electrolytes in solid oxide fuel cells (SOFCs), wear-resistant coatings, and biomedical coatings [42]. Various deposition methods can be used to fabricate nanostructured coatings with high quality, such as the gas-condensation process, sol-gel process, chemical vapor condensation, electron beam vaporization, and magnetron sputtering [43]. However, these processes usually have the disadvantages of being costly and providing a slow deposition speed [44]. To solve the problem, thermal spray processes like APS and HVOF have been used to prepare nano-sized coatings, which have a rapid deposition rate at relatively low cost. However, conventional thermal spray processes use a gas carrier system to inject the feedstock particles into the plasma jet, whose average size ranges from 10 to 100 μm . When the particle size decreases from microscale to submicro- or nano-scale, the mass of the particle significantly reduces. To achieve the same injection force, a much higher gas carrier flow rate is needed, which will drastically perturb the high-enthalpy plasma jet [45,46]. In addition, the electrostatic surface forces between micron-sized and smaller particles can dominate the gravitational body forces acting on the particles, resulting in particle agglomeration and an inability to transfer powders through the feeder [47].

One way to overcome this drawback is to use agglomerated particles including nano-sized crystal grains. Such agglomerated particles with sizes in the range of 10 to 100 μm are large enough to be fed using a conventional injection route based on

carrier gas [48]. However, in regular thermal spraying, the deposition strategy is to melt the powder particles entirely or almost entirely to obtain an effective coating deposition. This cannot be applied to spray nanostructured agglomerates, because the nano-sized grains in the agglomerated particles are easy to turn into micro-sized ones during coating deposition. Therefore, the spray parameters must be optimized to produce conditions (particle temperatures and velocities) that result in only partial melting of the agglomerates. Thus the resulting coating can maintain the nanocrystals inside, but generate the microcrystals outside, ensuring its cohesion on the substrate (see Figure 1.15). As a result, the coating is usually deposited from the stacking of the lamellae, which has a bimodal microstructure rather than a full nanometer-sized one [49].

Another way to overcome this limitation is to directly spray the suspension containing the nanometer-sized particles, known as suspension plasma spray (SPS). Compared to a gas carrier, the more massive liquid carrier can generate the momentum required to inject these small powders into the high-enthalpy and high-velocity plasma stream without severe disturbance. Furthermore, a liquid carrier can contain dispersants that inhibit powder agglomeration. The schematic of SPS is shown in Figure 1.16, and the specific steps are as follows:

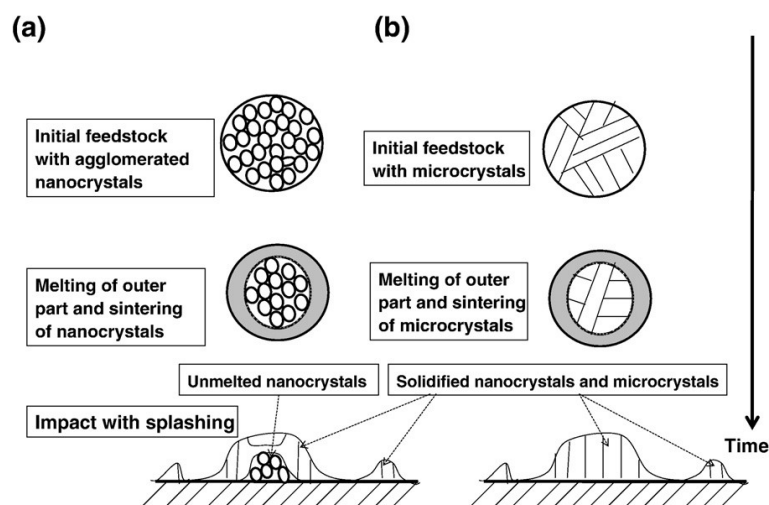


Figure 1.17 Evolution of crystals size at thermal spraying of different feedstocks: (a) agglomerated nano-particles, and (b) conventional micro-particles [49].

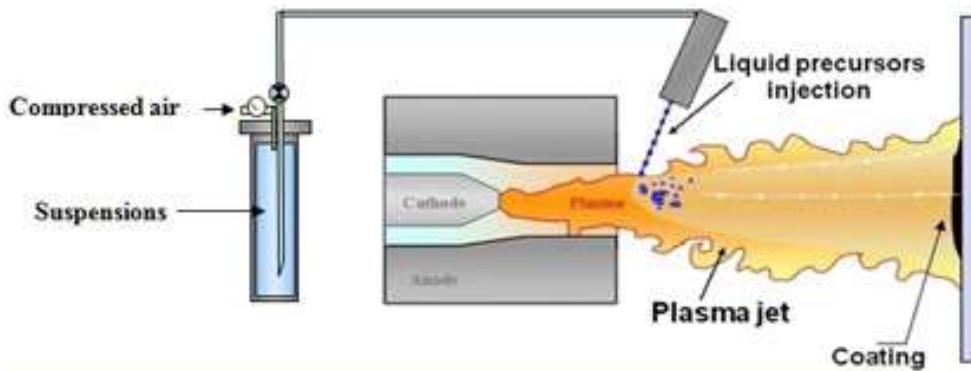


Figure 1.18 Schematic diagram of the SPS [50].

1. Suspension preparation. The suspension consists of fine particles dispersed in a solvent. The particles sizes vary from a few tens of nanometers to a few micrometers. The most frequently used solvents are ethanol, water or a mixture of both [46,51]. Due to electrostatic attraction, the fine particles have a natural tendency to settle and stick together, forming larger clusters or agglomerates. Thus, a suitable dispersant needs to be added in the suspension to resist the agglomeration and maintain the suspension stability. Furthermore, the percentage of dispersant must be adjusted to achieve a suspension with low viscosity and shear-thinning behavior [52].

2. Suspension injection. Atomization or mechanical injection can be used to radially or axially (depending on the design of plasma torch) transport the liquid into the plasma jet, via peristaltic pumps, plunger pumps and the pneumatic system [53-55]. After that, the suspension is injected as liquid jets or drops.

3. Coating deposition. The liquid jets or drops undergo fragmentation (due to flow shear forces) and then vaporization. Once the liquid phase is entirely vaporized, the solid particles contained will be released, heated and accelerated to deposit on the substrate.

1.2.1.2 Characteristics of Suspension Plasma Spray

Compared with the conventional plasma spray, SPS is much more complicated and has many new features, due to its different feedstock and carrier system. The detailed characteristics of SPS are shown in the following:

1. Suspension fragmentation and vaporization. Two main forces are exerted on the liquid jets or drops within the plasma jet: drag force and surface tension force. As the former is two orders of magnitude higher than the latter, the liquid jets or drops will be fragmented very fast. The fragmentation effect mainly depends on the Weber number $We = \rho v^2 d / \sigma$. For example, if $We > 350$ (catastrophic breakup), the liquid can be fragmented into droplets smaller than a few μm in a less than 10 mm trajectory in the plasma jet. However, it is worth underlining that the plasma properties continuously and drastically vary from the plasma fringe to the plasma core, leading to a continuous variation of the Weber number. After fragmentation, the droplets will be progressively vaporized. The vaporization time is about 2 to 3 orders of magnitude longer than the fragmentation time [52].

The particle morphology and size distribution also influence the fragmentation and vaporization processes. For example, the YSZ particles made by attrition milling, after the solvent vaporization, are accelerated, heated, and melted by the plasma as shown schematically in Figure 1.17. While using other YSZ particles obtained by a chemical process, the behavior upon solvent vaporization is different. The big droplets containing agglomerates or aggregates explode after the solvent vaporization. Then the solid powders inside are released and result in molten particles and smaller particle vaporization as shown in Figure 1.18 [56].

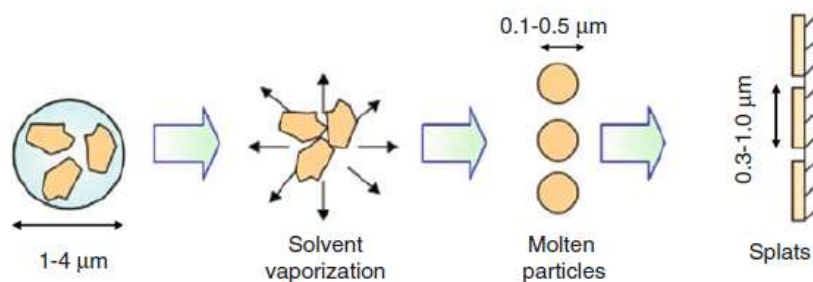


Figure 1.19 Schematic of suspension droplet treatment when containing attrition-milled particles [56].

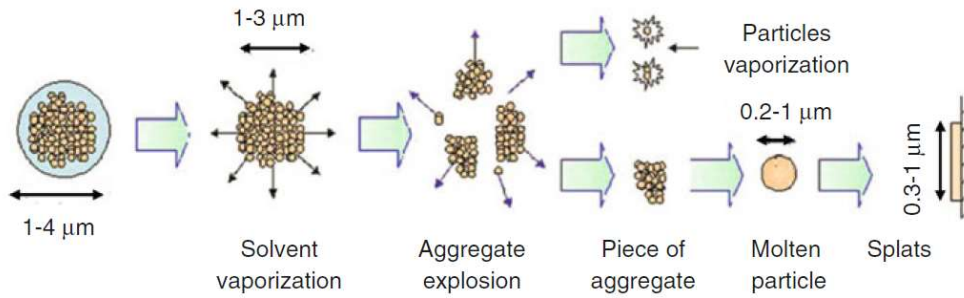


Figure 1.20 Schematic of suspension droplet treatment when containing aggregates and agglomerates [56].

2. Particle trajectory. For radial injection, the fragmentation and vaporization occur from the plasma fringe to the plasma core. Thus the solid particles will follow different trajectories and widely dispersed in the plasma jet, as shown in Figure 1.19 [57]. When the solid particles are in the plasma fringes, they will be insufficiently treated, forming stacking defects. When the solid particles are in the plasma core, some of them will agglomerate then deposit as small splats after full melting, while some of them will go to the cold areas due to the thermophoresis effect, resulting in spherical particles. For axial injection, the liquid phase can be directly injected into the plasma core. The solid particles contained can be rapidly released with a relatively narrow trajectory, which favors the particles to be sufficiently heated and accelerated. However, the turbulence and thermophoresis effect still make some particles disperse in the plasma fringes.

Furthermore, it is noteworthy that it is possible for the nanoparticles with low inertia to follow the plasma flow and these do not impact on the substrate. To avoid this, the impacting velocity of the molten particle must be high enough to achieve Stoke number (St) >1 , as shown in Figure 1.20 [58]. Therefore, to achieve an effective deposition of the coating, the spray distance for SPS is much shorter than that for conventional plasma spray.

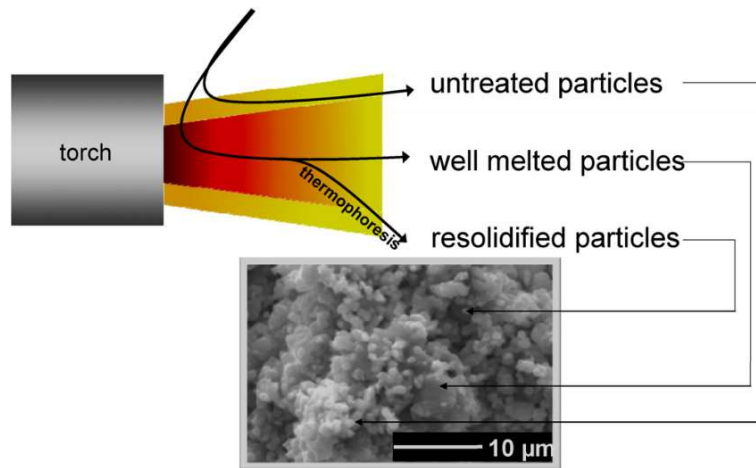


Figure 1.21 Schematic of particle trajectories within the plasma jet core and its fringes with the corresponding coating [57].

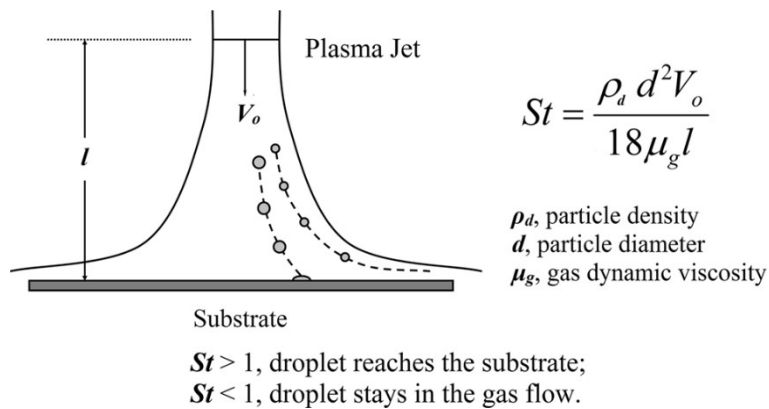


Figure 1.22 Stokes number for in-flight particles and the effect on deposition [58].

3. Heat and momentum transfers. The fine-particle size used by SPS is comparable to the mean free path of a plasma jet. Due to the Knudsen effect, the heat and momentum transfers in SPS are weaker than those in conventional plasma spray [59]. Moreover, the vaporization of the liquid phase in SPS cools down drastically the hot gas flow (20–30 % of the energy available), which further reduces the heating and acceleration ability of SPS [60].

1.2.1.2 Coatings Prepared by Suspension Plasma Spray

Due to fine nano- or submicron-scale particles used in SPS, a tailored coating architecture with different microstructures can be achieved, such as highly dense, highly porous and columnar-like or vertically cracked. The coating structure is strongly dependent on the spray parameters, such as particle size, suspension feed

rate, suspension concentration, spraying distance, and substrate roughness. [53,56,61-63]. The diversity of microstructures has attracted significant attention in academic research. The major fields of research are the generation of improved thermal barrier coatings (TBC) for gas turbines and engines, coatings for wear protection, components for fuel cells (SOFC), biocompatible coatings for implants, and photocatalytic coatings [64-68]. In the following, the YSZ-based TBCs will be chosen as a typical example to exhibit the different microstructures that can be obtained by SPS.

Coating with Laminar Structure

When spraying submicron molten YSZ particles onto a smooth substrate preheated above the transition temperature (~ 500 K for YSZ), the splats are identical to those obtained with micro-sized sprayed particles. However, because the small particles have lower impact velocities together with more considerable surface tension, a low flattening degree of about two at the maximum is achieved. Therefore, the diameters of SPS splats are generally between 0.2 and 3 μm , with thicknesses between 60 and 300 nm. The smaller and thinner splats reduce drastically the coating porosity as well as the micro-cracking within splats due to quenching stress, which favors the densification of coatings.

Fauchais et al. [69] achieved a fully dense YSZ coating with a thickness of about 30 μm by using attrition-milled YSZ particles ($d_{50}=1$ μm). The coating fracture is illustrated in Figure 1.21. Two different modes of coating growth can be observed, columnar growth for the top interface and granular growth for the base coating. The difference in heat transfer during the spraying process causes this distinct morphology. During the first few passes, the heat stress imposed by the convective flow of the plasma jet and the heat content of the deposited YSZ material is rapidly withdrawn by the substrate, resulting in a coating of columnar nucleation and growth. After a few layers, the thermal insulation from the coating, together with the drastic heat flux from the plasma, delays the splat solidification, allowing the surface tension

force to take over and resulting in quasi-spherical particles in a molten state sticking together before their solidification. Thus a granular structure without interconnected porosities is obtained.

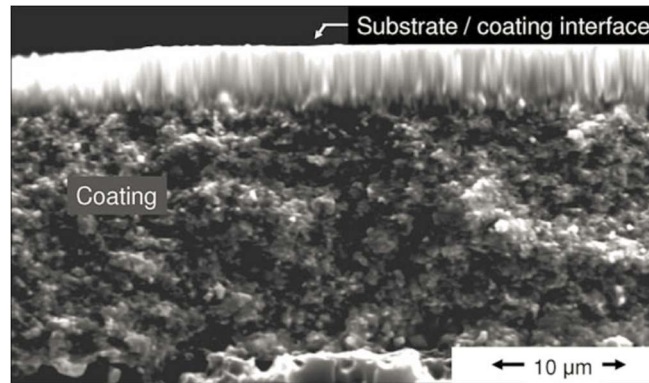


Figure 1.23 Fracture of a YSZ coating obtained by SPS [69].

Coating with Columnar Structure

Sokołowski et al. [70] systematically investigated the critical process parameters influencing the formation of columnar microstructure in SPS YSZ coatings, including the particle types, solid concentrations, substrate preparation methods and plasma spray setups. As shown in Figure 1.22 and Figure 1.23, the microstructure of the coatings depends on the solid concentration as well as the substrate surface morphology. The high solid concentration with smooth substrate surface favors the formation of a relatively dense coating, while the low solid concentration with rough substrate surface promotes the formation of columnar structures. The formation mechanism can be explained by the interaction of atomized droplets with the plasma jet [71-73]. As described in Section 1.2.1.2, the small particles with $St < 1$ will follow the gas flow parallel to the substrate surface, which will not only eliminate these particles from the coating generation but also create defects. This type of defect along with the substrate asperities can induce coatings with columnar microstructure. Van Every et al. [73] initially explained this phenomenon by the shadow effects theory. Ganvir et al. [74] further elucidated the dependence of droplet morphology on its size after it impacts onto a rough surface. As described in Figure 1.24, the massive large droplet has a high normal component of velocity and is hardly affected by the plasma

gas, which favors the normal deposition on the substrate without shadowing. In contrast, as the droplet size decreases, the small light droplet has a high parallel component of velocity and is easily influenced by the plasma gas, which preferentially impacts on the surface asperities and benefits the formation of columnar structures.

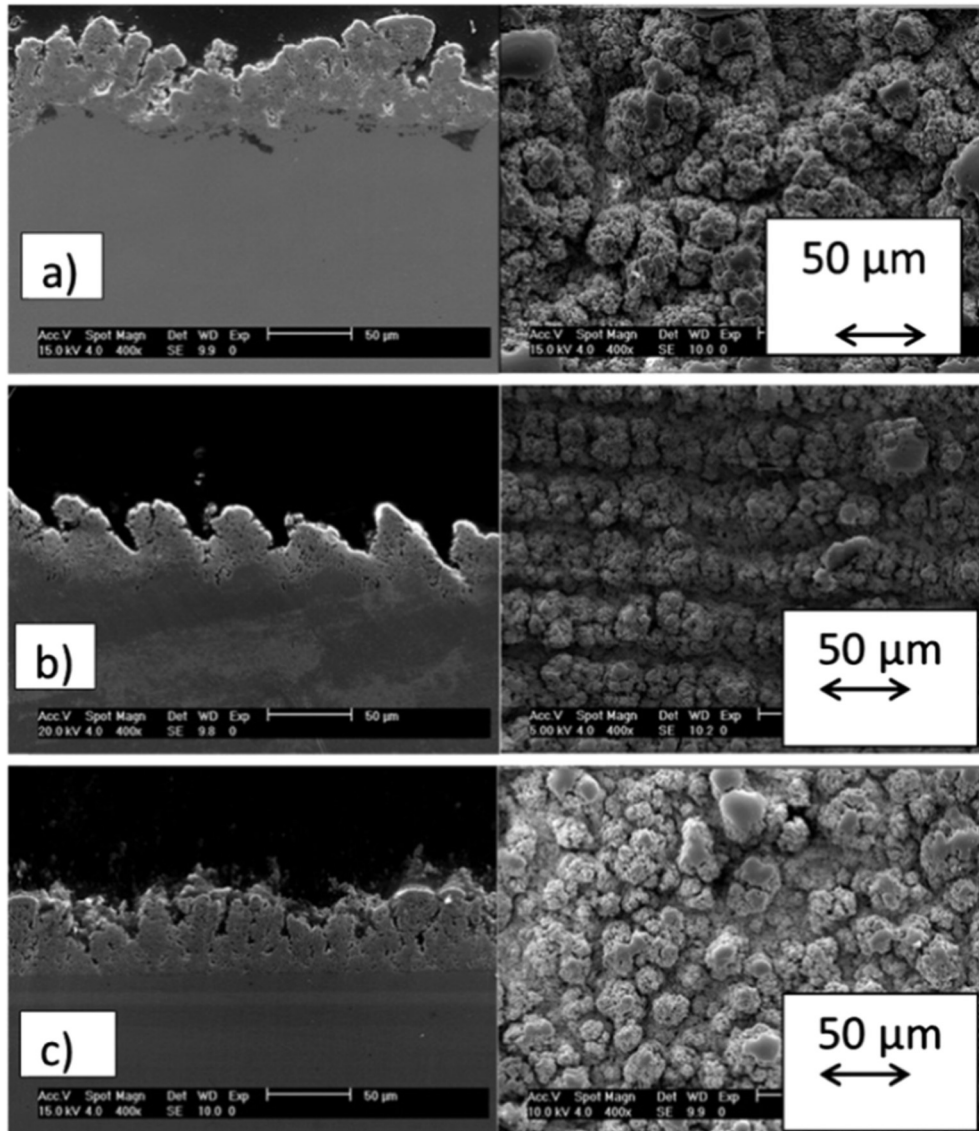


Figure 1.24 Cross sections (left side) and surfaces (right side) microstructures of YSZ coatings with 2.5 wt.% solid phase deposited on different substrates prepared by (a) sandblasting, sample; (b) laser treatment, sample; (c) grinding [70].

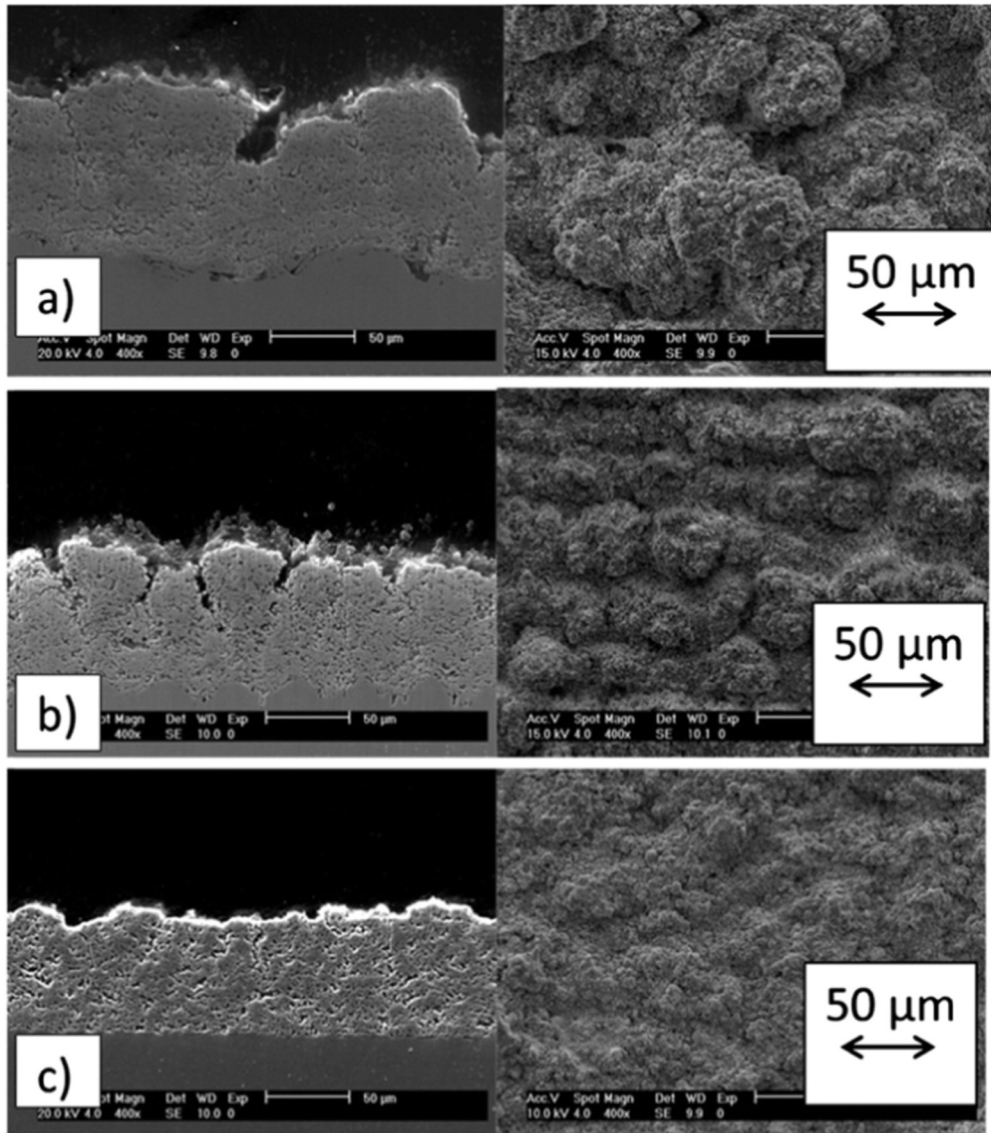


Figure 1.25 Cross sections (left side) and surfaces (right side) microstructures of YSZ coatings with 10 wt.% solid phase deposited on different substrates prepared by (a) sandblasting, sample; (b) laser treatment, sample; (c) grinding [70].

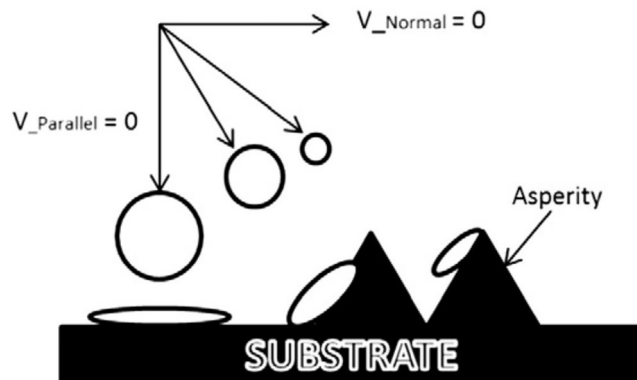


Figure 1.26 Dependence of droplet impact on substrate asperity on droplet momentum [74].

1.2.2 Why Use Low-Pressure Suspension Plasma Spray

As mentioned above, the velocity of small particles before striking the substrate is an essential factor to obtain coatings with different microstructures. Even for obtaining the columnar structure, high particle velocities are required for the deposition on the substrate asperity. However, traditional plasma spray can only produce a short plasma jet, typically less than 5 cm in length. To achieve sufficient impacting velocities of small particles, a short spraying distance must be used according to the Knudsen effect. Generally, the spraying distance of SPS is 30–40 mm, against 100–120 mm for conventional plasma spray. Such a short spraying distance will bring some disadvantages. For example, the plasma heat flux to the substrate could reach 20–40 MW/m², which increases the difficulty of substrate cooling and spraying parts with complex shapes. Moreover, due to jet cooling by the solvent vaporization, such a short spraying distance makes it difficult to entirely melt the powder particles [75,76].

To overcome the disadvantages of conventional SPS, studies have been done by using a Triplex torch (Oerlikon Metco, Switzerland) [77,78] and Axial III torch (Northwest Mettech Corp, Canada) [65,79]. The two torches can produce more extended plasma jets to achieve higher impact velocities of small particles, which can improve the coating quality and process efficiency. Especially for the Axial III torch, its high plasma power (~150 kW) and central injection can generate coatings that are vertically cracked, porous, and exhibit a feathery columnar microstructure like EB–PVD coatings.

Since the increase in particle velocity and plasma power can improve the SPS process and obtain higher quality coatings, this study attempts to offer another enhanced method by combining the LPPS and SPS processes (LP-SPS). Firstly, the low pressure lengthens the plasma jet of conventional SPS, which can increase not only the impact velocities of particles contained in suspensions but also the heating time of particles. Moreover, it is possible to use the high power plasma torch under

low pressure, which can further compensate the jet cooling caused by the solvent vaporization. Finally, LP-SPS can produce homogenous coatings that are deposited from splats or even from the vapor phase. The parts with complex geometries can be sprayed, even for areas that are not in the line of sight.

1.2.3 Challenge for the Plasma Torch Used In Low-Pressure Suspension Plasma Spray

For the F4VB torch and O3CP torch used in LPPS, both of them apply the single cathode/single anode system with the radial injection under low pressure, which makes it feasible to inject micro-sized powders, but very hard to deliver the suspension. The expanding plasma jet with high velocity under low pressure will keep the droplets traveling in the jet fringes after radial injection, leading to the particles contained being poorly heated, accelerated and creating defects in the coating. Moreover, the radial injection makes it easy to burn the suspension injector and clog up the torch nozzle within a few minutes [45]. Therefore, the axial injection mode is necessary to realize the SPS under low pressure.

At present, the Axial III torch is the most widely used plasma torch for axial SPS. It consists of three cathodes and three anodes operated by three independent power supplies (see Figure 1.25). The three plasma jets converge within an interchangeable nozzle, and liquid feedstock is injected axially between the three plasma jets [80,81]. Unfortunately, this plasma torch has never been used under low pressure. It is possible to have an unexpected arcing when operating under vacuum, which will damage the LPPS equipment. Therefore, it is necessary to design a specially made plasma torch with axial injection for realizing the LP-SPS.

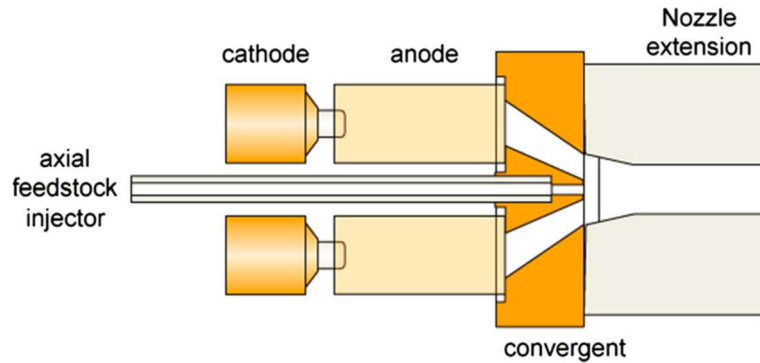


Figure 1.27 Schematic of the Northwest Mettech Axial III torch with central injection [76].

1.2.4 Coating Prepared by Low-Pressure Suspension Plasma Spray

Very few papers have reported the investigation of LP-SPS because of the difficulty of implementation. The preliminary research for LP-SPS was conducted at the LERMPS laboratory (UTBM, Belfort, France). He et al. [45] deposited the nanostructured YSZ coating using the SPS at 100 Pa. To inject the YSZ suspension axially under low pressure, a tri-cathode/one-anode plasma torch with the axial injection mode was designed, as shown in Figure 1.26. By using this plasma torch, the YSZ powders contained in suspension were partially vaporized based on optical emission spectroscopy. The resulting coatings are relatively dense due to the high velocity of particles accelerated by the plasma jet at very low pressure (see Figure 1.27). The surface microstructure showed that the YSZ coatings are composed of melted and agglomerated particles after solvent vaporization and the condensation of the vapor phase (see Figure 1.28). The hardness and elastic modulus of the as-sprayed coating is increased by 61 % and 31 %, respectively, in comparison with the value obtained at atmospheric ambient. This dense nanostructured coating could be used as the electrolyte of SOFC.

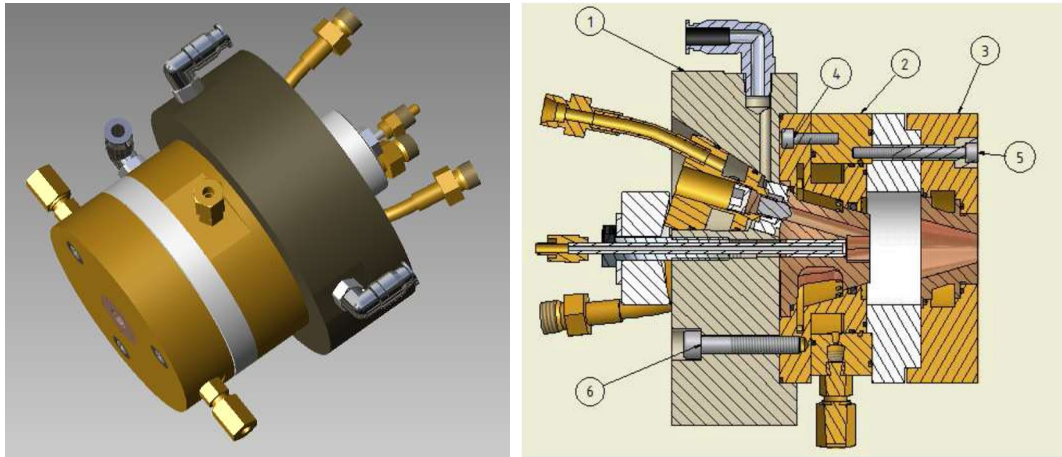


Figure 1.28 The configuration of the tri-cathode torch with the axial injection mode [82].

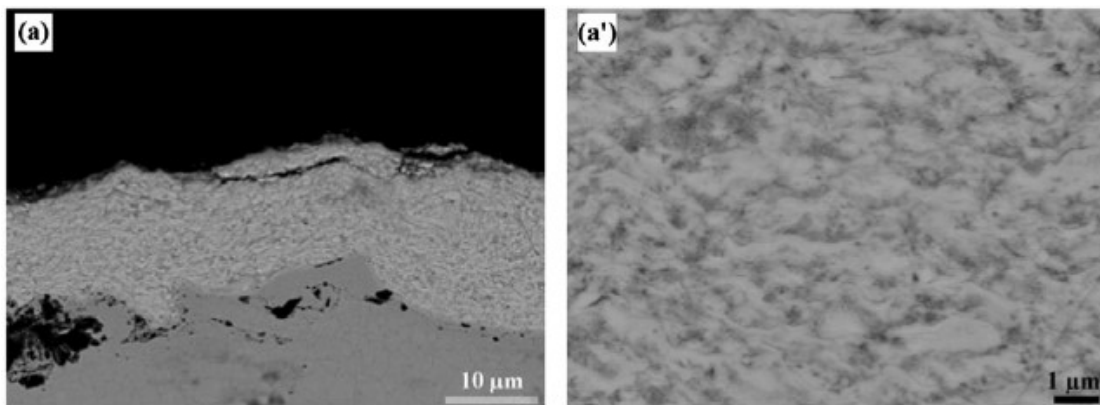


Figure 1.29 The cross-sectional morphologies of YSZ coatings deposited by LP-SPS at 150 mm: (a) low magnification, (a') high magnification [45].

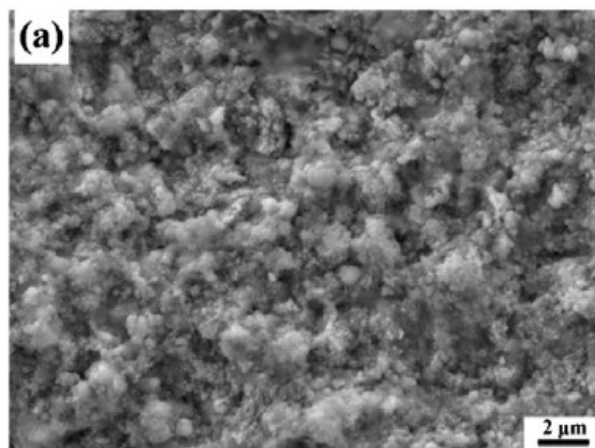


Figure 1.30 Surface morphology of YSZ coatings deposited by LP-SPS at 150 mm [45].

In addition, another researcher, Fleetwood [83], also produced thin and pore-free SOFC electrolytes via a combination of the VLPPS and SPS. A Sulzer Metco 03CA plasma torch with an N_2 pressurized suspension feed system was used. The

dimensions of the cathode and anode setup are shown in Figure 1.29. The suspensions were injected radially into the torch throat with a back pressure of ~ 3900 Torr (0.52 MPa). A second feed supply of ethanol was also used to keep the injection nozzle cooling before suspension injection, as well as to clean the feed system after deposition. The resulting YSZ coating is dense but still has unmelted particles, which means that the radial suspension injection is not so good for uniformly heating the powder.

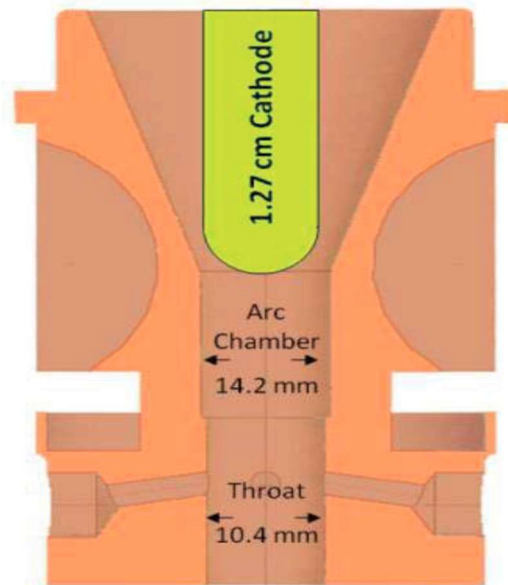


Figure 1.31 A diagram of the cathode and anode plasma gun setup [83].

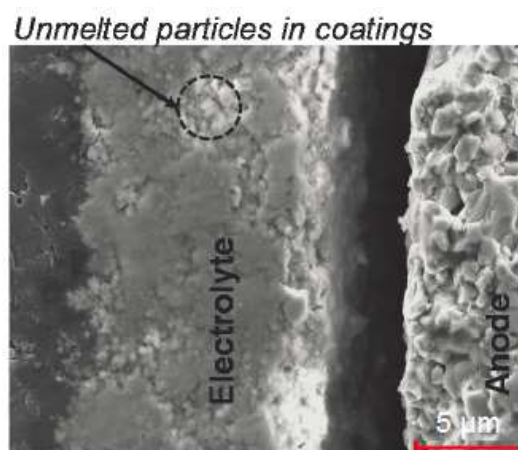


Figure 1.32 The presence of unmelted YSZ particles in the cross section image [83].

1.3 Low-Pressure Reactive Plasma Spray

1.3.1 Introduction to Reactive Plasma Spray

1.3.1.1 Principle of Reactive Plasma Spray

Reactive plasma spray (RPS) is a process developed in the 1990s, which combines traditional plasma spray with self-propagating high-temperature synthesis (SHS) to produce in-situ composite coatings (especially ceramic coatings) [84-86]. According to the different reactants, the RPS process can be divided into two types. The first one is the RPS without reaction gas. The spraying powder is injected into the plasma jet as the only reactant for the self-propagating combustion reaction, as shown in Figure 1.31. The second one is RPS with reaction gas (e.g., N_2 or CH_4), which is introduced into the plasma jet as a carrier/working gas or by an additional injection, and then reacts with the spraying powder to form the desired product, as shown in Figure 1.32.

During RPS, the plasma jet favors the conditions for the reactions so that the desired materials like carbides or nitrides can be formed despite the very short reaction time available. Due to the short reaction time, the deposited material is usually a composite of the starting material forming the matrix and phases synthesized *in situ* [87]. Moreover, the chemical reactions for RPS are considered to take place either in-flight within the plasma gas, or after the deposition on the formed deposit. In most cases, it is believed that both mechanisms contribute to the process [5].

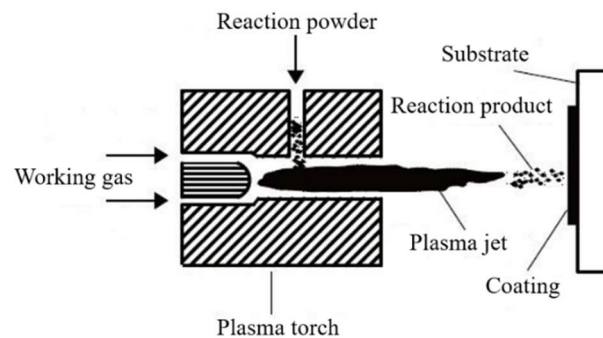


Figure 1.33 Schematic diagram of RPS without reaction gas.

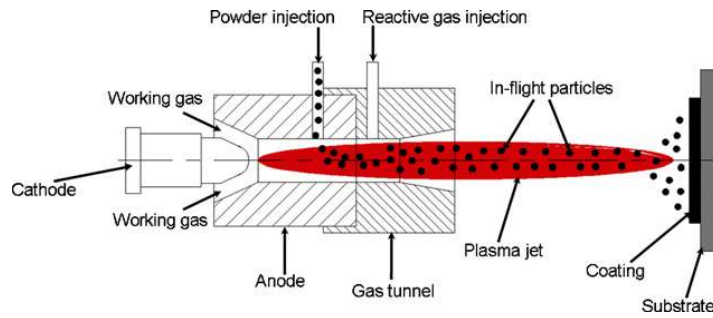


Figure 1.34 Schematic diagram of RPS with reaction gas [88].

1.3.1.2 Characteristics of Reactive Plasma Spray

As an integrated process, RPS has the advantages of both PS and SHS processes. The detailed characteristics of RPS are shown in the following:

1. Similar to APS, RPS is a low-cost and straightforward process, which is due to the possibility of substituting expensive raw materials with cheaper ones for synthesizing the same products and the relatively low energy requirement due to the significant amounts of heat released by exothermic reactions. Moreover, because the chemical reaction and coating formation occur almost simultaneously, RPS usually has a high deposition rate, which can prepare thick (up to several hundreds of microns or more) and scaleable coatings.

2. Compared with APS, RPS forms the second phases *in situ* directly from the powder matrices, which should have stronger cohesion with the matrix and should be uniformly distributed in the resulting coating [89].

3. The RPS products can be significantly affected by adjusting the spraying parameters, such as increasing the plasma power and external atmosphere. Furthermore, it is even possible to form metastable or intermediate phases by combining steep thermal gradients, high reaction rates, and relatively rapid cooling rates [84].

1.3.1.3 Coatings Prepared by Reactive Plasma Spray

Several composite coatings with improved properties have been successfully produced by using different RPS processes [90-97], especially for the *in-situ* fabrication of nitride coatings. This is because the nitride coatings are easily

decomposed under high temperature when conventional techniques directly prepare them.

Feng et al. [98] synthesized a TiN coating *in situ* by injecting the pure Ti powders by the N₂ carrier gas into the Ar and N₂ containing plasma jet. The XRD result (see Figure 1.33a) showed that the coating is mainly composed of TiN and small quantities of Ti₃O. The Ti₃O phase may come from surface oxidation of the superfluous Ti or TiN phase under high temperature in the atmosphere. The cross-sectional morphology of the TiN coating (see Figure 1.33b) indicates that its thickness exceeds 500 μm, which is about 100 times thicker than that of TiN films prepared by CVD or PVD. The dense structure with few pores should be attributed to the powders with high kinetic energy supplied by the plasma jet. The average hardness of the RPS TiN coating is about 1200 Hv_{100g}. Besides, its toughness is superior to multilayered CVD TiN/Ti(C, N)/TiC films.

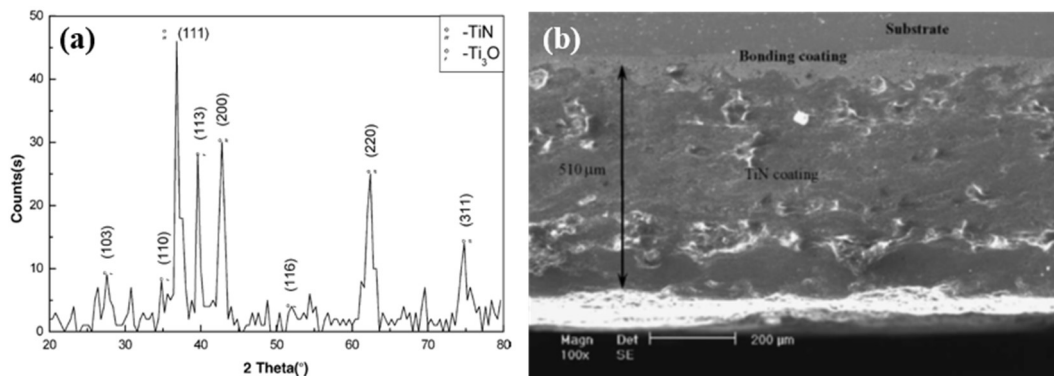


Figure 1.35 (a) The cross-sectional morphology of the RPS TiN coating, (b) XRD pattern of the RPS TiN coating [98].

Furthermore, Valente et al. [92] prepared the Ti/TiN coatings by spraying Ti powders in a controlled atmosphere plasma spray system. Ar-H₂ (-He) and Ar-N₂ were used as plasma gases when nitrogen was selected as the chamber and carrier gas. The chamber pressure was varied between 20 and 300 kPa to study its effects on TiN phase formation. The XRD result (see Figure 1.34a) showed that the Ti₂N was the dominant phase at pressures higher than 90 kPa, and the higher chamber pressures enhanced the nitride formation. Besides, according to the measurement of the

nitrogen content in the collected particles, the effect of N_2 pressure on nitridation was more significant than with N_2 as plasma gas (see Figure 1.34b).

Shahien et al. [99] fabricated an AlN coating through reactive plasma nitriding of Al feedstock powder in an N_2/H_2 plasma jet. The obtained coatings were a cubic-AlN/Al mixture with 100 μm thickness at 150 mm of spray distance. Since the nitride content increases gradually with spray distance, the coating mostly consists of AlN at 300 mm. The nitriding reaction was investigated, and it indicated that Al particles might react during flight and after deposition on the substrate surface.

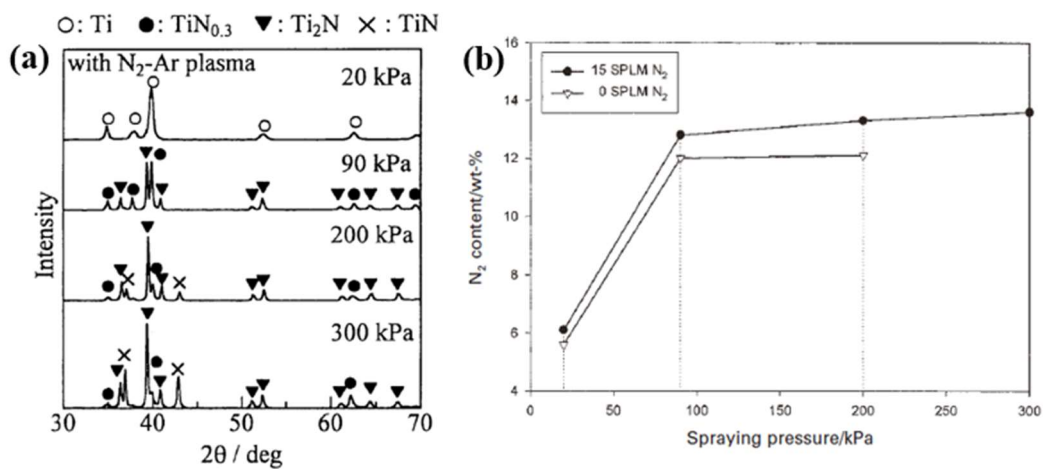


Figure 1.36 (a) XRD patterns for coatings sprayed with given chamber pressures, (b) variation of nitrogen content in collected particles with spraying pressure [92].

1.3.2 Why Use Low-Pressure Reactive Plasma Spray

Conventional RPS usually operates in atmospheric conditions. Thus the deposits can easily have uncontrolled levels of oxides and nitrides due to the interaction of the molten particles with the entrained air, especially for spraying the metal material. Furthermore, the plasma power for RPS is usually not enough to make the full reaction.

Low-pressure reactive plasma spraying (LP-RPS), which combines LPPS and RPS, can solve the problems. Firstly, using an LPPS facility can offer a controlled and low-pressure atmosphere for the reaction, which can improve the deposit quality by lowering the potential for uncontrolled deposit inclusions. Moreover, the LPPS

system can operate under high power and very low pressure, making it possible to obtain a long plasma jet with high enthalpy. Such a plasma jet can provide sufficient energy and time to vaporize Ti powder and ionize N₂, which is conducive to achieving a complete nitridation reaction. In addition, the plasma jet has a high velocity, allowing the resulting coating to be denser and more uniform, then has enhanced performance.

1.3.3 Coatings Prepared by Low-Pressure Reactive Plasma Spray

The studies reported by Zhao et al. [87], Vautherin et al. [100] and Zhu et al. [101] give typical examples of coatings prepared by LP-RPS.

Zhao et al. [87] formed titanium nitrides *in situ* by using a TiAl6V4 powder under 29–59 kPa. A mixture of Ar+N₂ was used as plasma gas, and N₂ was additionally introduced into the plasma jet through a reactor. As shown in Figure 1.35, the resulting coating had a very dense lamellar microstructure due to the high-velocity plasma jet under low pressure. Based on the XRD result, nitride phase was successfully synthesized, but its content was not very high. This could be attributed to the limited plasma power (–40 kW) and weak collision frequency under low pressure. The study also found that the chamber pressure and the nitrogen flow rate were the two main influencing factors for the nitrogen content of the coatings.

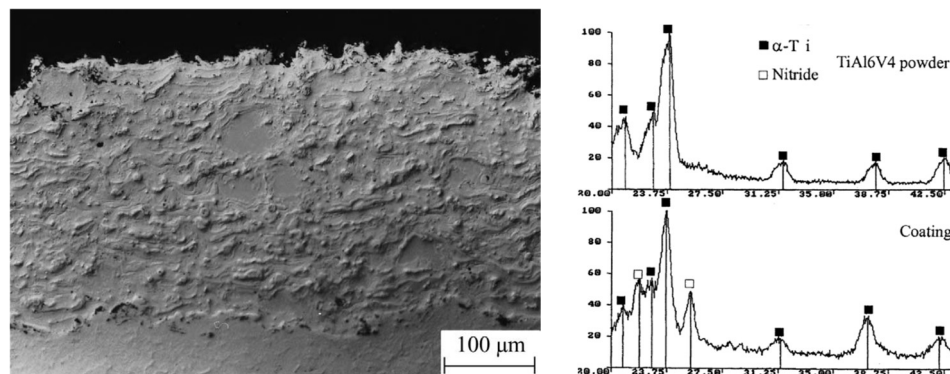


Figure 1.37 Cross section of the coating (left), XRD of the powders and the coating (right) [87].

Vautherin et al. [100] prepared dense Ti-TiN coatings by using pure Ti powder under 150 Pa (see Figure 1.36). Three different ways were considered to inject the

reactive N_2 into the plasma flow, including through working gas, carrier gas, and a ring-shaped injector near the substrate. The XRD result shown in Figure 1.37 indicates that the nitriding reaction was still incomplete because of insufficient plasma power (~ 54 kW). Three stoichiometric nitrides, TiN, $TiN_{0.3}$, and Ti_2N , were formed in the coatings. By applying higher plasma enthalpy, the nitridation could be enhanced. Besides, the ring-shaped N_2 injector near the substrate could also increase the nitrogen content in the coating, which demonstrated that nitriding mechanisms take place not only during the plasma jet but also on the substrate surface during the particle re-solidification.

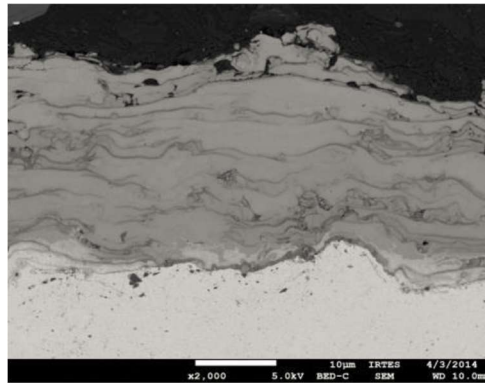


Figure 1.38 SEM observations of Ti-TiN coating cross sections elaborated by VLPPS [100].

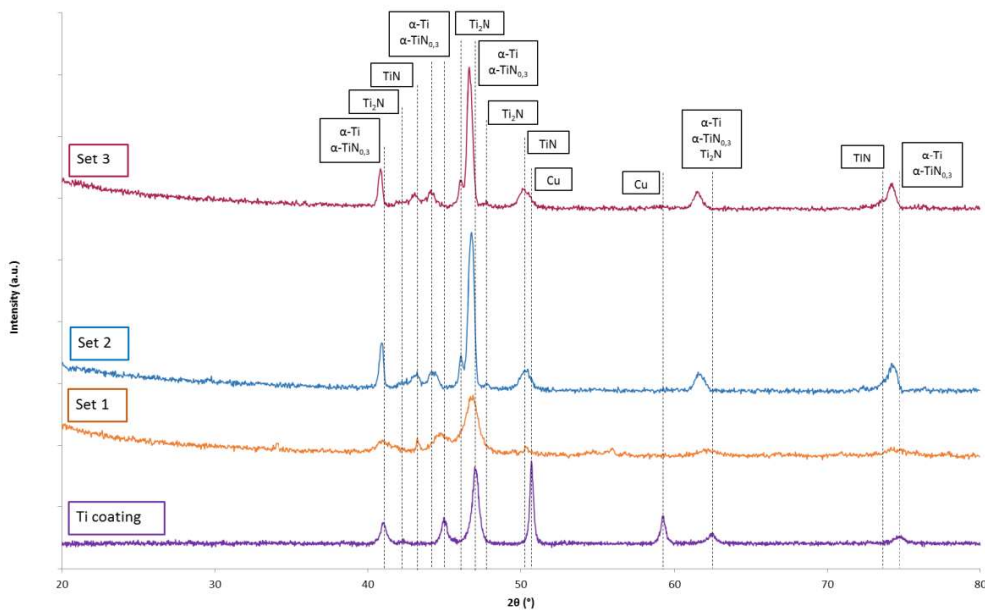


Figure 1.39 XRD pattern obtained on Ti coating and Ti-TiN coatings elaborated by VLPPS from different spraying parameters [100].

L Zhu et al. [101] reported that a dense and homogeneous FeAl coating was successfully in-situ synthesized by reactive plasma spraying of an Al/Fe₂O₃ composite powder under 1 mbar. According to the XRD patterns displayed in Figure 1.38, there are no Al or Fe₂O₃ phases but only FeAl phase existing in the coatings, suggesting a near complete reaction by using LP-RPS. The use of low pressure is certainly a key factor in allowing the formation of an oxide-free material. Besides, the FeAl coating exhibited a quite dense and uniform microstructure because of the expanding plasma jet under low pressure, as shown in Figure 1.39. As a result, the Vickers microhardness of the FeAl coatings is much higher than that of HVOF coatings or even of sintered samples [102,103].

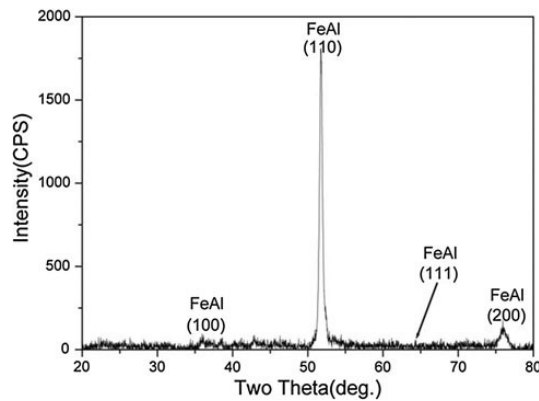


Figure 1.40 XRD pattern of the FeAl coating [101].

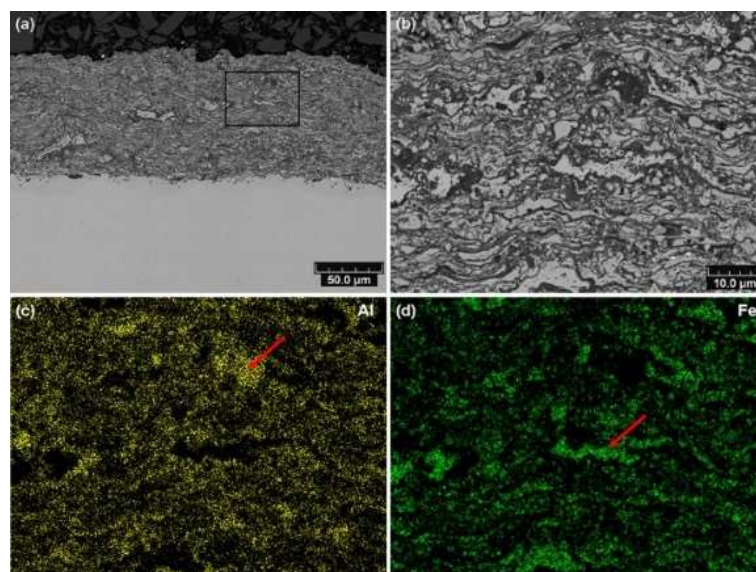


Figure 1.41 (a) Cross-sectional microstructure of the FeAl coating, (b) high-magnification image of the black frame in (a); (c) and (d) the corresponding Al and Fe elements mapping in (b) [101].

1.4 Objectives of the Thesis

As an advanced thermal spray technology, LPPS can bridge the thickness gap between conventional thermal spray processes and standard thin film processes. Moreover, the uniform coatings with different microstructures can be obtained by using the LPPS. The deposition takes place not only from liquid splats but also from nano-sized clusters and the vapor phase. To better utilize and further develop the LPPS process, this study combines the LPPS with the emerging SPS and RPS processes. We hope not only to provide a new integrated process but also to achieve unique coatings with fine microstructures and high performance.

Specifically, the work of the thesis is divided into several parts:

- Above all, a bi-cathode plasma torch with axial injection mode was designed and built for the LPPS, whose maximum input plasma power was able to reach 81 kW. The new torch allowed to inject either the very fine-particle suspension or the micro-sized powders into the plasma center under low pressures. Consequently, the heat and mass transfer between the plasma jet and the sprayed materials could be enhanced, making it possible to achieve high-quality coatings with high deposition efficiency.
- Furthermore, the axial bi-cathode plasma torch was used to deposit the YSZ coatings under low pressure. Two types of YSZ feedstock were employed, including the agglomerated YSZ powder and YSZ suspension. Different spraying parameters were applied, and their effect on the plasma jet as well as the morphology, phase structure, mechanical property of the YSZ coating was investigated.
- Finally, another O3CP plasma torch that with a higher power of 120 kW was adopted to in-situ synthesize the TiN coatings on Ti-6Al-4V alloy by using the reactive plasma spray under very low-pressure. The influences of the spraying distances on the vaporization degree, the nitriding effect and the microstructure

of TiN coatings were discussed. The mechanical properties of the TiN coatings and the Ti-6Al-4V substrate were also investigated.

References

- [1] P. Fauchais, Understanding plasma spraying, *Journal of Physics D: Applied Physics* 37(9) (2004) R86.
- [2] AEROMAC, Advantages of Various Thermal Spray Processes. <http://www.aeromac.com.sg/thermalsprayadv.html>.
- [3] A. Vardelle, C. Moreau, N.J. Themelis, C. Chazelas, A perspective on plasma spray technology, *Plasma Chemistry and Plasma Processing* 35(3) (2015) 491-509.
- [4] R.C. Tucker Jr, *ASM Handbook, Volume 5A: Thermal Spray Technology*. ASM International, 2013.
- [5] P.L. Fauchais, J.V. Heberlein, M.I. Boulos, *Thermal spray fundamentals: from powder to part*, Springer Science & Business Media 2014.
- [6] Oerlikon Metco, Atmospheric Plasma Spray Solutions V6, 2017. https://www.oerlikon.com/ecomaXL/files/metco/oerlikon_Plasma_Solutions_EN6.pdf&download=1.
- [7] J.R. Davis, *Handbook of thermal spray technology*, ASM international 2004.
- [8] E. Muehlberger, Method and apparatus for effecting high-energy dynamic coating of substrates, Google Patents, 1974.
- [9] V. Wilms, LPPS deposited coatings for the protection against hot gas corrosion - a first evaluation, in *Proceedings of the 9th International Thermal Spray Conference*, Nederlands Instituut voor Lastechniek, The Hague, The Netherlands (1980) 317-324.
- [10] M. Braguier, R. Tueta, Supersonic and vacuum arc plasma spraying apparatus characteristics and application to metallic coatings, in *Proceedings of the 9th International Thermal Spray Conference*, Nederlands Instituut voor Lastechniek, The Hague, Netherlands (1980) 67-72.
- [11] L. Pawlowski, *The science and engineering of thermal spray coatings*, John Wiley & Sons 2008.
- [12] E. Muehlberger, P. Meyer, LPPS—Thin Film Processes: Overview of Origin and Future Possibilities, *Thermal Spray 2009: Proceedings of International Thermal Spray Conference, 2009*, pp. 737-740.
- [13] E. Muehlberger, Method of forming uniform thin coatings on large substrates, Google Patents, 1998.

- [14] M.F. Smith, A.C. Hall, J.D. Fleetwood, P. Meyer, Very Low Pressure Plasma Spray—A Review of an Emerging Technology in the Thermal Spray Community, *Coatings* 1(2) (2011) 117-132.
- [15] A. Vardelle, C. Moreau, J. Akedo, H. Ashrafizadeh, C.C. Berndt, J.O. Berghaus, M. Boulos, J. Brogan, A.C. Bourtsalas, A. Dolatabadi, M. Dorfman, T.J. Eden, P. Fauchais, G. Fisher, F. Gaertner, M. Gindrat, R. Henne, M. Hyland, E. Irissou, E.H. Jordan, K.A. Khor, A. Killinger, Y.C. Lau, C.J. Li, L. Li, J. Longtin, N. Markocsan, P.J. Masset, J. Matejicek, G. Mauer, A. McDonald, J. Mostaghimi, S. Sampath, G. Schiller, K. Shinoda, M.F. Smith, A.A. Syed, N.J. Themelis, F.L. Toma, J.P. Trelles, R. Vassen, P. Vuoristo, The 2016 Thermal Spray Roadmap, *Journal of Thermal Spray Technology* 25(8) (2016) 1376-1440.
- [16] M.I. Boulos, P. Fauchais, E. Pfender, *Thermal plasmas: fundamentals and applications*, Springer Science & Business Media 2013.
- [17] K. von Niessen, M. Gindrat, Plasma Spray-PVD: A New Thermal Spray Process to Deposit Out of the Vapor Phase, *Journal of Thermal Spray Technology* 20(4) (2011) 736-743.
- [18] M. Gindrat, J.-L. Dorier, C. Hollenstein, M. Loch, A. Refke, A. Salito, G. Barbezat, Effect of specific operating conditions on the properties of LPPS plasma jets expanding at low pressure, 2001.
- [19] A. Refke, G. Barbezat, J.-L. Dorier, M. Gindrat, C. Hollenstein, Characterization of LPPS processes under various spray conditions for potential applications, 2003.
- [20] W. Mayr, R. Henne, Investigation of a VPS-Burner with Laval Nozzle using an Automated Laser Doppler Measuring System, 1st Plasma Technik symposium, Luzern, 1988, pp. 87-97.
- [21] M. Cao, F. Gitzhofer, D. Gravelle, R. Henne, M. Boulos, A torch nozzle design to improve plasma spraying techniques, *Plasma Sources Science and Technology* 6(1) (1997) 39.
- [22] R. Henne, W. Mayr, A. Reusch, Influence of nozzle geometry on particle behaviour and coating quality in high-velocity VPS, TS 93: Thermal Spraying Conference (Thermische Spritzkonferenz), 1993, pp. 7-11.
- [23] G. Schiller, R.H. Henne, M. Lang, R. Ruckdäschel, S. Schaper, Development of vacuum plasma sprayed thin-film SOFC for reduced operating temperature, *Fuel Cells Bulletin* 3(21) (2000) 7-12.
- [24] G. Mauer, A. Hospach, N. Zotov, R. Vassen, Process Conditions and Microstructures of Ceramic Coatings by Gas Phase Deposition Based on Plasma Spraying, *Journal of Thermal Spray Technology* 22(2-3) (2013) 83-89.

- [25] F. Shao, H. Zhao, C. Liu, X. Zhong, Y. Zhuang, J. Ni, S. Tao, Dense yttria-stabilized zirconia coatings fabricated by plasma spray-physical vapor deposition, *Ceramics International* 43(2) (2017) 2305-2313.
- [26] X. Zhang, K. Zhou, C. Deng, M. Liu, Z. Deng, C. Deng, J. Song, Gas-deposition mechanisms of 7YSZ coating based on plasma spray-physical vapor deposition, *Journal of the European Ceramic Society* 36(3) (2016) 697-703.
- [27] G. Mauer, Plasma Characteristics and Plasma-Feedstock Interaction Under PS-PVD Process Conditions, *Plasma Chemistry and Plasma Processing* 34(5) (2014) 1171-1186.
- [28] A. Refke, G. Barbezat, D. Hawley, R. Schmid, Low pressure plasma spraying(LPPS) as a tool for the deposition of functional SOFC components, *ITSC 2004: International Thermal Spray Conference 2004: Advances in Technology and Application*, 2004, pp. 61-65.
- [29] Oerlikon Mecto, F4-VB Spray Gun Plasma Spraying, 2015. https://www.oerlikon.com/ecomaXL/files/metco/oerlikon_PL_40333_EN_06.pdf&download=1.
- [30] Oerlikon Metco, O3CP Spray Gun Plasma Spraying, 2016. https://www.oerlikon.com/ecomaXL/files/metco/oerlikon_PL-41940-EN-10.pdf&download=1.
- [31] Oerlikon Metco, Solutions Flash ChamPro LPPS Hybrid Technologies for application of unique, high-performance functional surfaces, 2016. https://www.oerlikon.com/ecomaXL/files/oerlikon_SF-0014.2_LPPS-Hybrid_EN.pdf&download=1.
- [32] A. Feuerstein, J. Knapp, T. Taylor, A. Ashary, A. Bolcavage, N. Hitchman, Technical and Economical Aspects of Current Thermal Barrier Coating Systems for Gas Turbine Engines by Thermal Spray and EBPVD: A Review, *Journal of Thermal Spray Technology* 17(2) (2008) 199-213.
- [33] B.K. Pant, V. Arya, B.S. Mann, Development of Low-Oxide MCrAlY Coatings for Gas Turbine Applications, *Journal of Thermal Spray Technology* 16(2) (2007) 275-280.
- [34] D. Naumenko, R. Pillai, A. Chyrkin, W. Quadackers, Overview on recent developments of bondcoats for plasma-sprayed thermal barrier coatings, *Journal of Thermal Spray Technology* 26(8) (2017) 1743-1757.
- [35] A. Scrivani, U. Bardi, L. Carrafiello, A. Lavacchi, F. Niccolai, G. Rizzi, A comparative study of high velocity oxygen fuel, vacuum plasma spray, and axial plasma spray for the deposition of CoNiCrAlY bond coat alloy, *Journal of thermal spray technology* 12(4) (2003) 504-507.

- [36] G. Mauer, M. Jarligo, D. Marcano, S. Rezanka, D. Zhou, R. Vaßen, Recent developments in plasma spray processes for applications in energy technology, IOP Conference Series: Materials Science and Engineering, IOP Publishing, 2017, p. 012001.
- [37] D. Marcano, G. Mauer, R. Vassen, A. Weber, Manufacturing of high performance solid oxide fuel cells (SOFCs) with atmospheric plasma spraying (APS) and plasma spray-physical vapor deposition (PS-PVD), *Surface & Coatings Technology* 318 (2017) 170-177.
- [38] S. Rezanka, G. Mauer, R. Vassen, Improved Thermal Cycling Durability of Thermal Barrier Coatings Manufactured by PS-PVD, *Journal of Thermal Spray Technology* 23(1-2) (2014) 182-189.
- [39] A. Barth, M. Gindrat, S. Usai, High Productivity PS-PVD Process, Proceedings of ITSC 2012,(Houston, USA), *Thermal Spray 2012: Proceedings of the International Thermal Spray Conference, Air, Land, Water, and the Human Body: Thermal Spray Science and Applications*, 2012, pp. 21-24.
- [40] J.L. Dorier, P. Guittienne, C. Hollenstein, M. Gindrat, A. Refke, Mechanisms of films and coatings formation from gaseous and liquid precursors with low pressure plasma spray equipment, *Surface and Coatings Technology* 203(15) (2009) 2125-2130.
- [41] M. Gindrat, H.M. Höhle, K. von Niessen, P. Guittienne, D. Grange, C. Hollenstein, Plasma Spray-CVD: A New Thermal Spray Process to Produce Thin Films from Liquid or Gaseous Precursors, *Journal of Thermal Spray Technology* 20(4) (2011) 882-887.
- [42] P. Fauchais, G. Montavon, R. Lima, B. Marple, Engineering a new class of thermal spray nano-based microstructures from agglomerated nanostructured particles, suspensions and solutions: an invited review, *Journal of Physics D: Applied Physics* 44(9) (2011) 093001.
- [43] H. Chen, C. Ding, Nanostructured zirconia coating prepared by atmospheric plasma spraying, *Surface and Coatings Technology* 150(1) (2002) 31-36.
- [44] H. Kassner, R. Siegert, D. Hathiramani, R. Vassen, D. Stoeber, Application of suspension plasma spraying (SPS) for manufacture of ceramic coatings, *Journal of Thermal Spray Technology* 17(1) (2008) 115-123.
- [45] P. He, H. Sun, Y. Gui, F. Lapostolle, H. Liao, C. Coddet, Microstructure and properties of nanostructured YSZ coating prepared by suspension plasma spraying at low pressure, *Surface and Coatings Technology* 261 (2015) 318-326.

- [46] P. Fauchais, R. Etchart-Salas, V. Rat, J.-F. Coudert, N. Caron, K. Wittmann-Ténèze, Parameters controlling liquid plasma spraying: Solutions, sols, or suspensions, *Journal of Thermal Spray Technology* 17(1) (2008) 31-59.
- [47] Z. Chen, R.W. Trice, M. Besser, X. Yang, D. Sordelet, Air-plasma spraying colloidal solutions of nanosized ceramic powders, *Journal of materials science* 39(13) (2004) 4171-4178.
- [48] R.S. Lima, B.R. Marple, Thermal spray coatings engineered from nanostructured ceramic agglomerated powders for structural, thermal barrier and biomedical applications: a review, *Journal of Thermal Spray Technology* 16(1) (2007) 40-63.
- [49] L. Pawlowski, Suspension and solution thermal spray coatings, *Surface and Coatings Technology* 203(19) (2009) 2807-2829.
- [50] Suspension Plasma Spray (SPS). See Suspension Plasma Spray (SPS) at <https://users.encs.concordia.ca/~dolat/Research-TS-Processes.html>.
- [51] F. Toma, G. Bertrand, R. Rampon, D. Klein, C. Coddet, C. Meunier, Relationship between the suspension properties and liquid plasma sprayed coating characteristics, *Proc. 2006 Internat. Thermal Spray Conf*, 2006.
- [52] J. Fazilleau, C. Delbos, V. Rat, J.-F. Coudert, P. Fauchais, B. Pateyron, Phenomena involved in suspension plasma spraying part 1: Suspension injection and behavior, *Plasma chemistry and plasma processing* 26(4) (2006) 371-391.
- [53] W. Fan, Y. Bai, Review of suspension and solution precursor plasma sprayed thermal barrier coatings, *Ceramics International* (2016).
- [54] R. Rampon, C. Filiatre, G. Bertrand, Suspension Plasma Spraying of YPSZ Coatings: Suspension Atomization and Injection, *Journal of Thermal Spray Technology* 17(1) (2008) 105-114.
- [55] P. Fauchais, R. Etchart-Salas, C. Delbos, M. Tognonvi, V. Rat, J.-F. Coudert, T. Chartier, Suspension and solution plasma spraying of finely structured layers: potential application to SOFCs, *Journal of Physics D: Applied Physics* 40(8) (2007) 2394.
- [56] C. Delbos, J. Fazilleau, V. Rat, J.-F. Coudert, P. Fauchais, B. Pateyron, Phenomena involved in suspension plasma spraying Part 2: Zirconia particle treatment and coating formation, *Plasma chemistry and plasma processing* 26(4) (2006) 393-414.
- [57] P. Fauchais, G. Montavon, Latest Developments in Suspension and Liquid Precursor Thermal Spraying, *Journal of Thermal Spray Technology* 19(1) (2010) 226-239.

- [58] E.H. Jordan, C. Jiang, M. Gell, The solution precursor plasma spray (SPPS) process: a review with energy considerations, *Journal of Thermal Spray Technology* 24(7) (2015) 1153-1165.
- [59] X. Chen, E. Pfender, Effect of the Knudsen number on heat transfer to a particle immersed into a thermal plasma, *Plasma chemistry and plasma processing* 3(1) (1983) 97-113.
- [60] T. Bhatia, A. Ozturk, L. Xie, E.H. Jordan, B.M. Cetegen, M. Gell, X. Ma, N.P. Padture, Mechanisms of ceramic coating deposition in solution-precursor plasma spray, *Journal of materials research* 17(9) (2002) 2363-2372.
- [61] K. VanEvery, M.J.M. Krane, R.W. Trice, Parametric study of suspension plasma spray processing parameters on coating microstructures manufactured from nanoscale yttria-stabilized zirconia, *Surface and Coatings Technology* 206(8) (2012) 2464-2473.
- [62] F. Tarasi, M. Medraj, A. Dolatabadi, J. Oberste-Berghaus, C. Moreau, Effective Parameters in Axial Injection Suspension Plasma Spray Process of Alumina-Zirconia Ceramics, *Journal of Thermal Spray Technology* 17(5) (2008) 685-691.
- [63] E.M. Cotler, D. Chen, R.J. Molz, Pressure-Based Liquid Feed System for Suspension Plasma Spray Coatings, *Journal of Thermal Spray Technology* 20(4) (2011) 967-973.
- [64] R. Vassen, H. Kassner, G. Mauer, D. Stover, Suspension Plasma Spraying: Process Characteristics and Applications, *Journal of Thermal Spray Technology* 19(1-2) (2010) 219-225.
- [65] A. Ganvir, S. Joshi, N. Markocsan, R. Vassen, Tailoring columnar microstructure of axial suspension plasma sprayed TBCs for superior thermal shock performance, *Materials & Design* (2018).
- [66] A. Cattini, L. Łatka, D. Bellucci, G. Bolelli, A. Sola, L. Lusvarghi, L. Pawłowski, V. Cannillo, Suspension plasma sprayed bioactive glass coatings: Effects of processing on microstructure, mechanical properties and in-vitro behaviour, *Surface and Coatings Technology* 220 (2013) 52-59.
- [67] F.-L. Toma, G. Bertrand, S. Begin, C. Meunier, O. Barres, D. Klein, C. Coddet, Microstructure and environmental functionalities of TiO₂-supported photocatalysts obtained by suspension plasma spraying, *Applied Catalysis B: Environmental* 68(1-2) (2006) 74-84.
- [68] J.O. Berghaus, B. Marple, C. Moreau, Suspension plasma spraying of nanostructured WC-12Co coatings, *Journal of Thermal Spray Technology* 15(4) (2006) 676-681.

- [69] P. Fauchais, V. Rat, C. Delbos, J.F. Coudert, T. Chartier, L. Bianchi, Understanding of suspension DC plasma spraying of finely structured coatings for SOFC, *IEEE transactions on plasma science* 33(2) (2005) 920-930.
- [70] P. Sokołowski, S. Kozerski, L. Pawłowski, A. Ambroziak, The key process parameters influencing formation of columnar microstructure in suspension plasma sprayed zirconia coatings, *Surface and Coatings Technology* 260 (2014) 97-106.
- [71] N. Curry, Z. Tang, N. Markocsan, P. Nylén, Influence of bond coat surface roughness on the structure of axial suspension plasma spray thermal barrier coatings—Thermal and lifetime performance, *Surface and Coatings Technology* 268 (2015) 15-23.
- [72] J.O. Berghaus, S. Bouaricha, J. Legoux, C. Moreau, Injection conditions and in-flight particle states in suspension plasma spraying of alumina and zirconia nano-ceramics, *Proceedings of the International Thermal Spray Conference*, May, 2005, pp. 2-4.
- [73] K. VanEvery, M.J. Krane, R.W. Trice, H. Wang, W. Porter, M. Besser, D. Sordelet, J. Ilavsky, J. Almer, Column formation in suspension plasma-sprayed coatings and resultant thermal properties, *Journal of thermal spray technology* 20(4) (2011) 817-828.
- [74] A. Ganvir, N. Curry, N. Markocsan, P. Nylén, F.-L. Toma, Comparative study of suspension plasma sprayed and suspension high velocity oxy-fuel sprayed YSZ thermal barrier coatings, *Surface and Coatings Technology* 268 (2015) 70-76.
- [75] P. Fauchais, M. Vardelle, A. Vardelle, S. Goutier, What Do We Know, What are the Current Limitations of Suspension Plasma Spraying?, *Journal of Thermal Spray Technology* 24(7) (2015) 1120-1129.
- [76] P. Fauchais, M. Vardelle, S. Goutier, A. Vardelle, Key Challenges and Opportunities in Suspension and Solution Plasma Spraying, *Plasma Chemistry and Plasma Processing* 35(3) (2015) 511-525.
- [77] N. Schlegel, S. Ebert, G. Mauer, R. Vassen, Columnar-Structured Mg-Al-Spinel Thermal Barrier Coatings (TBCs) by Suspension Plasma Spraying (SPS), *Journal of Thermal Spray Technology* 24(1-2) (2015) 144-151.
- [78] P. Sokołowski, L. Pawłowski, D. Dietrich, T. Lampke, D. Jech, Advanced Microscopic Study of Suspension Plasma-Sprayed Zirconia Coatings with Different Microstructures, *Journal of Thermal Spray Technology* 25(1-2) (2015) 94-104.
- [79] D. Zhou, O. Guillon, R. Vaßen, Development of YSZ Thermal Barrier Coatings Using Axial Suspension Plasma Spraying, *Coatings* 7(8) (2017) 120.

- [80] D. Waldbillig, O. Kesler, Characterization of metal-supported axial injection plasma sprayed solid oxide fuel cells with aqueous suspension plasma sprayed electrolyte layers, *Journal of Power Sources* 191(2) (2009) 320-329.
- [81] M. Shahien, M. Suzuki, USING AN AXIAL FEEDING DC-PLASMA SPRAY GUN FOR FABRICATION OF CERAMIC COATINGS, *Advances in High Temperature Ceramic Matrix Composites and Materials for Sustainable Development* 263 (2017) 479.
- [82] P. He, Etude du développement de la projection plasma sous très basse pression, Belfort-Montbéliard, 2014.
- [83] J.D. Fleetwood, Solid oxide fuel cell electrolytes produced via very low pressure suspension plasma spray and electrophoretic deposition, Purdue University, 2014.
- [84] Y. Yang, D. Yan, Y. Dong, L. Wang, X. Chen, J. Zhang, J. He, X. Li, In situ nanostructured ceramic matrix composite coating prepared by reactive plasma spraying micro-sized Al-Fe₂O₃ composite powders, *Journal of Alloys and Compounds* 509(5) (2011) L90-L94.
- [85] J. Xu, B. Zou, X. Fan, S. Zhao, Y. Hui, Y. Wang, X. Zhou, X. Cai, S. Tao, H. Ma, Reactive plasma spraying synthesis and characterization of TiB₂-TiC-Al₂O₃/Al composite coatings on a magnesium alloy, *Journal of Alloys and Compounds* 596 (2014) 10-18.
- [86] B. Zou, S. Tao, W. Huang, Z.S. Khan, X. Fan, L. Gu, Y. Wang, J. Xu, X. Cai, H. Ma, Synthesis and characterization of in situ TiC-TiB₂ composite coatings by reactive plasma spraying on a magnesium alloy, *Applied Surface Science* 264 (2013) 879-885.
- [87] L. Zhao, E. Lugscheider, Reactive plasma spraying of TiAl₆V₄ alloy, *Wear* 253(11) (2002) 1214-1218.
- [88] L. Zhu, J. He, D. Yan, L. Xiao, Y. Dong, J. Zhang, H. Liao, Synthesis and microstructure observation of titanium carbonitride nanostructured coatings using reactive plasma spraying in atmosphere, *Applied Surface Science* 257(20) (2011) 8722-8727.
- [89] R. Smith, Z. Mutasim, Reactive plasma spraying of wear-resistant coatings, *Journal of Thermal Spray Technology* 1(1) (1992) 57-63.
- [90] L. Xiao, D. Yan, J. He, L. Zhu, Y. Dong, J. Zhang, X. Li, Nanostructured TiN coating prepared by reactive plasma spraying in atmosphere, *Applied Surface Science* 253(18) (2007) 7535-7539.

- [91] C. Song, M. Liu, Z.-Q. Deng, S.-P. Niu, C.-M. Deng, H.-L. Liao, A novel method for in-situ synthesized TiN coatings by plasma spray-physical vapor deposition, *Materials Letters* 217 (2018) 127-130.
- [92] T. Valente, F. Carassiti, M. Suzuki, M. Tului, High pressure reactive plasma spray synthesis of titanium nitride based coatings, *Surface Engineering* 16(16) (2000) 339-343.
- [93] Y. Qin, G. Zheng, L. Zhu, J. He, F. Zhang, Y. Dong, F. Yin, Structure and wear characteristics of TiCN nanocomposite coatings fabricated by reactive plasma spraying, *Surface and Coatings Technology* (2018).
- [94] P.B. Mi, J.N. He, Y.F. Qin, K. Chen, Nanostructure reactive plasma sprayed TiCN coating, *Surface & Coatings Technology* 309 (2017) 1-5.
- [95] R. Licheri, R. Orru, G. Cao, A. Crippa, R. Scholz, Self-propagating combustion synthesis and plasma spraying deposition of TiC–Fe powders, *Ceramics International* 29(5) (2003) 519-526.
- [96] P. Ananthapadmanabhan, P.R. Taylor, Titanium carbide–iron composite coatings by reactive plasma spraying of ilmenite, *Journal of Alloys and Compounds* 287(1-2) (1999) 121-125.
- [97] C. Tekmen, Y. Tsunekawa, M. Okumiya, In-situ TiB₂–Al₂O₃ formed composite coatings by atmospheric plasma spraying: Influence of process parameters and in-flight particle characteristics, *Surface and Coatings Technology* 203(12) (2009) 1649-1655.
- [98] W. Feng, D. Yan, J. He, G. Zhang, G. Chen, W. Gu, S. Yang, Microhardness and toughness of the TiN coating prepared by reactive plasma spraying, *Applied Surface Science* 243(1–4) (2005) 204-213.
- [99] M. Shahien, M. Yamada, T. Yasui, M. Fukumoto, Fabrication of AlN coatings by reactive atmospheric plasma spray nitriding of Al powders, *Materials transactions* 51(5) (2010) 957-961.
- [100] B. Vautherin, M.P. Planche, A. Quet, L. Bianchi, G. Montavon, Manufacturing of composite titanium-titanium nitride coatings by reactive very low pressure plasma spraying (R-VLPPS), *Journal of Physics: Conference Series* 550(1) (2014) 12035-12044.
- [101] L. Zhu, N. Zhang, B. Zhang, R. Bolot, H. Liao, C. Coddet, In Situ Synthesis of FeAl Dense Coatings by Very Low Pressure Reactive Plasma Spraying, *Journal of Thermal Spray Technology* 22(2) (2013) 90-95.
- [102] T.C. Totemeier, R.N. Wright, W.D. Swank, FeAl and Mo–Si–B intermetallic coatings prepared by thermal spraying, *Intermetallics* 12(12) (2004) 1335-1344.

- [103] T. Skiba, P. Haušild, M. Karlík, K. Vanmeensel, J. Vleugels, Mechanical properties of spark plasma sintered FeAl intermetallics, *Intermetallics* 18(7) (2010) 1410-1414.

CHAPTER 2

Experimental and Testing Equipment

Chapter 2 Experimental and Testing Equipment

2.1 Experimental Equipment

For the cooperation between the joint laboratories, the coating experiments in this study were performed using two pieces of LPPS equipment. The first was the LPPS equipment in the LERMPS lab (UTBM, Belfort, France), which prepared the YSZ coating using LP-SPS and LPPS. The other was the PS-PVD equipment in the Guangdong Institute of New Materials (Guangzhou, China), which fabricated the TiN coating using LP-RPS.

2.1.1 LPPS Equipment

The LERMPS laboratory started its LPPS technology research over ten years ago. The first LPPS installation was standard production equipment marketed by PLASMA-TECHNIK AG, that could deposit the coating under very low pressure, e.g., <1 mbar [1]. To better fit the long plasma jet caused by the very low pressure, the chamber volume of the original LPPS system was enlarged by Sokolov [2] and is now double the original size (i.e., from 6 m^3 to 12 m^3). The appearance of the LPPS system after modification is demonstrated in Figure 2.1.

By using two pumping groups adjusted by a control panel, the LPPS system allows the operation pressure to vary from 150 Pa to 5000 Pa. The plasma torch for spraying is mounted on a programmable 6-axis robot (ABB IRB 1400), and a rotary table is also available as an additional axis to produce the multi-angle spray. During the spraying, the substrate temperature can be measured by an IRCON monochromatic infrared pyrometer ($\lambda=1.6 \mu\text{m}$), which is installed outside the vacuum chamber. Other diagnostic equipment such as an optical emission spectrometer can also be set up on the flange of the chamber wall.



Figure 2.1 The LPPS system made by the LERMPS [3].

A bi-cathode plasma torch designed for LPPS

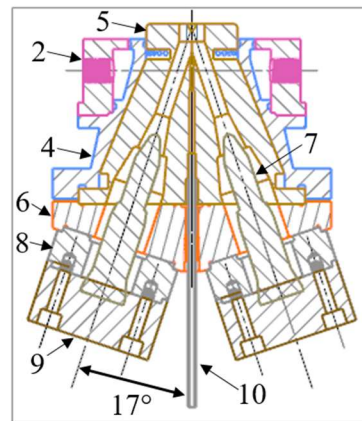
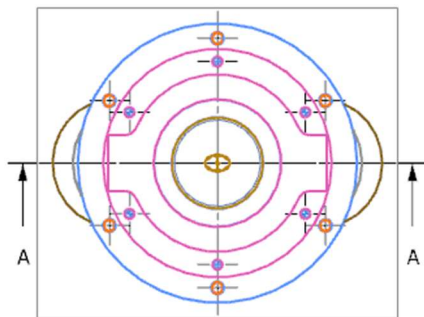
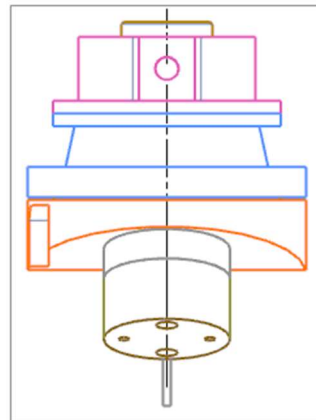
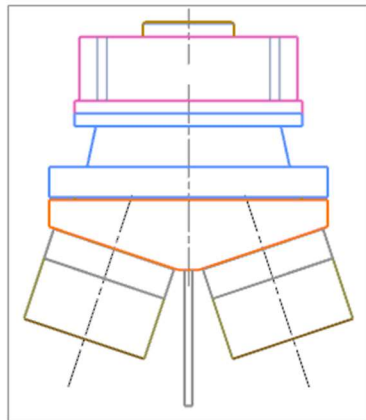
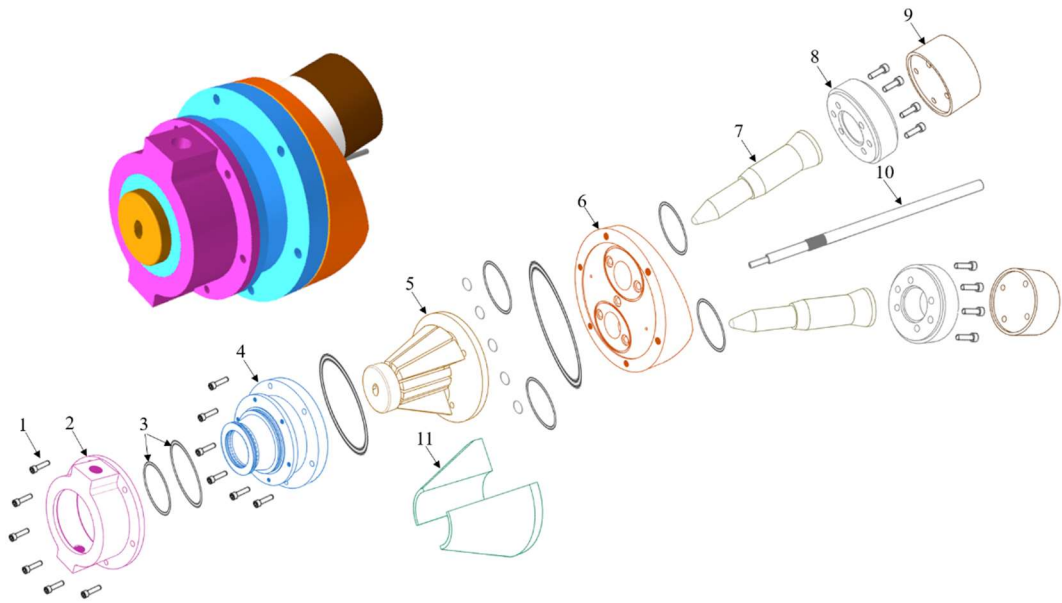
As mentioned in Chapter 1, on the one hand, the commercial LPPS plasma torch at present usually applies the radial injection mode, which is impossible to send the very fine particles or suspension into the expanding, high-temperature and high-velocity plasma jet without disturbing it. Therefore, the feedstock injection is always a troublesome issue for the LPPS process. To solve the problem, applying a plasma torch with an axial injection mode is undoubtedly a suitable method. On the other hand, the heat and momentum transfer of the LPPS process is much weaker than the APS process due to the rarefied environment. It means that the powders will be more difficult to be heated and accelerated under low pressure. In this case, a high-power plasma torch should be adopted to compensate for the insufficient ability of heating and acceleration. Based on these points, the LERMPS lab proposed to develop a novel axial bi-cathode plasma torch to solve the problem mentioned above. The ultimate goal of the design is to obtain high-quality coatings by injecting very fine particles or suspension into the plasma center with a relatively high input plasma power.

The three-dimensional model and three-view drawing of the new plasma torch is presented in Figure 2.2. The corresponding component information is listed in Table 2.1. The basic design concept is to combine two commercial F4 type plasma torch. For supporting the torch design, two consoles, and two power supplies are applied, which allows the power of the plasma torch to reach 81kW. The new torch

directly inherits the cathode (7), the insulating intermediate body (8), and the rear body (9) of the original F4 type plasma torch, but redesigns the anode retainer (2, 4), the anode (5), the center body (6), and the diversion block (11). Specifically, two individual F4 cathodes (7) are arranged on the center body (6) around a suspension injector (10) with an angle of 17° . The choice of this angle is derived from another tri-cathode plasma torch previously used by the LERMPS laboratory [4]. A shared anode (5) is positioned at the opposite end of the center body (6), acting as a nozzle for the two F4 type cathodes (7). The machining dimensions of the center body (6) are carefully controlled to guarantee the relative position between the anode (5) and the cathode (7). Because this relative position is significant for generating the electric arc and maintaining the symmetry of the plasma jet. Furthermore, to ensure the effective cooling of the anode (5) and prolong its service life, partial anode material that perpendicular to the planes of the two cathodes (7) is removed. With the plasma gases fed behind the F4 cathodes (7), two plasma jets can be generated separately, and then converge in the axis of the anode (5). After that, the feedstock of both powders and suspensions can be axially injected into the center of the converging plasma jet under low pressure. As a result, the heat transfer and the fusion of high melting point material will be effectively enhanced because the torch center has the highest plasma temperature and density. However, the axial injection also has a problem that is easy to clog the anode (5). Taking this into account, the anode (5) adopts a diverging design at the exit, which can not only avoid the sprayed material sticking to its inner wall but also improve the jet flow under low pressure.

Furthermore, as the new torch have a relatively high plasma power, it will cause serious erosion of the anode (5) and the cathode (7). To protect them, two cooling water systems are connected to the anode retainer top (2), which has two inlets on both sides. When the distilled water is injected into the anode retainer top (2), it will first fill the tiny reservoir inside the retainer, and then evenly flows into the anode (5) through a series of small round holes at the neck of the anode retainer bottom (4).

With the aim of better cooling the high-temperature area of the anode (5), two additional diversion blocks (11) are positioned next to the anode (5) to restrict the water to flow close to the anode (5). As a result, the anode (5) can be uniformly cooled with being strongly heated by the high-temperature plasma jet. Finally, the cooling water exits the plasma torch through four outlets in the center body (6). To avoid excess energy loss, the diameter of all the water outlets is chosen the same as the size of the F4 plasma torch. During the water-cooling process, several O-rings (3) are used to prevent the water from leaking. In addition, all components are coated with a layer of insulating varnish to avoid the arc striking outside the torch under low pressure.



SECTION A-A

Figure 2.2 The 3D model (top) and three-view drawing (bottom) of the bi-cathode plasma torch designed for LPPS.

Table 2.1 Parts list of the bi-cathode plasma torch

Item number	Description	Materials	Quantity
1	Cap screws with difference sizes	Stainless Steel	24
2	Anode retainer top	Copper	1
3	O-rings with difference sizes	Rubber	13
4	Anode retainer bottom	Copper	1
5	Anode	Copper	1
6	Center body	Copper	1
7	F4 Cathode	-	2
8	Insulating intermediate body	-	2
9	Rear body	-	2
10	Suspension injector	Stainless Steel	1
11	Diversion block	Peek	2

2.1.2 PS–PVD Equipment

The PS–PVD equipment at the Guangdong Institute of New Materials (GINM) is a MultiCoat™ hybrid plasma coating system (Oerlikon Metco, Switzerland) that was installed in 2014. Due to its strengthened vacuum pumping unit, this system can operate under the very low pressure of 50 Pa. Moreover, a high plasma gas flow of 200 L/min and a maximal power input of 180 kW can be achieved by using a modified single cathode of the O3CP plasma torch. In addition, the F4-VB torch can be operated in the system.

By using this equipment, it is expected to improve the reacting degree of the conventional reactive plasma spray with the long plasma jet of high power and prevent the oxidation of the resulting coating by controlling the atmosphere.



Figure 2.3 The MultiCoat™ hybrid plasma-coating system at GINM [5].

2.2 Testing Equipment

2.2.1 Optical Emission Spectroscopy

Unlike conventional thermal spray processes, the LPPS technique can partially or even completely vaporize the injected materials by using specific parameters. As a result, conventional diagnostic techniques, such as the DPV-2000, are no longer applicable as these are based on detecting solid or liquid particles. Therefore, other diagnostic tools have had to be developed to characterize the LPPS process [6]. Among them, the optical emission spectroscopy (OES) technology as a non-intrusive detecting method is a good alternative. The fundamental principle of this technology is based on the following points:

- The excited atoms or ions create an emission spectrum after their transition from a high energy state to a low energy state.
- Each element produces unique characteristic emission spectral lines, due to the different atomic energy levels. The qualitative analysis of the elements can be performed by measuring the existence of the spectrum.

- The spectral intensity of each emission spectrum is proportional to the concentration of the element. The quantitative analysis of the elements can be implemented by measuring the intensity of the spectrum.

According to the principles mentioned above, OES can be used to characterize the plasma jet properties under low pressure. For instance, it can calculate the electron temperature and density of plasma [7]. Moreover, OES can check whether specific plasma parameters under low pressure have a measurable influence on the injected material. For example, it can analyze whether the injected material is vaporized [8].

In this study, a Jobin-Yvon spectrometer (type TRIAX190, UK) with a charge-coupled device (CCD) 3000 detector (Figure 2.4) was installed on the LPPS equipment to detect the spectrums emitted by the plasma and the vapor phase from the materials, as shown in Figure 2.5 [7]. The measurement was performed perpendicular to the axis of the plasma jet with a focal length of 190 mm. The optical sensor was mounted inside a specially designed tube equipped with a cooling system to avoid the sensor head being overheated by the plasma jet during the measurements.

The detailed specifications of the Jobin-Yvon Triax 190 are shown in Table 2.1. Before the experiment, the calibrations for the spectral wavelength, full width at the half-maximum, and intensities were carried out. A mercury lamp was used to ensure the CCD focusing and alignment. For the measurement, the light signals were first collected by the sensor and transferred through the optical fiber to the entrance slit (6 μm). The spectrometer then split the light into a spectrum using 1200 grooves/mm diffraction grating and the CCD detector with 1024×256 pixels collected the spectrum, converted it to an electrical signal, and sent it to the computer data acquisition system. Finally, the result could be displayed and analyzed with the SpectraMax and Plasus Specline software. All the spectral data for the analysis were from the National Institute of Standards and Technology [9].

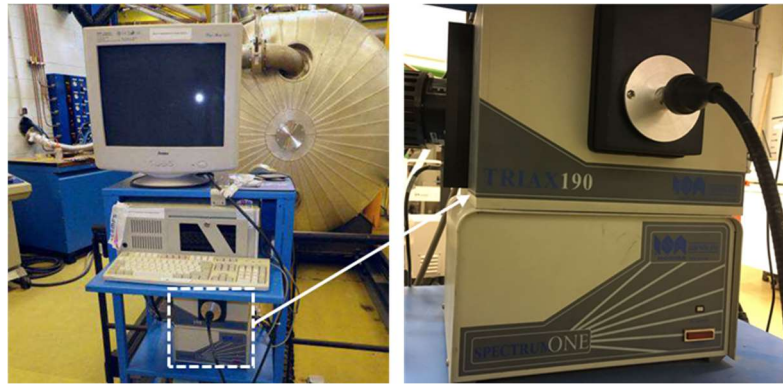


Figure 2.4 Jobin-Yvon Triax 190 optical emission spectrometer.

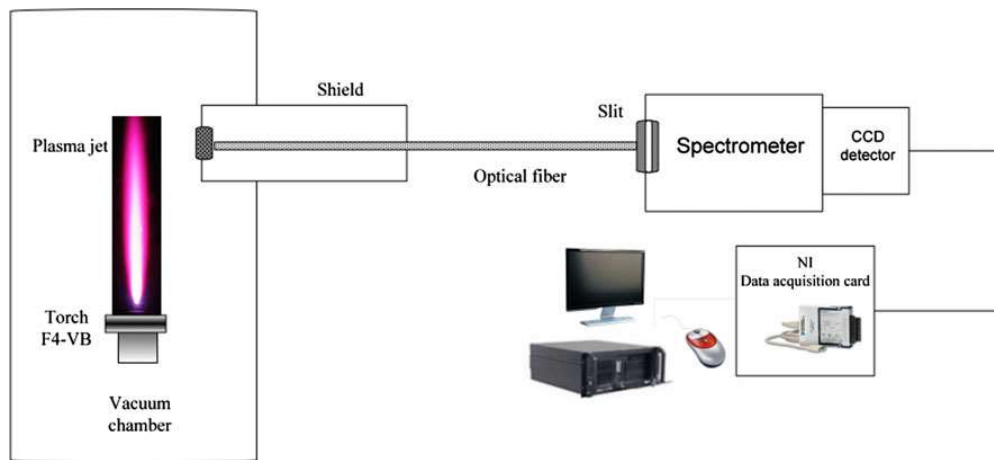


Figure 2.5 Schematic of the OES measuring process in the LPPS system [7].

Table 2.2 Technical specifications for the Jobin-Yvon Triax 190.

Focal length	190 mm
Entrance aperture ratio	F/3.9
Grating size	50 mm × 50 mm
Scanning range with 1200 gr/mm grating	300–900 nm
Spectral dispersion with 1200 gr/mm grating	3.53 nm/mm
Spectral resolution with 1200 gr/mm grating	0.3 nm
Wavelength positioning accuracy/ repeatability	± 0.3 nm/± 0.06 nm

2.2.2 X-Ray Diffraction

2.2.2.1 Qualitative Analysis

X-ray diffraction (XRD) is a routine, nondestructive technique used to characterize the phase composition and crystal structure of powders and coatings [10]. When a monochromatic X-ray beam with a single wavelength strikes the material, the X-ray is scattered in all directions. Most of the scatterings will cancel each other out because of the destructive interference and only specific crystal planes at specific angles cause constructive reinforcement of the beam. This phenomenon is called diffraction, which satisfies Bragg's law (see Figure 2.6):

$$n\lambda = 2d_{hkl}\sin\theta \quad (2-1)$$

where n is an integer number, λ is the wavelength of the x-ray, d_{hkl} is the interplanar spacing with the same Miller indices (h, k, l) that cause constructive reinforcement of the beam, and θ is half the angle between the original beam direction and the diffracted beam.

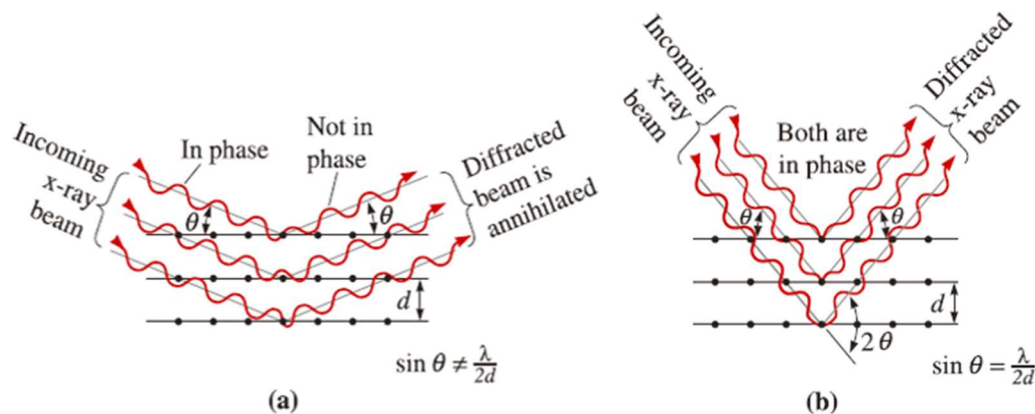


Figure 2.6 (a) Destructive and (b) reinforcing interactions between x-rays and the crystalline material. Reinforcement occurs at angles that satisfy Bragg's law [11].

During XRD testing, there are always crystals in materials with d_{hkl} oriented at the proper angle to satisfy Bragg's law. Therefore, a diffracted beam, making an angle of 2θ with the incident beam, is produced. In a diffractometer, a moving X-ray detector records the 2θ angles and the corresponding diffraction intensity at which

the beam is diffracted, giving a characteristic diffraction pattern (see Figure 2.7). This special pattern has the following characteristics:

- Each phase has a characteristic diffraction pattern.
- The diffraction pattern of any two phases cannot be the same.
- The diffraction pattern of a multiphase sample is the culmination of the individual patterns.

Based on these characteristics, the phase composition of powders and coatings can be identified by comparing the detecting pattern with the standard data from the literature. The reference data are that of the Joint Committee Powder Diffraction Standard (J.C.P.D.S.).

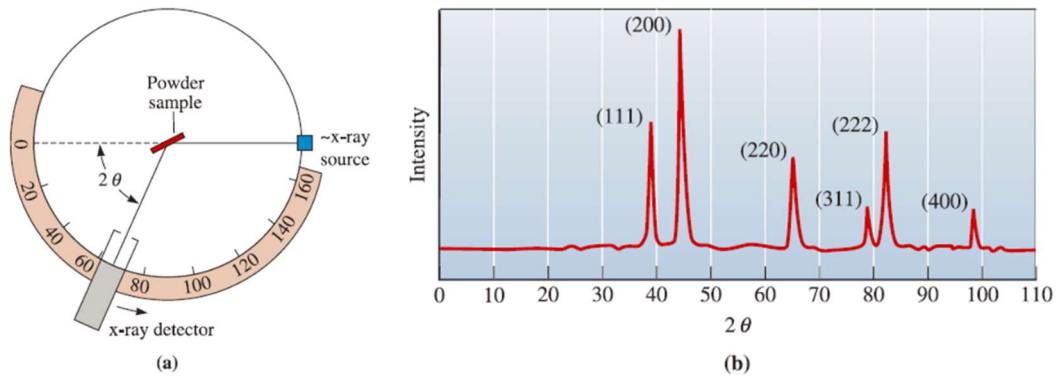


Figure 2.7 (a) Diagram of a diffractometer, showing powder sample, incident, and diffracted beams (b) The diffraction pattern obtained from a sample of gold powder [11].

2.2.2.2 Quantitative Analysis

XRD is also used to quantitatively analyze powders and coatings, e.g., to estimate the average grain size and calculate the content of the phase.

For the powders and coatings, the average grain size can be estimated using the Williamson-Hall equation [12-14]:

$$\beta \cos \theta = \frac{K\lambda}{D} + 4\epsilon \sin \theta \quad (2-2)$$

where β is the peak width of the diffraction peak profile at half the maximum height resulting from small crystallite size in radians, θ is the Bragg angle in degrees, K is a dimensionless shape factor related to crystallite shape with a typical value of about

0.9, λ is the X-ray wavelength in nanometers, ε is the strain factor, and D is the mean size of the grains in nanometers.

The content of a phase can be calculated based on the method of reference intensity ratio (RIR), which is based on the adiabatic principle [15]:

$$X_i = \left(\frac{k_i \sum_{i=1}^n I_i}{I_i k_i} \right)^{-1} \quad (2-3)$$

where X_i is the mass fraction of i phase, k_i is a factor containing the mass absorption coefficient of the sample, I_i is the integrated intensity of the i phase, and n is the number of phases.

In this study, the characterization of powders and coatings was performed on two machines, i.e., a Bruker AXS-D8 Focus X-ray diffractometer (Germany) equipped with Co K α radiation ($\lambda = 1.7889 \text{ \AA}$); a Rigaku SmartLab X-ray diffractometer (Japan) with Cu K α radiation ($\lambda = 1.5418 \text{ \AA}$). To identify the phases, an angular range of 20 to 80 $^\circ$ (in 2θ) was scanned with a speed of 4 $^\circ$ /min.

2.2.3 Optical and Scanning Electron Microscopy

As a fast observation method, the metallographic structures of coatings were examined after polishing using a Nikon (Japan) optical microscope. This device has a wide range of observation and can give the natural color of the specimen at 1000 times magnification.

For higher magnification, two field emission scanning electron microscopes were used to characterize the morphology of the powders and coatings: a JSM-7800F (JEOL, Japan) and a Nova nanoSEM 450 (FEI, USA). The observations could be made at different magnifications in secondary electrons or backscattered electrons mode. In addition, the SEM was equipped with an energy dispersive spectrometer (EDS) to enable the qualitative or semi-quantitative elemental analysis in a point on a line or a full screen. Before the observation of powders and insulating coatings, pre-gold metallization or carbon vaporization was performed using a SCD005/CEA035 sputter coater (BAL-TEC, Switzerland).

2.2.4 Nanoindentation

The traditional indentation test (macro or micro-indentation) is limited for the measurement of thin coatings due to the large and varied tip shapes. In contrast, nanoindentation can improve the micro-indentation test by indenting on the nanoscale with a very precise tip shape. During the indentation process, a record of the load and depth of penetration can be measured as a typical load-displacement curve, as shown in Figure 2.8 where P_{max} is the maximum load, h_{max} is the maximum displacement relative to the initial under-formed surface, S is the contact stiffness, and h_f is the final depth.

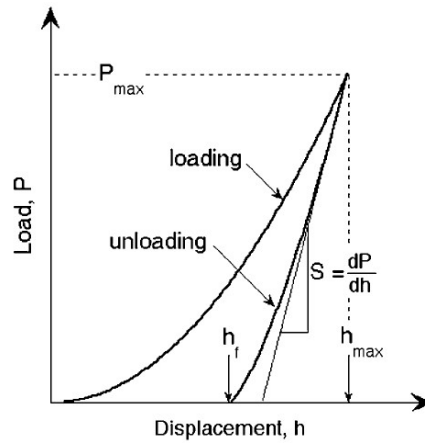


Figure 2.8 The schematic of the load-displacement curve for an instrumented nanoindentation test [16].

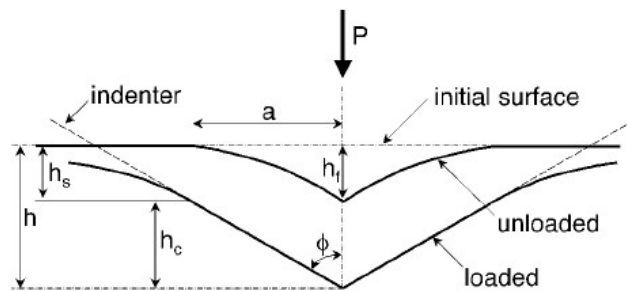


Figure 2.9 The schematic of the unloading process showing parameters characterizing the contact geometry [16].

The hardness H and elastic modulus E can be calculated based on the unloading processes, as shown in Figure 2.9 [16]. The hardness H is estimated from:

$$H = \frac{P_{max}}{A(h_c)} \quad (2-4)$$

where P_{max} is the peak indentation load and $A(h_c)$ is the projected area of the indentation at the contact depth h_c .

$$E_r = \frac{S}{2\beta} \sqrt{\frac{\pi}{A(h_c)}} \quad (2-5)$$

where β is a geometrical constant on the order of unity and E_r is the effective elastic modulus defined by:

$$\frac{1}{E_r} = \frac{1-\nu^2}{E} + \frac{1-\nu_i^2}{E_i} \quad (2-6)$$

where E and ν are Young's modulus and Poisson's ratio for the coatings. E_i and ν_i are the same parameters for the indenter. For general material, ν is typically around 0.3, and for a diamond indenter tip, E_i is 1140 GPa and ν_i is 0.07.

In this study, A Hysitron nanoindenter system (Hysitron, Minneapolis, MN, USA) was used to perform nanoindentation. A Berkovich tip with a tip angle of 140° and a tip radius of approximately 100–200 nm was employed.

References

- [1] Z. Salhi, D. Klein, P. Gougeon, C. Coddet, Development of coating by thermal plasma spraying under very low-pressure condition < 1 mbar, *Vacuum* 77(2) (2005) 145-150.
- [2] D. Sokolov, Contribution au développement de la projection thermique à très faible pression, Université de Technologie de Belfort-Montbéliard, 2009.
- [3] B. Vautherin, M.P. Planche, A. Quet, L. Bianchi, G. Montavon, Manufacturing of composite titanium-titanium nitride coatings by reactive very low pressure plasma spraying (R-VLPPS), *Journal of Physics: Conference Series* 550(1) (2014) 12035-12044.
- [4] P. He, Etude du développement de la projection plasma sous très basse pression, Belfort-Montbéliard, 2014.
- [5] J. Mao, Z. Deng, M. Liu, C. Deng, J. Song, K. Yang, Regional characteristics of YSZ coating prepared by expanded Ar/He/H plasma jet at very low pressure, *Surface and Coatings Technology* 328 (2017) 240-247.
- [6] A. Refke, M. Gindrat, S.M. AG, Process Characterization of LPPS Thin Film Processes with Optical Diagnostics, *Thermal Spray 2007: Global Coating Solutions*, Beijing, China, 2007.
- [7] N. Zhang, F. Sun, L. Zhu, M.P. Planche, H. Liao, C. Dong, C. Coddet, Electron Temperature and Density of the Plasma Measured by Optical Emission Spectroscopy in VLPPS Conditions, *Journal of Thermal Spray Technology* 20(6) (2011) 1321-1327.
- [8] K. von Niessen, M. Gindrat, Plasma Spray-PVD: A New Thermal Spray Process to Deposit Out of the Vapor Phase, *Journal of Thermal Spray Technology* 20(4) (2011) 736-743.
- [9] NIST Atomic Spectra Database Lines Form. https://physics.nist.gov/PhysRefData/ASD/lines_form.html.
- [10] ASM International (2008) ASM handbook, vol 10, 8th edn, Materials characterization. ASM International, Materials Park, OH.
- [11] D.R. Askeland, W.J. Wright, Science and engineering of materials, Nelson Education 2015.
- [12] A.K. Zak, W.A. Majid, M.E. Abrishami, R. Yousefi, X-ray analysis of ZnO nanoparticles by Williamson–Hall and size–strain plot methods, *Solid State Sciences* 13(1) (2011) 251-256.

- [13] G. Williamson, W. Hall, X-ray line broadening from filed aluminium and wolfram, *Acta metallurgica* 1(1) (1953) 22-31.
- [14] V. Mote, Y. Purushotham, B. Dole, Williamson-Hall analysis in estimation of lattice strain in nanometer-sized ZnO particles, *Journal of Theoretical and Applied Physics* 6(1) (2012) 6.
- [15] F.H. Chung, Quantitative interpretation of X-ray diffraction patterns of mixtures. II. Adiabatic principle of X-ray diffraction analysis of mixtures, *Journal of Applied Crystallography* 7(6) (1974) 526-531.
- [16] W.C. Oliver, G.M. Pharr, Measurement of hardness and elastic modulus by instrumented indentation: Advances in understanding and refinements to methodology, *Journal of materials research* 19(1) (2004) 3-20.

CHAPTER 3

Elaboration and Characterization of YSZ Coatings Prepared by Low-Pressure Plasma Spray

Chapter 3 Elaboration and Characterization of YSZ Coatings Prepared by Low-Pressure Plasma Spray

3.1 Introduction

Yttria-stabilized zirconia (YSZ) coating is the focus of intensive research due to its excellent properties, such as high strength and toughness, low thermal conductivity, good ionic conductivity, and excellent biocompatibility [1-5]. For example, It can be used as a thermal barrier coating (TBC) in gas turbine engines, which can protect the components from the surrounding high-temperature medium to substantially extend turbine lives and improve engine efficiency [2,6-8]. Furthermore, YSZ coating can be applied as a negative oxygen ion conductor for the dense electrolyte of the solid oxide fuel cell (SOFC), which can convert chemical energy directly to electricity with high conversion efficiency and very low pollution [9-11]. Generally, the YSZ coatings can be prepared by the APS and vapor phase deposition processes. The APS YSZ coatings are typically deposited from stacks of lamellae, which result from the impact of molten splats [12,13]. The characteristics of these splats make it challenging to obtain dense, super-thin, and defect-free YSZ coatings. In contrast, the vapor phase deposition processes (PVD or CVD) can deposit a high-quality coating product, but their high operating cost and low deposition rate strongly restrict the application ranges [14].

To overcome the shortcomings of both processes, an LPPS process has been established and developed in recent years. By operating at high power and very low pressure, LPPS technology can produce high-quality YSZ coatings over comparatively large areas with thicknesses (~ 1 to >100 μm) that are impractical using traditional thermal spray or vapor deposition processes. Moreover, depending on the

specific spraying parameter, the YSZ deposition may be in the form of very fine molten droplets, vapor phase deposition, or a mixture of droplet and vapor deposition [15]. This means that different types of YSZ microstructures can be obtained, from thin and dense coatings [16,17] to mixed mode deposits [18,19] and columnar-structured coatings [20,21].

However, as the heat and momentum transfer is weak under low pressure, the LPPS process usually uses a high-energy plasma torch of more than 100 kW to melt and evaporate the YSZ powders [22-24], such as the O3CP torch (Sulzer Metco). The high-power plasma torch undoubtedly leads to high operating costs. Therefore, many attempts have been made to employ a lower plasma power to produce highly dense or columnar structured YSZ coatings under low pressures [19,25,26]. However, it remains challenging to deposit YSZ coatings with full columnar structures using conventional low-power plasma systems, due to the low heating ability of the expanding plasma jet under low pressure.

Based on this, the present study aimed to deposit high-quality YSZ coatings economically by using an 80-kW-class LPPS system. To compensate for the low plasma power, a bi-cathode plasma torch with axial injection mode was designed to deliver the YSZ powders into the center of the plasma jet, as described in Section 2.1.1. Using this axial plasma torch under low pressure was expected to enhance the plasma-particle interaction to obtain high-quality YSZ coatings with improved microstructures. As a preliminary study, two spraying conditions with different working gases, plasma powers, and spraying distances were used. A comparison was then carried out to study the effect of different parameters on the structures, morphologies, and properties of coatings.

3.2 Experimental Procedures

3.2.1 Spraying Material

Commercially available 7–8 wt% YSZ powders (Metco 6700, Oerlikon Metco, Switzerland) with particle sizes of 1–30 μm ($d_{50} = 10 \mu\text{m}$) were used as feedstock. These spherical powders were loosely packed agglomerations of fine YSZ particles that were specially designed for the PS–PVD process. Their morphology and chemical composition are illustrated in Figure 3.1 and Table 3.1, respectively.

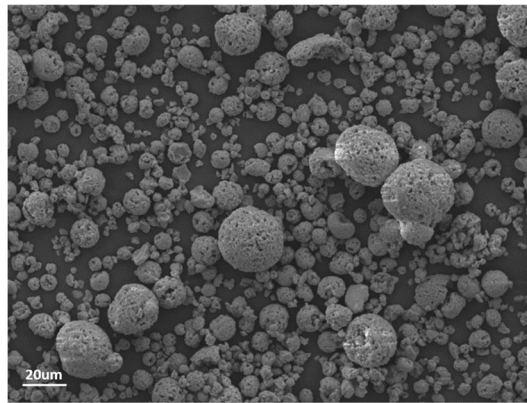


Figure 3.1 Morphology of Metco 6700 YSZ powder.

Table 3.1 Chemical composition of Metco 6700 YSZ powder.

Composition	ZrO ₂	Y ₂ O ₃	HfO ₂	Binder	Impurities
Wt.%	Balance	7.5	2.5 max	1	<0.1

3.2.2 Coating Preparation

The YSZ coatings were fabricated using the LPPS system in the LERMPS lab, as shown in Figure 3.2. The axial bi-cathode plasma torch was mounted on a movable 6-axis robotic arm (ABB, IRB 1400, Swiss). To support this new torch, a second power source, water-cooling, and control system were added to the original LPPS system. Carbon steel plates with dimensions of 30 mm \times 30 mm \times 5 mm were employed as substrates. To improve the adhesive strength between the substrate and the coating, bonding coatings of CoNiCrAlY (Amdry 9951, Sulzer Metco, USA) with

a thickness of 150–200 μm were deposited on the substrates using the APS technique (F4-MB, Sulzer Metco, USA).

Prior to coating deposition, the chamber pressure was lowered to around 6 mbar, and the substrates were preheated by the sweeping plasma jet. The average sample temperature during the preheating and spraying process was measured as 850 $^{\circ}\text{C}$ by a K-type thermocouple inserted in the back of the substrate. Besides, some substrates without the bonding coating were placed parallel to the plasma jet next to the normal sample. The detailed spraying parameters are summarized in Table 3.2.

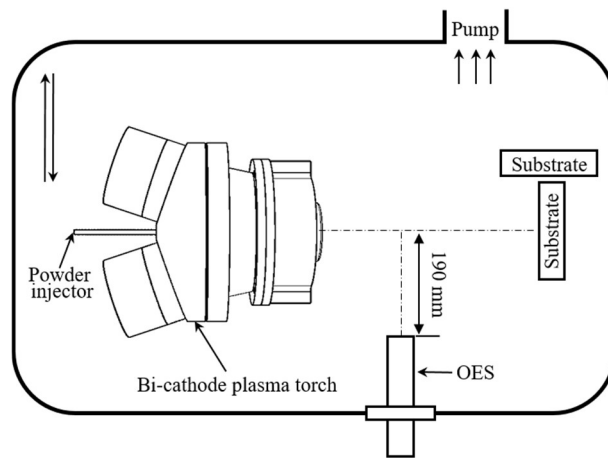


Figure 3.2 Schematic diagram of the YSZ coatings prepared by the LPPS system.

Table 3.2 LPPS operating parameters.

Parameters	Set 1	Set 2
Pressure (mbar)	6	6
Current (A)	1400	1400
Voltage (V)	56	58
Power (kW)	78	81
Net power (kW)	33	36
Plasma gas (Ar) (slpm) ^a	80	60
Plasma gas (He) (slpm) ^a	30	100
Plasma gas (H ₂) (slpm) ^a	12	10
Carrier gas (Ar) (slpm) ^a	3	3
Powder feeding rate (g/min)	2	2
Spraying distance (mm)	350,450,550	350,450,550
Torch speed (mm/s)	200	200

^a slpm: standard liter per minute.

3.2.3 Characterization

The OES instrument (Jobin-Yvon spectrometer, TRIAX190, UK) equipped with a CCD detector was used to examine the species in the plasma jet during the YSZ deposition process. The measurement was performed at a focal length of 190 mm and with a spraying distance of 200 mm from the nozzle exit. The spectral region was selected for peaks in the wavelength range of 400 nm to 900 nm. The surface morphology and cross-sectional microstructure of LPPS-deposited YSZ coatings were characterized by the field emission scanning electron microscope (JSM-7800F, JEOL, Japan). The phase compositions of the powder and as-sprayed coatings were identified by XRD (Rigaku, Japan) with Cu K α ($\lambda= 1.5418 \text{ \AA}$) radiation at a scan rate of 0.05°/s. The cross-sectional nanoindentation experiments were performed to determine the hardness and Young's modulus of the coatings [27]. A Berkovich-type nanoindenter (Hysitron, USA) was used with a maximum load of 10 mN. Ten random points were measured to calculate the mean value.

3.3 Results and Discussions

3.3.1 Plasma Jet Diagnostics

Figure 3.3 shows a photo of the plasma jets with YSZ powders using Set 1 and Set 2. It can be seen that the two plasma jets expanded and lengthened significantly under the same low pressure of 6 mbar, due to the low density of the surrounding chamber gas and laminar jet flow resulting in a weak energy dissipation [28]. The two plasma jets had a similarly expanding width of 100 mm. However, the Set 2 plasma jet had a longer length of 650 mm, with respect to 550 mm of the Set 1 plasma jet. The higher plasma power and larger gas flow of Set 2 played a crucial role in the longer plasma jet. Moreover, a large amount of He used in Set 2 could concentrate

not only the plasma jet but also the particle plume due to its high viscosity [29], which helped increase the vaporization degree of the YSZ powders [30].

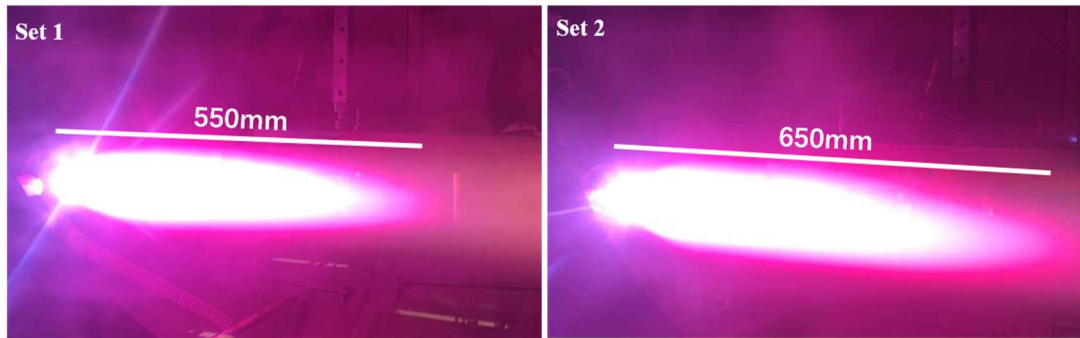


Figure 3.3 The plasma jets with YSZ powders using Set 1 (left) and Set 2 (right).

Figure 3.4 compares the OES spectra of the pure plasma jet using Set 1 and Set 2. The two spectra are similar because they used the same type of working gas. However, the H emission intensity using Set 1 was a slightly stronger than when using Set 2 at the position of 486.21 and 588.25 nm. This can be explained by the fact that Set 1 used more H₂ gas. Although the plasma power of Set 1 was slightly lower, it was enough to dissociate and ionize the H₂ gas as the required energy was the lowest among the working gases [31].

Figure 3.5 presents the OES patterns of the plasma jets with YSZ powders using Set 1 and Set 2. It is clear that both spectra had peaks from YSZ emissions between wavelengths of 500 and 600 nm. Besides, both original spectra of the pure plasma jet were not significantly affected by the injection of YSZ powders. These two phenomena demonstrated that during the LPPS process, the YSZ powders with a low feeding rate (2 g/min) could be vaporized by the axial bi-cathode plasma torch without consuming many plasma energy. However, it is also found that the YSZ signals for both spraying parameters had a comparatively weak intensity, indicating that the produced vapor quantity was limited for two cases. Although the YSZ powders were injected into the center of the plasma jet, the result was still reasonable as the new plasma torch had a limited net power and the plasma jet was not very long under 6 mbar. Fortunately, the YSZ signal of Set 2 was slightly stronger than that of Set 1, proving that higher power and larger amounts of He gas could indeed vaporize

more YSZ powders. A similar result was reported by Von Niessen et al. [22], who found that only conditions with a high intensity of YSZ spectral lines can fully vaporize the YSZ powders and obtain columnar coatings, whereas conditions with a low intensity of YSZ spectral lines can only vaporize a minor amount of YSZ powders and produce splat-like coatings.

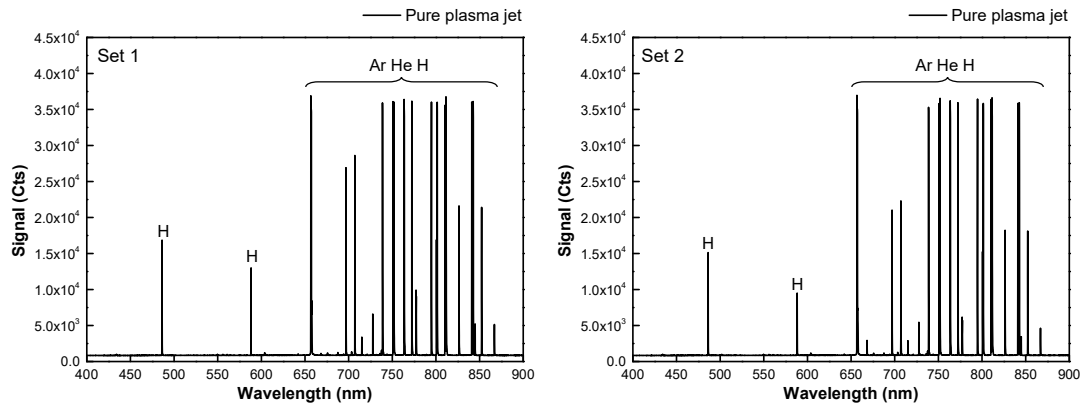


Figure 3.4 The OES patterns of pure plasma jets using Set 1 (left) and Set 2 (right).

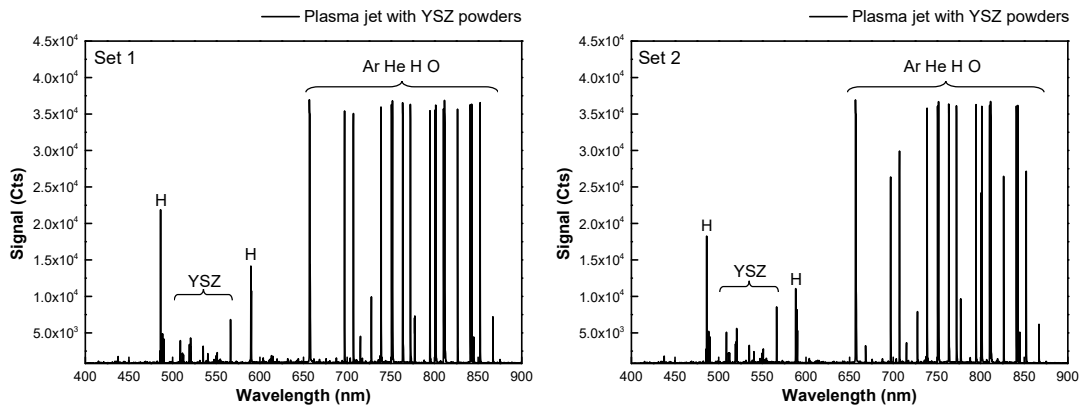


Figure 3.5 The OES patterns of plasma jets with YSZ powders using Set 1 (left) and Set 2 (right).

3.3.2 SEM Analysis

3.3.2.1 YSZ coatings with the Set 1 parameters

Figure 3.6 shows the surface morphologies of YSZ coatings deposited at different spraying distances using Set 1. It can be seen that all the YSZ coatings exhibited hybrid microstructures, which were composed of fine clusters and big unmelted powder. Almost no splats could be found in all the coatings, indicating that

the YSZ powders were not well melted using Set 1. Therefore, the fine clusters may come mostly from the unmelted small particles rather than from the vapor deposition.

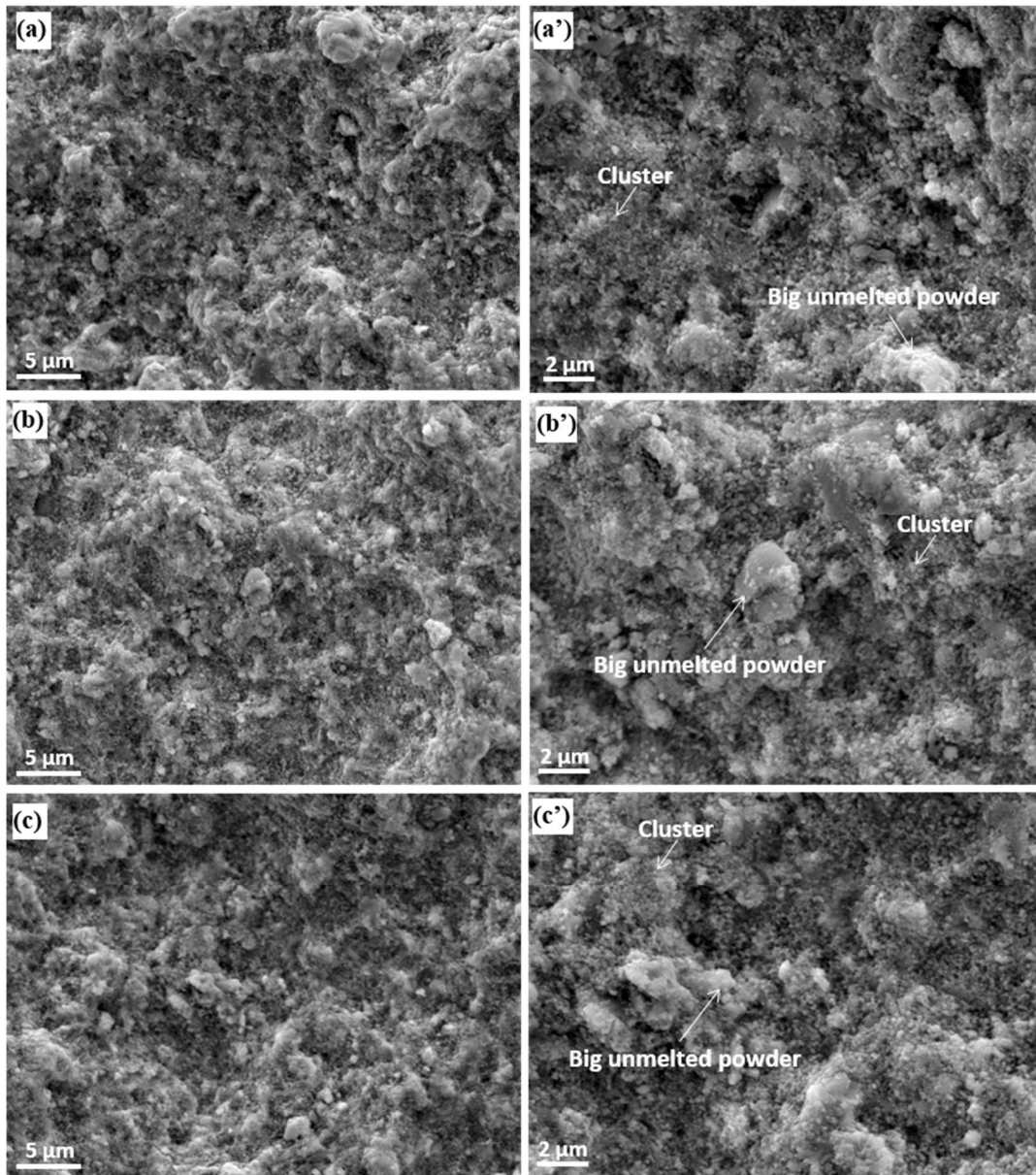


Figure 3.6 The surface morphologies of YSZ coatings deposited at different spraying distances of (a) 350 mm, (b) 450 mm, and (c) 550 mm using Set 1. Images (a')–(c') show the corresponding high magnification.

As the spraying distance increased, both the size and quantity of the unmelted big powders were reduced, indicating that the melting state of the YSZ powders had improved. Correspondingly, the proportion of coating clusters deposited from the vapor phase should be increased. The formation of these morphologies was mainly related to the different particle sizes and insufficient plasma power. When the

agglomerated YSZ powders were injected into the plasma jet, they probably fragmented into small primary particles with dimensions mostly in the sub-micrometer range. As the plasma power was not very high, however, the different-sized particles needed different amounts of time for fragmentation. For small agglomerated YSZ powders, these can be quickly decomposed into submicron particles by the plasma jet and get the chance to form the clusters after vaporization, but for the large agglomerated YSZ powders, it is hard for the plasma jet quickly fragment and melt them well. Therefore, they appear in the resulting coatings, especially for short spraying distances.

Figure 3.7 displays the cross-sectional morphologies of the YSZ coatings deposited at different spraying distances using Set 1. The hybrid microstructures stacked by the small clusters and big unmelted powders can be clearly seen in all the coatings. Although all the coatings have pores and cracks, the 350 mm and 550 mm coatings are denser than the 450 mm coating. This was because the 350 mm coating was deposited with the fastest impact speed, whereas the 550 mm coating was deposited with the best melting state. The deposition condition of the 450 mm coating was in the middle, so the bonding strength of the coating was the worst. Therefore, the 450 mm coating contains the most pores and cracks.

Furthermore, the YSZ coatings can also be found on the substrate parallel to the plasma jet using Set 1. Figure 3.8 shows their cross-sectional morphologies deposited at different spraying distances. All the coatings exhibited an approximate columnar structure, which should be the condensation of the vapor phase as the liquid or solid phase is hard to deposit on this side. The thickness of all coatings did not exceed 5 μm , which could be attributed to the insufficient power input resulting in a low quantity of the YSZ vapor phase in the plasma jet. This fact is consistent with previous OES and SEM results.

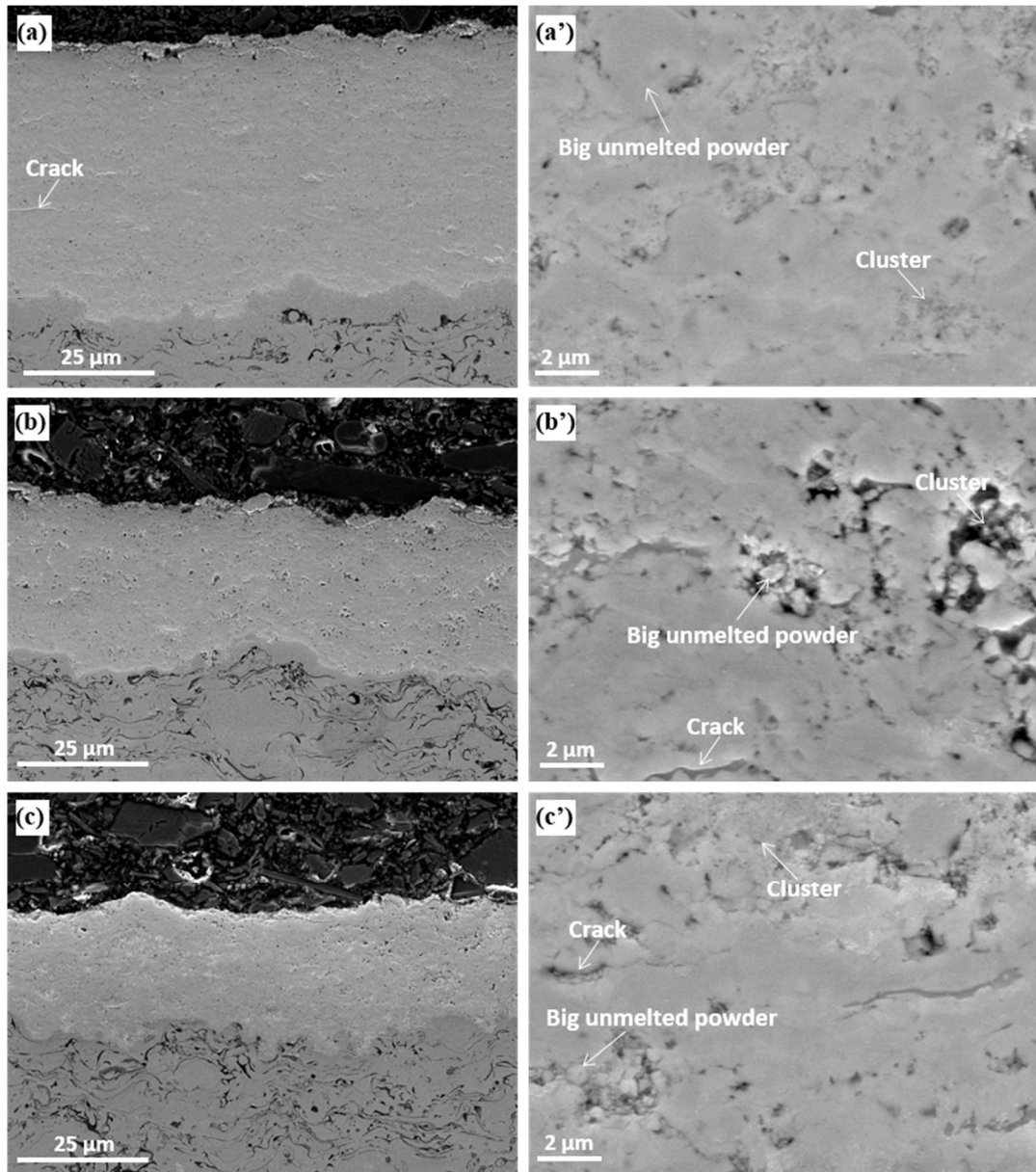


Figure 3.7 The cross-sectional morphologies of YSZ coatings deposited at different spraying distances of (a) 350 mm, (b) 450 mm, and (c) 550 mm using Set 1. Images (a')–(c') show the corresponding high magnification.

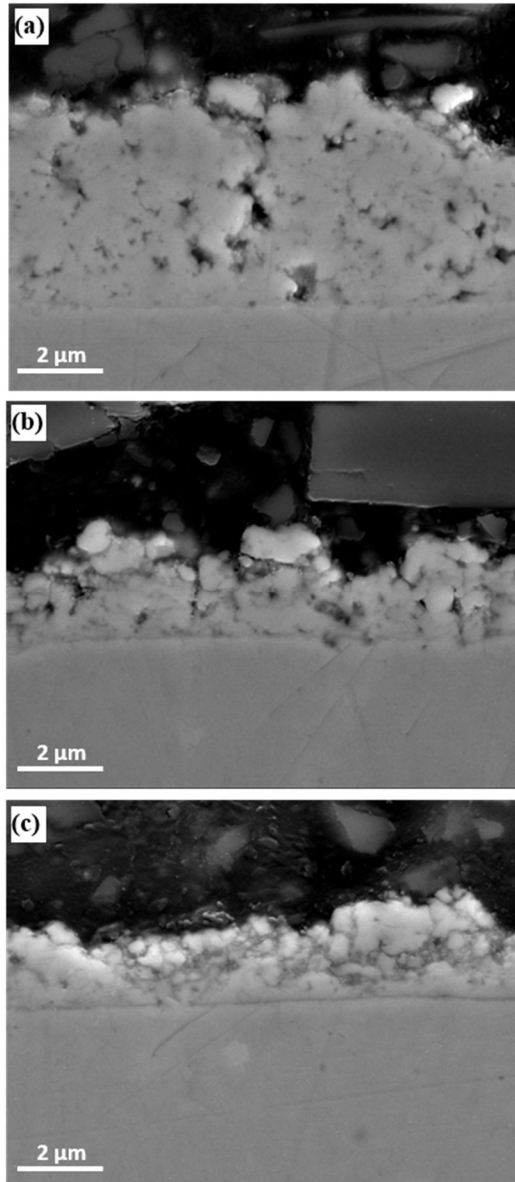


Figure 3.8 The cross-sectional morphologies of YSZ coatings deposited on the substrate parallel to the plasma jet at different spraying distances of (a), (a') 350 mm; (b), (b') 450 mm; and (c), (c') 550 mm using Set 1.

3.3.2.2 YSZ coatings with the Set 2 parameters

For comparison, Figure 3.9 presents the surface morphologies of the YSZ coatings deposited at different spraying distances using Set 2. Compared with the Set 1 YSZ coatings, the Set 2 YSZ coatings also had a hybrid microstructure. However, the Set 2 YSZ coating contained not only the small clusters and big unmelted powders but also many molten splats. This indicated that Set 2 was better for melting the YSZ

powders. Therefore, more vapor deposition was obtained to form the clusters using Set 2. In the 350 mm coating, many unmelted powders and large splats could be seen. When the spraying distance increased to 450mm, their sizes became significantly smaller and the number of clusters obviously increased. This change was more pronounced at 550mm, indicating that the melting state of the YSZ powders gradually improved with a longer spraying distance.

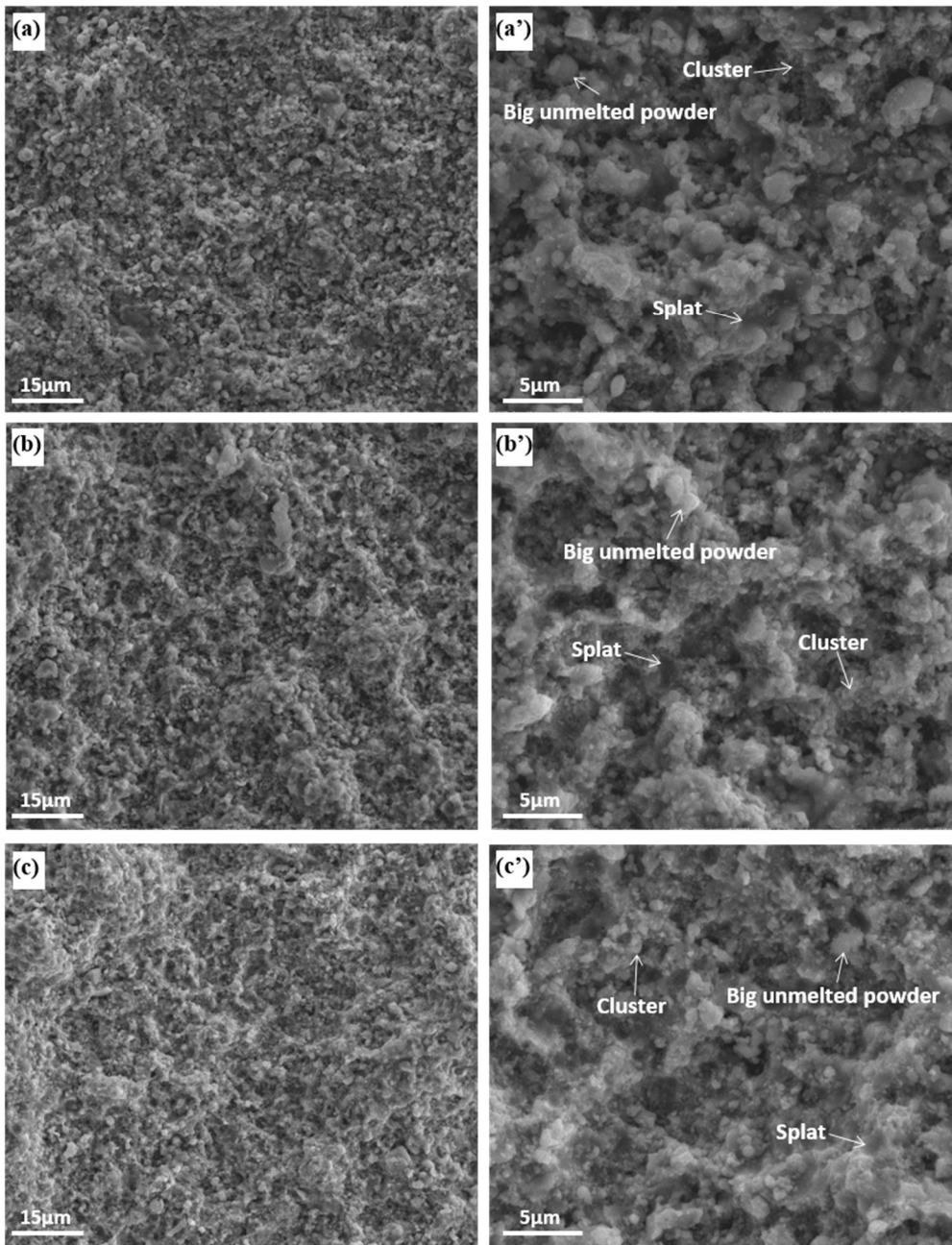


Figure 3.9 The surface morphologies of YSZ coatings deposited at different spraying distances of (a) 350 mm, (b) 450 mm, and (c) 550 mm using Set 2. Images (a')–(c') show the corresponding high magnification.

Figure 3.10 displays the cross-sectional morphologies of the YSZ coatings deposited at different spraying distances using Set 2. Compared with the Set 1 YSZ coatings, the Set 2 YSZ coatings had denser microstructures and fewer cracks, especially the 350 and 450 mm coatings. On the one hand, the YSZ powders could be heated better by using a higher plasma power, so the depositions are well combined. On the other hand, the use of a large He flow rate could make the YSZ powders have a higher impact velocity, which would help to form a denser structure.

Figure 3.11 shows the surface and cross-sectional morphologies of the YSZ coatings deposited on the substrate parallel to the plasma jet using Set 2. Similar to the Set 1 coatings, all the Set 2 YSZ coatings showed quasi-columnar structures deposited from the vapor phase. However, the columnar structures obtained by Set 2 were more visible and much thicker at each corresponding spraying distance, which proved that the amount of YSZ vapor phase was increased by Set 2. Moreover, it can be found on the surface morphologies that the cauliflower structure also became more evident at a longer spraying distance. This illustrates that the larger spraying distances favored the vaporization of YSZ powders.

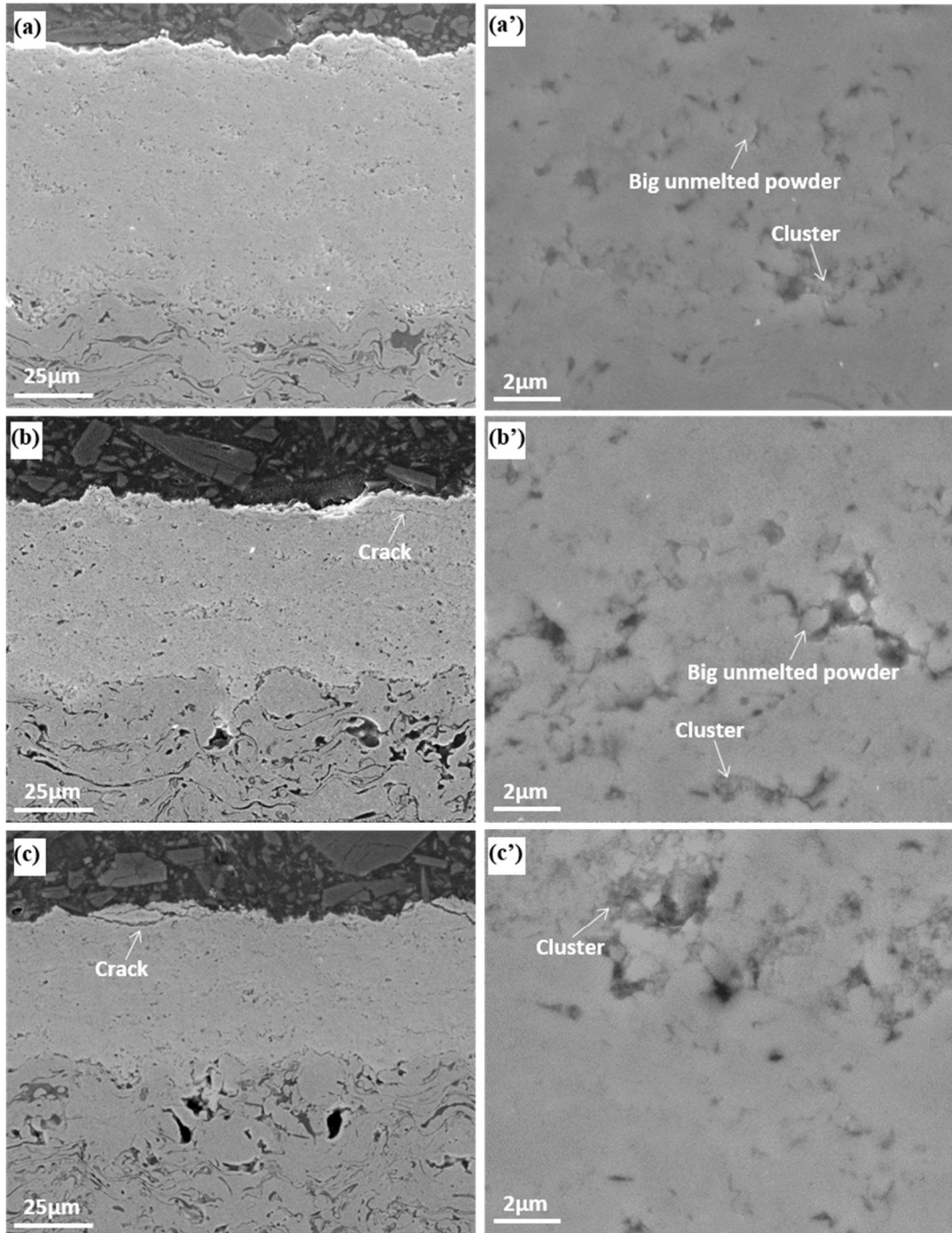


Figure 3.10 The cross-sectional morphologies of YSZ coatings deposited at different spraying distances of (a) 350 mm, (b) 450 mm, and (c) 550 mm using Set 2. Images (a')–(c') show the corresponding high magnification.

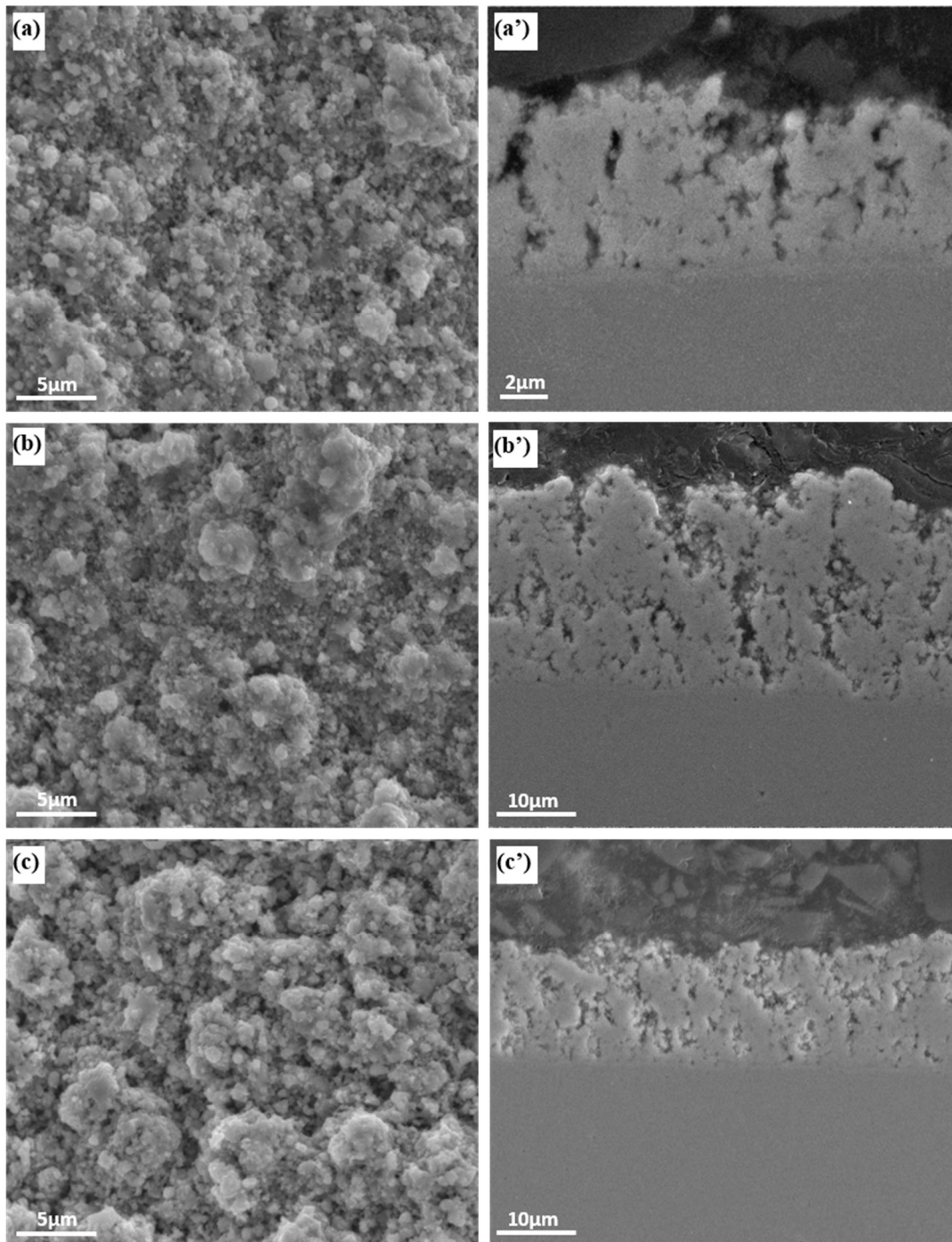


Figure 3.11 The surface and cross-sectional morphologies of YSZ coatings deposited on the substrate parallel to the plasma jet at different spraying distances of (a), (a') 350 mm; (b), (b') 450 mm; and (c), (c') 550 mm using Set 2.

3.3.3 XRD Analysis

Figure 3.12 shows the XRD patterns of the YSZ powders and as-sprayed coatings deposited using Set 1 and Set 2. As can be seen, the original YSZ powders were composed of the monoclinic zirconia phase (M-ZrO₂) and the cubic yttria phase (C-Y₂O₃), whereas the as-sprayed coatings contained a new tetragonal zirconia phase (T'-ZrO₂) as well as the original powder phases. This showed that the YSZ powders underwent a significant phase change after the LPPS process. Specifically, the M phase of the original YSZ powders was stable at low temperatures. When the YSZ powders were melted or vaporized by the plasma jet, the M phase had a martensitic transformation to a tetragonal phase around 1100 °C [32]. After the molten YSZ particles impacted on the substrates or the previously stacked splats, the tetragonal phase changed to a metastable T'-ZrO₂ due to the high quenching rates. The T' phase could be stored at room temperature because the doping of Y₂O₃ could generate oxygen deficiency and greatly maintain the stability of the T' phase.

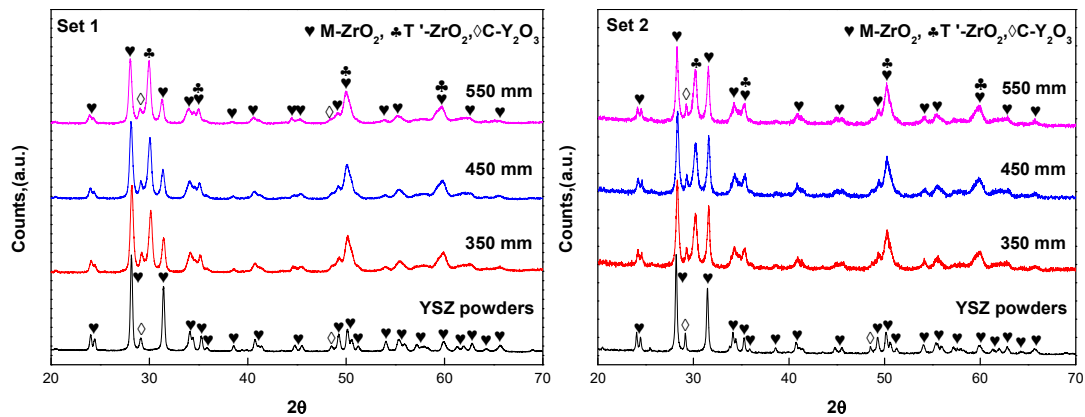


Figure 3.12 The XRD patterns of YSZ powder and as-sprayed coatings deposited using Set 1 (left) and Set 2 (right).

To further study the effect of different spraying parameters on the YSZ phase transformation, quantitative analyses based on the RIR method [33] were performed to calculate the percentages of the M and T' phase in the YSZ powders and the as-sprayed coatings using Set 1 and Set 2, as shown in Figure 3.13. The M phase content

of the YSZ powders was as high as 93%. After spraying using Set 1, more than 38% of the M phase turned into the T' phase. Also, the content of the T' phase increased with a longer spraying distance. Thus, the maximal content of 42% T' phase appeared in the 550 mm coating. This indicated that the plasma jet using Set 1 could maintain a high temperature within 550mm so that the YSZ powders could be heated well and continuously change from the M phase to the T' phase. Similarly, when the spraying parameter changed to Set 2, the content of the T' phase also increased with the spraying distance. For each corresponding spraying distance, however, using Set 2 achieved more transition from M phase to T' phase than using Set 1. Moreover, the advantage of using Set 2 was more evident at a longer spraying distance of 550 mm as the T' phase reached the highest content of 50%. Therefore, it could be concluded that the longer plasma jet achieved by using Set 2 favored the phase transformation from the low-temperature M phase to the middle-temperature T' phase, which meant that the YSZ powders were melted better when using Set 2.

The average crystallite sizes of the YSZ powders and the as-sprayed coatings deposited by Set 1 and Set 2 were also calculated using the Williamson-Hall equation [34-36], as shown in Figure 3.14. The mean crystallite size of the original YSZ powders was 43.9 nm, and all the as-sprayed coatings showed smaller values under 30 nm. This fact could be attributed to the rapid cooling during the deposition process, which restrained the growth of crystallite. As the spraying distance increased, the difference in crystallite size in each set was not significant. However, compared to the Set 1 YSZ coatings, it is evident that the Set 2 YSZ coatings exhibited smaller average crystallite sizes overall. What's more, the smallest average crystallite size of 20.6 nm appeared in the 550 mm coating using Set 2, indicating the YSZ powders had a better melting state in Set 2 and the best-melting state occurred at longer spraying distance. As a result, the condenser depression and cooling velocity for the YSZ powders were enhanced by using Set 2, which meant the resulting grains would be smaller.

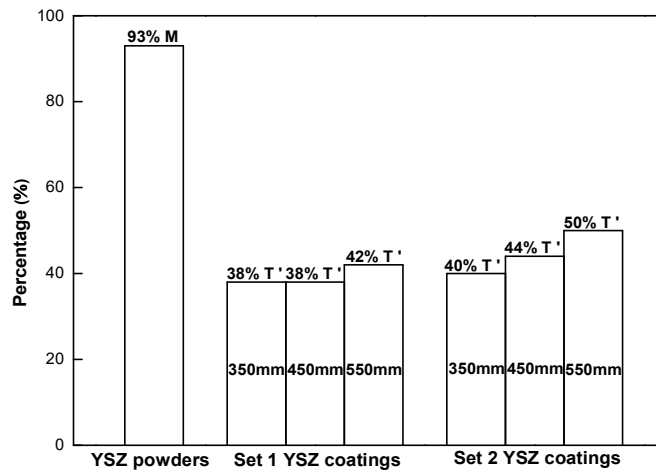


Figure 3.13 The percentages of the M and T' phase in the YSZ powders and the as-sprayed coatings deposited by Set 1 and Set 2.

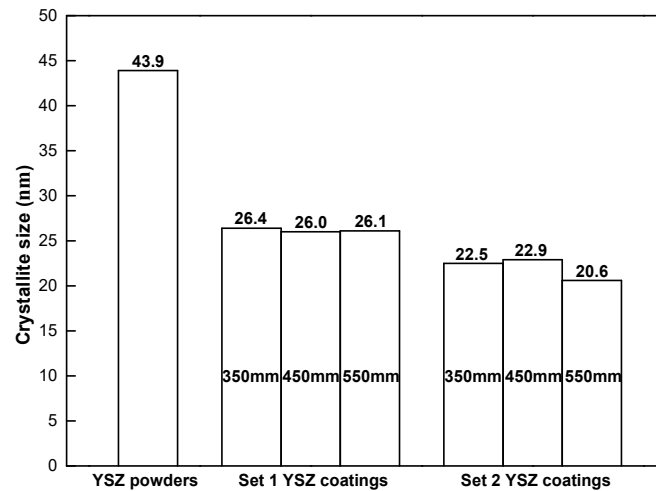


Figure 3.14 The crystallite sizes of the YSZ powders and the as-sprayed coatings deposited by Set 1 and Set 2.

3.3.4 Nanoindentation Results

Figure 3.15 shows the load-displacement curves of the cross-sectional YSZ coatings deposited by Set 1 and Set 2. All the nanoindentations applied a maximal load of 10 mN, a loading rate and unloading rate of 20 mN/min, and a dwell time of 10 s. The result showed that for both Set 1 and Set 2, the depth of indentation generally decreased as the spraying distance increased. The reason is that as the spraying distance increased, the YSZ powders were heated more fully. Thus, the proportion of nano-sized clusters and vapor deposition was gradually increased, resulting in more

nanopores and cracks in the coating. These fine defects reduced the bonding strength of the coating, then making it more easily penetrated by the indenter.

Figure 3.16 presents the hardness and Young's modulus of the cross-sectional YSZ coatings deposited by Set 1 and Set 2. Compared with all other investigated coatings, the 350 mm and 450 mm coatings using Set 2 exhibited the best overall mechanical properties, i.e., hardness and Young's modulus of 11.7 ± 0.6 GPa, 167.8 ± 4 GPa and 10.9 ± 1.1 GPa, 175.0 ± 10.4 GPa, respectively. This was due to the two coatings having the dense microstructures. As Set 2 used higher plasma power and a large flow rate of He, numerous molten YSZ splats were generated and struck the substrate with a higher velocity. The high-speed splats could combine the unmelted particles and clusters, thus decreasing the porosity and increasing the bonding strength inside the coating. In contrast, the 450 mm coating using Set 1 had the lowest hardness and Young's modulus (7.6 ± 0.8 GPa and 144.6 ± 11.4 GPa, respectively). As the melting state of the YSZ powders using Set 2 was worse than that in Set 1, there were many unmelted particles involved in this coating. Therefore, numerous pores and cracks with weak cohesion were obtained, which resulted in lower mechanical properties for the coating.

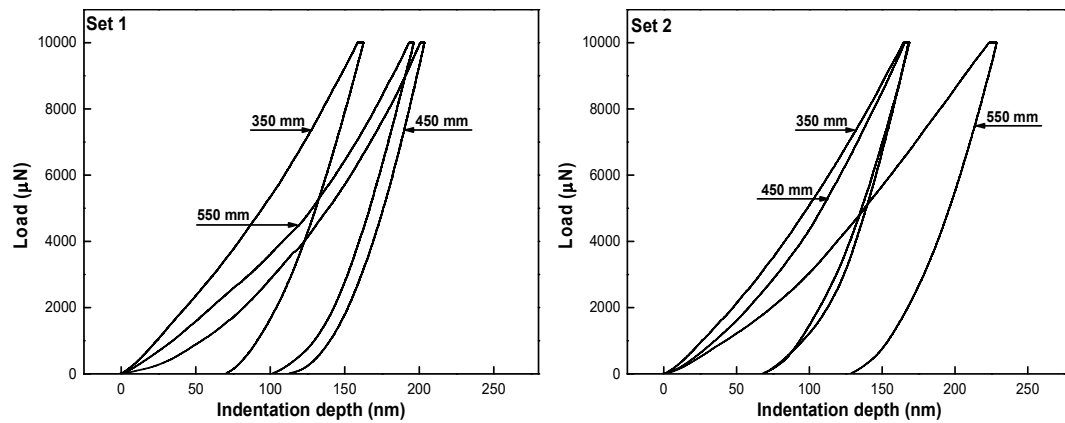


Figure 3.15 The load-displacement curves of the cross-sectional YSZ coatings deposited by Set 1 (left) and Set 2 (right).

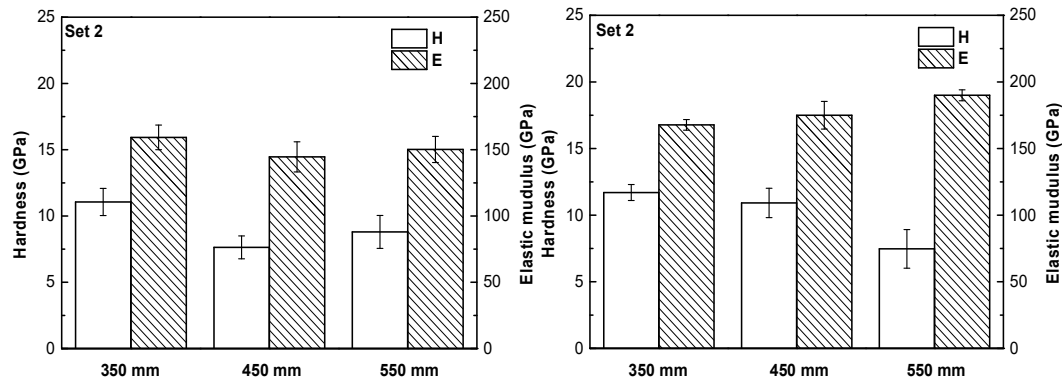


Figure 3.16 The hardness and Young's modulus of the cross-sectional YSZ coating deposited by Set 1 (left) and Set 2 (right).

3.4 Conclusions

In this study, YSZ coatings were deposited by an LPPS process with an axial bi-cathode plasma torch. The effects of spraying conditions on the plasma jet and coating deposition were investigated. The microstructures, phase compositions and mechanical properties of the coatings were examined. Based on the obtained results, the following conclusions can be drawn:

1) The designed axial bi-cathode plasma torch could obtain dense YSZ coatings with hybrid microstructures. The YSZ powders could be evaporated, but the quantity of the vapor phase was limited. Therefore, thin YSZ coatings with quasi-columnar structures deposited from the vapor phase could be found on the substrate parallel to the plasma jet.

2) Among the spraying parameters, the high plasma power, large He gas flow and long spraying distance played an essential role in the melting or the vaporization of the YSZ powders, as well as the phase transformation.

3) The best overall mechanical properties were found in the densest 350 mm and 450 mm coatings using Set 2, whose hardness and Young's modulus was 11.7 ± 0.6 GPa, 167.8 ± 4 GPa, and 10.9 ± 1.1 GPa, 175.0 ± 10.4 GPa, respectively.

References

- [1] B. Nait-Ali, K. Haberko, H. Vesteghem, J. Absi, D. Smith, Thermal conductivity of highly porous zirconia, *Journal of the European Ceramic society* 26(16) (2006) 3567-3574.
- [2] X.Q. Cao, R. Vassen, D. Stoeber, Ceramic materials for thermal barrier coatings, *Journal of the European Ceramic Society* 24(1) (2004) 1-10.
- [3] A. Selçuk, A. Atkinson, Strength and toughness of tape-cast yttria-stabilized zirconia, *Journal of the American Ceramic Society* 83(8) (2000) 2029-2035.
- [4] M. Sillassen, P. Eklund, N. Pryds, E. Johnson, U. Helmersson, J. Bøttiger, Low-temperature superionic conductivity in strained yttria-stabilized zirconia, *Advanced Functional Materials* 20(13) (2010) 2071-2076.
- [5] Y. Gu, K. Khor, D. Pan, P. Cheang, Activity of plasma sprayed yttria stabilized zirconia reinforced hydroxyapatite/Ti-6Al-4V composite coatings in simulated body fluid, *Biomaterials* 25(16) (2004) 3177-3185.
- [6] R. Vassen, X. Cao, F. Tietz, D. Basu, D. Stöver, Zirconates as new materials for thermal barrier coatings, *Journal of the American Ceramic Society* 83(8) (2000) 2023-2028.
- [7] D.R. Clarke, S.R. Phillpot, Thermal barrier coating materials, *Materials Today* 8(6) (2005) 22-29.
- [8] D. Zambrano, A. Barrios, L. Tobón, C. Serna, P. Gómez, J. Osorio, A. Toro, Thermal properties and phase stability of Yttria-Stabilized Zirconia (YSZ) coating deposited by Air Plasma Spray onto a Ni-base superalloy, *Ceramics International* 44(4) (2018) 3625-3635.
- [9] J.W. Fergus, Electrolytes for solid oxide fuel cells, *Journal of Power Sources* 162(1) (2006) 30-40.
- [10] R. Hui, Z. Wang, O. Kesler, L. Rose, J. Jankovic, S. Yick, R. Maric, D. Ghosh, Thermal plasma spraying for SOFCs: Applications, potential advantages, and challenges, *Journal of Power Sources* 170(2) (2007) 308-323.
- [11] R. Vaßen, D. Hathiramani, J. Mertens, V. Haanappel, I. Vinke, Manufacturing of high performance solid oxide fuel cells (SOFCs) with atmospheric plasma spraying (APS), *Surface and Coatings Technology* 202(3) (2007) 499-508.
- [12] C. Tendero, C. Tixier, P. Tristant, J. Desmaison, P. Leprince, Atmospheric pressure plasmas: A review, *Spectrochimica Acta Part B: Atomic Spectroscopy* 61(1) (2006) 2-30.

- [13] X. Chen, S. Kuroda, T. Ohnuki, H. Araki, M. Watanabe, Y. Sakka, Effects of processing parameters on the deposition of yttria partially stabilized zirconia coating during suspension plasma spray, *Journal of the American Ceramic Society* 99(11) (2016) 3546-3555.
- [14] L. Zhu, N. Zhang, R. Bolot, M.-P. Planche, H. Liao, C. Coddet, Very low pressure plasma sprayed yttria-stabilized zirconia coating using a low-energy plasma gun, *Applied Physics A* 105(4) (2011) 991-996.
- [15] A. Vardelle, C. Moreau, J. Akedo, H. Ashrafizadeh, C.C. Berndt, J.O. Berghaus, M. Boulos, J. Brogan, A.C. Bourtsalas, A. Dolatabadi, M. Dorfman, T.J. Eden, P. Fauchais, G. Fisher, F. Gaertner, M. Gindrat, R. Henne, M. Hyland, E. Irissou, E.H. Jordan, K.A. Khor, A. Killinger, Y.C. Lau, C.J. Li, L. Li, J. Longtin, N. Markocsan, P.J. Masset, J. Matejcek, G. Mauer, A. McDonald, J. Mostaghimi, S. Sampath, G. Schiller, K. Shinoda, M.F. Smith, A.A. Syed, N.J. Themelis, F.L. Toma, J.P. Trelles, R. Vassen, P. Vuoristo, The 2016 Thermal Spray Roadmap, *Journal of Thermal Spray Technology* 25(8) (2016) 1376-1440.
- [16] F. Shao, H. Zhao, C. Liu, X. Zhong, Y. Zhuang, J. Ni, S. Tao, Dense yttria-stabilized zirconia coatings fabricated by plasma spray-physical vapor deposition, *Ceramics International* 43(2) (2017) 2305-2313.
- [17] G. Mauer, R. Vaßen, D. Stöver, Thin and Dense Ceramic Coatings by Plasma Spraying at Very Low Pressure, *Journal of Thermal Spray Technology* 19(1) (2010) 495-501.
- [18] P.-j. He, S. Yin, C. Song, F. Lapostolle, H.-l. Liao, Characterization of Yttria-Stabilized Zirconia Coatings Deposited by Low-Pressure Plasma Spraying, *Journal of Thermal Spray Technology* 25(3) (2016) 558-566.
- [19] Q.-Y. Chen, C.-X. Li, J.-Z. Zhao, G.-J. Yang, C.-J. Li, Microstructure of YSZ coatings deposited by PS-PVD using 45 kW shrouded plasma torch, *Materials and Manufacturing Processes* 31(9) (2016) 1183-1191.
- [20] A. Hospach, G. Mauer, R. Vaßen, D. Stöver, Columnar-structured thermal barrier coatings (TBCs) by thin film low-pressure plasma spraying (LPPS-TF), *Journal of Thermal Spray Technology* 20(1-2) (2011) 116-120.
- [21] M. Gindrat, H.M. Höhle, K. von Niessen, P. Guittienne, D. Grange, C. Hollenstein, Plasma Spray-CVD: A New Thermal Spray Process to Produce Thin Films from Liquid or Gaseous Precursors, *Journal of Thermal Spray Technology* 20(4) (2011) 882-887.
- [22] K. von Niessen, M. Gindrat, Plasma Spray-PVD: A New Thermal Spray Process to Deposit Out of the Vapor Phase, *Journal of Thermal Spray Technology* 20(4) (2011) 736-743.

- [23] K. von Niessen, M. Gindrat, A. Refke, Vapor Phase Deposition Using Plasma Spray-PVD™, *Journal of Thermal Spray Technology* 19(1) (2010) 502-509.
- [24] L. Gao, H. Guo, L. Wei, C. Li, S. Gong, H. Xu, Microstructure and mechanical properties of yttria stabilized zirconia coatings prepared by plasma spray physical vapor deposition, *Ceramics International* 41(7) (2015) 8305-8311.
- [25] Y. Gao, D.M. Yang, C.Q. Sun, Z.Y. Chen, Deposition of YSZ Coatings in a Chamber at Pressures below 100 Pa Using Low-Power Plasma Spraying with an Internal Injection Powder Feeding, *Journal of Thermal Spray Technology* 22(7) (2013) 1253-1258.
- [26] L. Zhu, N.N. Zhang, F. Sun, R. Bolot, M.P. Planche, H.L. Liao, C. Coddet, Thin Yttria-Stabilized Zirconia Coatings Deposited by Low-Energy Plasma Spraying Under Very Low Pressure Condition, *Journal of Thermal Spray Technology* 20(5) (2011) 1118-1124.
- [27] W.C. Oliver, G.M. Pharr, An improved technique for determining hardness and elastic modulus using load and displacement sensing indentation experiments, *Journal of materials research* 7(06) (1992) 1564-1583.
- [28] M.F. Smith, A.C. Hall, J.D. Fleetwood, P. Meyer, Very Low Pressure Plasma Spray—A Review of an Emerging Technology in the Thermal Spray Community, *Coatings* 1(2) (2011) 117-132.
- [29] J. Aubreton, M. Elchinger, V. Rat, P. Fauchais, Two-temperature transport coefficients in argon–helium thermal plasmas, *Journal of Physics D: Applied Physics* 37(1) (2003) 34.
- [30] G. Mauer, A. Hospach, R. Vaßen, Process development and coating characteristics of plasma spray-PVD, *Surface and Coatings Technology* 220 (2013) 219-224.
- [31] M.I. Boulos, P. Fauchais, E. Pfender, *Thermal plasmas: fundamentals and applications*, Springer Science & Business Media 2013.
- [32] G. Witz, V. Shklover, W. Steurer, S. Bachegowda, H.P. Bossmann, Phase Evolution in Yttria-Stabilized Zirconia Thermal Barrier Coatings Studied by Rietveld Refinement of X-Ray Powder Diffraction Patterns, *Journal of the American Ceramic Society* 90(9) (2007) 2935-2940.
- [33] C.R. Hubbard, R.L. Snyder, RIR-measurement and use in quantitative XRD, *Powder Diffraction* 3(2) (1988) 74-77.
- [34] A.K. Zak, W.A. Majid, M.E. Abrishami, R. Yousefi, X-ray analysis of ZnO nanoparticles by Williamson–Hall and size–strain plot methods, *Solid State Sciences* 13(1) (2011) 251-256.

- [35] G. Williamson, W. Hall, X-ray line broadening from filed aluminium and wolfram, *Acta metallurgica* 1(1) (1953) 22-31.
- [36] V. Mote, Y. Purushotham, B. Dole, Williamson-Hall analysis in estimation of lattice strain in nanometer-sized ZnO particles, *Journal of Theoretical and Applied Physics* 6(1) (2012) 6.

CHAPTER 4

Elaboration and Characterization of YSZ Coatings Prepared by Low-Pressure Suspension Plasma Spray

Chapter 4 Elaboration and Characterization of YSZ Coatings Prepared by Low-Pressure Suspension Plasma Spray

4.1 Introduction

As mentioned in Section 3.1, the YSZ coatings have a wide range of applications in aerospace, energy, and medicine [1-5]. Therefore, it becomes increasingly important to seek a fast and reliable process for preparing the YSZ coatings with high quality. The conventional APS process is one such process, with high deposition efficiency and low operating costs in comparison with vapor deposition processes like physical vapor deposition and chemical vapor deposition (PVD and CVD) [6]. However, the YSZ coatings prepared by a conventional thermal spray process are generally built by stacking a large number of splats with dimensions ranging from about 60 to 200 μm in diameter and 1 to 3 μm in thickness [7,8]. Thus, the coating microstructure (lamellae size, non-melted particles embedded in the coating, voids, cracks, etc.) is on a micrometer scale, which is hard to meet in demanding applications such as higher temperatures of operation, wear and corrosion under extreme conditions, and a longer lifespan of parts and devices [9].

To produce YSZ coatings with higher performance, a potential method is to deposit nanostructured YSZ coatings using an SPS process. The emerging coating technology allows the direct feeding of sub-micron YSZ powders in suspension to form the coating [10]. Such coating has the advantage of a much finer scale microstructure feature compared to that of conventional APS coating, whose diameter and thickness are between 0.1–2 μm and 20–300 nm, respectively [11-14]. This fine microstructure makes many micro-pores exist in the YSZ coatings, which enhances the phonon scattering of heat transport and thereby effectively reduces the thermal conductivity of coatings (0.3–1.6W/m·K) [15]. Not only that, as described in Section

1.2.1.2, the columnar or vertical cracked YSZ coating can also be prepared by SPS under certain process conditions, which is similar to that prepared by EB-PVD [19-22]. The columnar structure allows the coating to exhibit an excellent thermal shock resistance. Curry et al. [16] reported that the thermal cycling life of SPS YSZ coating is up to 9903 cycles, which is five times longer than that of the conventionally sprayed coating.

Although SPS has the above advantages, several challenges and limitations of the process must be considered. For instance, SPS requires a short spraying distance (30–40 mm) for achieving $St > 1$ [17,18], which increases the difficulty of cooling the substrate and spraying parts with complex shapes [19]. Moreover, the plasma torch used by SPS usually has a radial injection mode and a low plasma power, which makes it difficult to inject the suspension into the plasma center and realize efficient heating and acceleration. Therefore, recent studies have focused on improving the SPS process by using a high-power plasma torch with an axial injection mode, such as the Mettech axial III [20-25], which can achieve a higher quality coating with a higher particle velocity and a longer spraying distance. Based on this point, this study aims to find another feasible solution to enhance the SPS process by combining it with the LPPS process, which is called the LP-SPS process. On the one hand, the low-pressure environment is beneficial for increasing the particle velocity and prolonging its heating time. On the other hand, compared with the traditional SPS process, the LP-SPS process can produce a more uniform coating that deposited from the splats or even from the vapor phase. The corresponding microstructures of the coating can be laminar or columnar. Therefore, parts with complex geometries can be sprayed, even in the areas that are not in the line of sight.

However, the suspension injection becomes more difficult in the low-pressure environment. Using the axial injection mode is necessary because the radially injected suspension will be rejected by the expanding plasma jet under low pressure. Unfortunately, at present no commercial axial plasma torch is available for the LPPS process. Therefore, in order to deposit YSZ coatings by LP-SPS, a homemade bi-cathode plasma torch (the LERMPS lab, UTBM, France) with axial injection mode

was designed, as described in Section 2.1.1. Two F4-type cathodes with one common anode were applied for this new torch, which enables the maximum input power to reach 81 kW. Moreover, both very fine YSZ suspension and micro-sized YSZ powders can be axially injected into the low-pressure plasma center using this torch.

In this chapter, an ethanol-based YSZ suspension was sprayed under low pressures by using the axial bi-cathode plasma torch. To optimize the LP-SPS process, different spraying parameters were studied. For the poor spraying parameters, the YSZ coatings were simply characterized, and the reason for their low quality was analyzed. For the good spraying parameters, further analysis of the OES, SEM, XRD, and nanoindentation was performed. Moreover, the influence of different spraying parameters on the coating microstructure and property were investigated.

4.2 Experimental Procedures

4.2.1 Spraying Material

Commercially available 3 mol% YSZ powder (Shanghai ST-Nano Science & Technology Co., Ltd., China) with an average particle size of 100 nm was used as the raw material. The particle morphology and chemical composition are illustrated in Figure 4.1 and Table 4.1, respectively. Due to the fine particle size of the YSZ powders, they agglomerate together under the Coulomb force and van der Waals force.

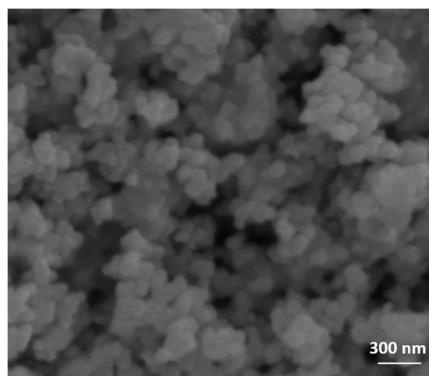


Figure 4.1 The morphology of the YSZ powders.

Table 4.1 The chemical composition of YSZ powders.

Composition	ZrO ₂	Y ₂ O ₃	Al ₂ O ₃	SiO ₂	Fe ₂ O ₃
Wt.%	94.60	5.0±0.3	≤0.02	≤0.01	≤0.03

4.2.2 Suspension Preparation

The simplest way to produce a suspension is to dissolve the submicron or nano solid particles in a solvent with suitable dispersant. The most frequently used solvents are ethanol and water [15,19]. Their main characteristics are presented in Table 4.2. Compared with water, ethanol has a lower surface tension and viscosity. As a result, the fragmentation time and resulting droplet size of the ethanol-based suspension will be shorter and smaller than the water-based suspension. Moreover, the vaporization energy of ethanol is much less than water, needing only 841 kJ/kg while water requires 2257 kJ/kg. In other words, the ethanol does not cool the plasma as much as water does, which means more energy can be used to heat the particles. Considering the above factors, ethanol was chosen for preparing the YSZ suspension in this study.

Table 4.2 The main characteristics of water and ethanol.

Liquid	Boiling temperature (°C)	Viscosity (mPa. s)	Surface tension (mN/m)	Vaporization energy (kJ/kg)
Ethanol	78	1.0	22.27	841
Water	99.98	1.74	71.97	2257

As the original YSZ powders had settled and stuck together, forming larger clusters or agglomerates, a dispersant Beycostat-C213 (CECA, France) [26] was added to stabilize the suspension. To ensure that the suspension had a slow sedimentation rate and low viscosity, a sedimentation test with different dispersant concentrations was studied in test tubes. Ultimately, 5 wt.% of dispersant (with respect to the YSZ mass) was selected for dispersing the YSZ particles in ethanol. After determining all the parameters, the YSZ particles, ethanol, and dispersant were

mixed using a combination of manual mixing, ultrasonic, and a magnetically driven stir bar. The stirring by the magnetic agitator continued until the end of the experiment.

4.2.3 Coating Preparation

Experiments were carried out on the LPPS equipment in the LERMPS lab, as illustrated in Figure 4.2. The axial bi-cathode plasma torch was mounted on a removable six-axis robotic arm (ABB, IRB 1400, Swiss). To support this torch, a second power source, a new water-cooling system, and a control system were added to the original LPPS system. Grit-blasted stainless steels were employed as substrate materials, which were preheated by sweeping the pure plasma jet before the deposition. The average sample temperature during the heating and spraying process was measured as 850°C by a K-type thermocouple inserted in the back of the substrate. Since the pneumatic pump cannot stop the suspension from flowing automatically into the plasma torch at low pressure, a peristaltic pump was used to deliver the YSZ suspension from the outside of the vacuum chamber. A specially designed injector with an internal diameter of 0.5 mm was carefully fixed along the axis of the anode nozzle, by which the suspension could be injected into the center of the plasma torch. During the injection, the suspension feed rate was controlled by adjusting the rotation speed of the peristaltic pump. To optimize the LP-SPS process, various spraying parameters were studied. The main adjusted parameters included the operating pressure, plasma power, gas composition and flow rate, and spraying distance, as demonstrated in Table 4.3.

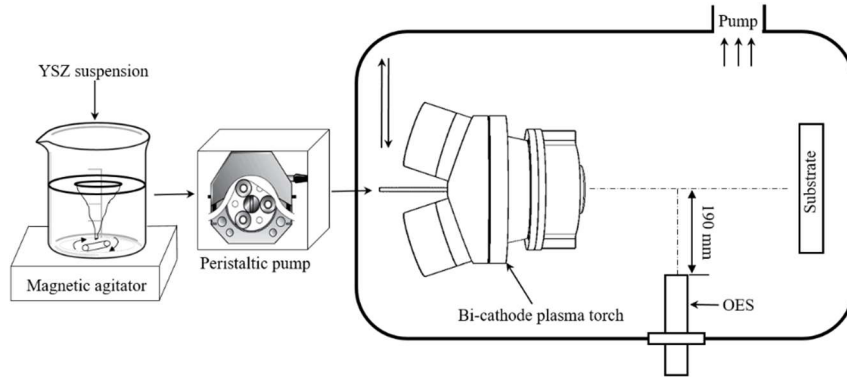


Figure 4.2 The experimental system of suspension plasma spraying YSZ at low pressure.

Table 4.3 The different spraying parameters for SPS YSZ coatings.

Parameters	Set 1	Set 2	Set 3	Set 4	Set 5
Pressure (mbar)	100	6	6	6	6
Current (A)	1000	1000	1400	1400	1400
Voltage (V)	61	61	46	56	58
Power (kW)	61	61	64	78	81
Net power (kW)	28	24	20	33	36
Plasma gas (Ar) (slpm) ^a	100	100	35	80	60
Plasma gas (He) (slpm) ^a	-	-	60	30	100
Plasma gas (H ₂) (slpm) ^a	16	16	10	12	10
Powder content (wt.%)	15	15	15	15	15
Feeding rate (ml/min)	15	15	15	15	15
Spraying distance (mm)	180-220	350-550	350-550	350-550	350-550
Torch speed (mm/s)	200	200	200	200	200
Result	✓	×	×	×	✓

^a slpm: standard liter per minute.

4.2.4 Characterization

For the LP-SPS YSZ coatings with good quality, the optical emission spectroscopy (OES) was employed to characterize the properties of the plasma jet under different operating conditions to detect the emission of evaporated particles inside the plasma jet. For measurements, a Jobin-Yvon spectrometer (type TRIAX190, UK) equipped with a charge-coupled device (CCD) detector was fixed at a focal length of 190 mm and with a spraying distance of 200 mm from the nozzle exit. All measurements were performed in the wavelength region ranging from 400

to 900 nm. In addition, the microstructures of coating surfaces and cross sections were characterized by the field emission scanning electron microscope (JSM-7800F, JEOL, Japan). In addition, the phase compositions of the powder and the coatings as sprayed were characterized by X-ray diffraction (Bruker AXS D8 Focus, Germany) with $\text{Co-K}\alpha$ ($\lambda=1.7889 \text{ \AA}$) radiation generated at 35 kV and 40 mA, respectively. Finally, the mechanical properties of the coating cross sections were studied by the nanoindentations (Hysitron, USA) with a diamond Berkovich tip at a maximum load of 10 mN. Ten separate indentations were made on the cross section of each investigated sample. A Poisson's ratio of 0.25 was used to calculate the Young's modulus [27].

4.3 Results and Discussion

Due to the different parameters used in the optimization of the spraying process, YSZ coatings of varying quality were obtained. Essentially, they can be divided into two categories. One is the YSZ coatings with poor quality, obtained using Sets 2–4, and the other is the YSZ coating with good quality obtained using Set 1 and Set 5. The following discusses these two types of YSZ coatings separately.

4.3.1 YSZ Coatings with the Set 2,3,4 Parameters

Figures 4.3 and 4.4 display the plasma jets with YSZ suspensions and corresponding YSZ coatings deposited at the spraying distance of 450 mm using Sets 2, 3, 4. As can be seen, the lengths of the plasma jets are Set 3 < Set 2 < Set 4, whose values are 450 mm, 500 mm, and 520mm, respectively. This is because Set 3 has the minimum net power and total gas flow, while the corresponding values of Set 2 and Set 4 increase sequentially.

Therefore, among these three YSZ coatings, the Set 3 coating was the worst melted. It is difficult to see the molten splats present in the coating, but can only find many unmelted sintered aggregates with particle sizes of more than 1 μm .

Additionally, the cross section of the Set 3 coating has the most pores, indicating the bonding strength inside the coating was the lowest, so the coating was partially detached during the sample preparation process. This is due to the poor melting of the YSZ powders and their insufficient impact velocity by using Set 3. In contrast, when Set 2 used higher net power, more splats instead of the large unmelted agglomerates can be found in the coating, demonstrating the melting state of the YSZ powders was improved. Even so, obvious cracks still exist in the Set 2 coating, indicating this improvement is limited. Although Set 2 has a higher total gas flow rate, it does not use He in the working gas, so the velocity of the YSZ powders is not sufficient when they impact the substrate. Compared with the two coatings above, the Set 4 coating exhibits the best quality. Most of the deposits in the Set 4 coating are molten splats. In addition, the coating has the fewest pores and cracks and bonds well to the substrate. This demonstrates that to obtain a high-quality YSZ coating at a relatively long spraying distance, it is necessary to make the YSZ powders have the best melting state and impact velocity. To achieve this goal, it is advantageous to use higher power and larger He gas flow.

In general, the quality of the Set 2–4 YSZ coatings is low, and most can easily peel off from the substrate. Therefore, further characterization tests were not performed on them but instead on the high-quality Set 1 and Set 5 coatings, which are described in the following section.



Figure 4.3 The plasma jets with YSZ suspensions at the spraying distance of 450 mm using Set 2,3,4.

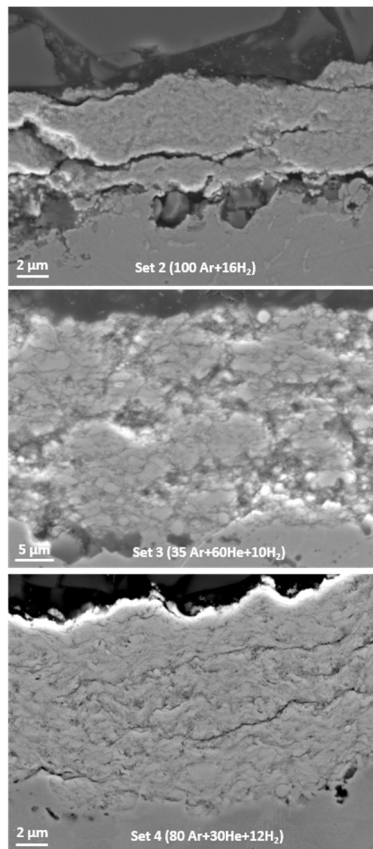


Figure 4.4 The YSZ coatings deposited at the spraying distance of 450 mm using Set 2,3,4.

4.3.2 YSZ Coatings with the Set 1 and Set 5 Parameters

4.3.2.1 Plasma jet diagnostics

Figure 4.5 compares the plasma jets of SPS YSZ coatings using the Set 1 and Set 5 parameters. As the chamber pressure decreases from Set 1 (100mbar) to Set 5 (6 mbar) and the plasma power increases from 61 to 81 kW, dramatic changes in the plasma jet can be observed. The width and length of the plasma jet extend from 40 mm and 250 mm to 100 mm and 550 mm, respectively. Although the expanding plasma jet under lower pressure reduces the heat and momentum transfer, it prolongs the heating time of the YSZ suspension in the plasma jet, which is more conducive to vaporizing the solvent and melting the particles over a wide spraying range.

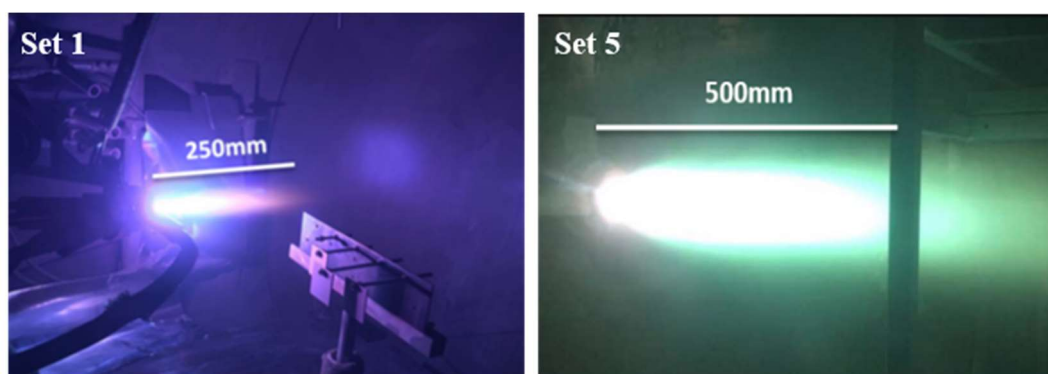


Figure 4.5 The plasma jets with YSZ suspensions using Set 1 and Set 5.

To further characterize the plasma jet and the vaporization of YSZ using Set 1 and Set 5, the OES patterns (see Figures 4.6 and 4.7) of the pure plasma jet and of the plasma jet with YSZ suspension were detected at the spraying distance of 200 mm. According to the atomic and molecular spectral database [28], all the detected patterns reveal that the spectral lines of Ar and H principally distribute in a wavelength range of 600–900 nm, while the signals of Zr and Y mainly locate at the wavelengths of 516.60, 550.21, 554.16 nm, etc.

Figure 4.6 illustrates the spectra of the pure plasma jet using the Set 1 and Set 5 parameters. It is clear that the Set 1 jet exhibits a much lower spectral intensity than the Set 5 jet, which indicates that the plasma temperature of Set 1 is considerably lower than that of Set 5. This is unsurprising because at first, the Set 5 jet applies a

higher input power. In addition, the dissipation of energy using Set 5 is much weaker than that of Set 1 because of the lower ambient pressure. Moreover, the use of He by Set 5 not only increases the plasma enthalpy and plasma temperature but also concentrates the plasma jet for maintaining the high temperature [29,30].

With the injection of the YSZ suspension, the spectral intensity of both the Set 1 and Set 5 cases decrease, as illustrated in Figure 4.7. This demonstrates that the injection of the YSZ suspension cools the plasma jet and decreases its temperature. Since the initial plasma temperature of Set 1 is low, this weakening effect becomes more pronounced, as can be seen in Figure 4.7 (a). Thus, there is only a small amount of energy that can be used to heat the YSZ powders using the Set 1 parameter. As a result, most of the YSZ powders can only be melted or semi-melted, leading to a low vaporization degree of YSZ powders. However, this situation is improved by using the Set 5 parameter, as revealed in Figure 4.7 (b). By using helium and a higher plasma power, the spectral intensity of the Ar and H is not drastically reduced after the injection of YSZ suspension. In fact, the spectral intensity of the plasma jet with YSZ suspension using Set 5 is even stronger than that of the pure plasma jet using Set 1. In other words, in using the Set 5 parameter, more plasma energy remains for heating the YSZ powders. Therefore, the spectral signal of Zr using Set 5 is much higher than in using Set 1, which indicates that the YSZ powders are better vaporized at the spraying distance of 200 mm.

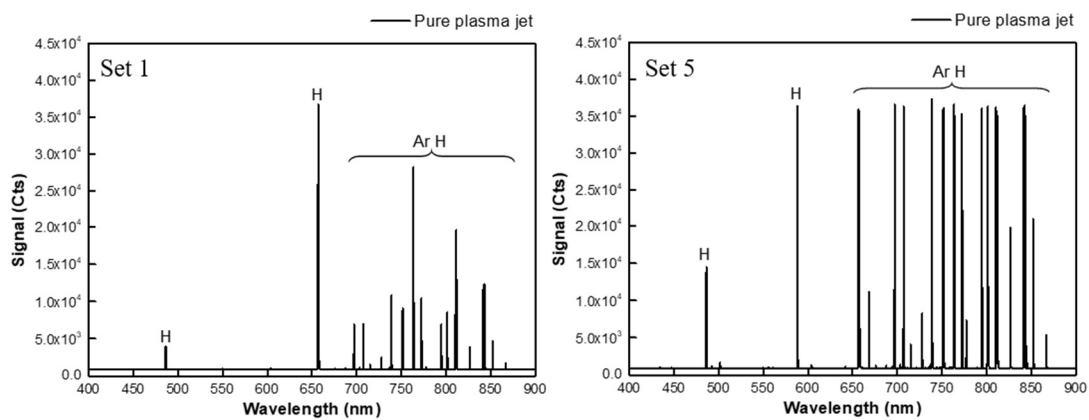


Figure 4.6 The OES patterns of pure plasma jets using Set 1 and Set 5.

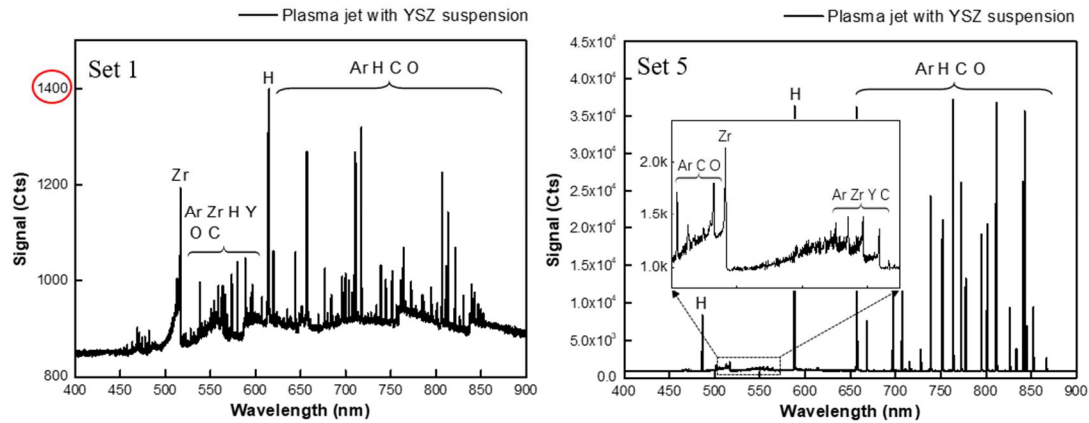


Figure 4.7 The OES patterns of plasma jets with YSZ suspension using Set 1 and Set 5.

4.3.2.2 SEM analysis

The surface morphologies of YSZ coatings deposited at different spraying distances using the Set 1 parameter are illustrated in Figure 4.8. It is found that all the YSZ coatings display mixed microstructures, which are composed of the unmelted aggregates (UA), unmelted sintered aggregates (US), melted sintered aggregates (MS), and vapor deposition (VD). Except for the UA and VD, the maximal sizes of US and MS for all the YSZ coatings are about 1 and 2 μm , respectively, which are much larger than that of the original feedstock (100 nm).

These particular morphologies can be explained by the deposition mechanism of the LP-SPS process [10,15]. After the YSZ suspension is injected into the center of the plasma jet, it is first fragmented into liquid drops, followed by the ethanol vaporization. After that, the fine YSZ powders are intensively reunited and then form the agglomerates with different sizes. Then the plasma jet heats these different agglomerates and makes them exhibit four different deposition states when striking the substrate. The lowest heating state is UA, where no sintering or melting happen for the agglomerates, making UA maintain their original size in the coating. The next heating state is US, where the agglomerates are merely sintered, and a lack of subsequent melting results in a large spherical body of US in the coating. If the agglomerates have an opportunity to be further heated, they can transform to MS, deposited as a melted lamella. Finally, with a perfect heating condition, the agglomerates can even be vaporized as VD and condensate on the substrate.

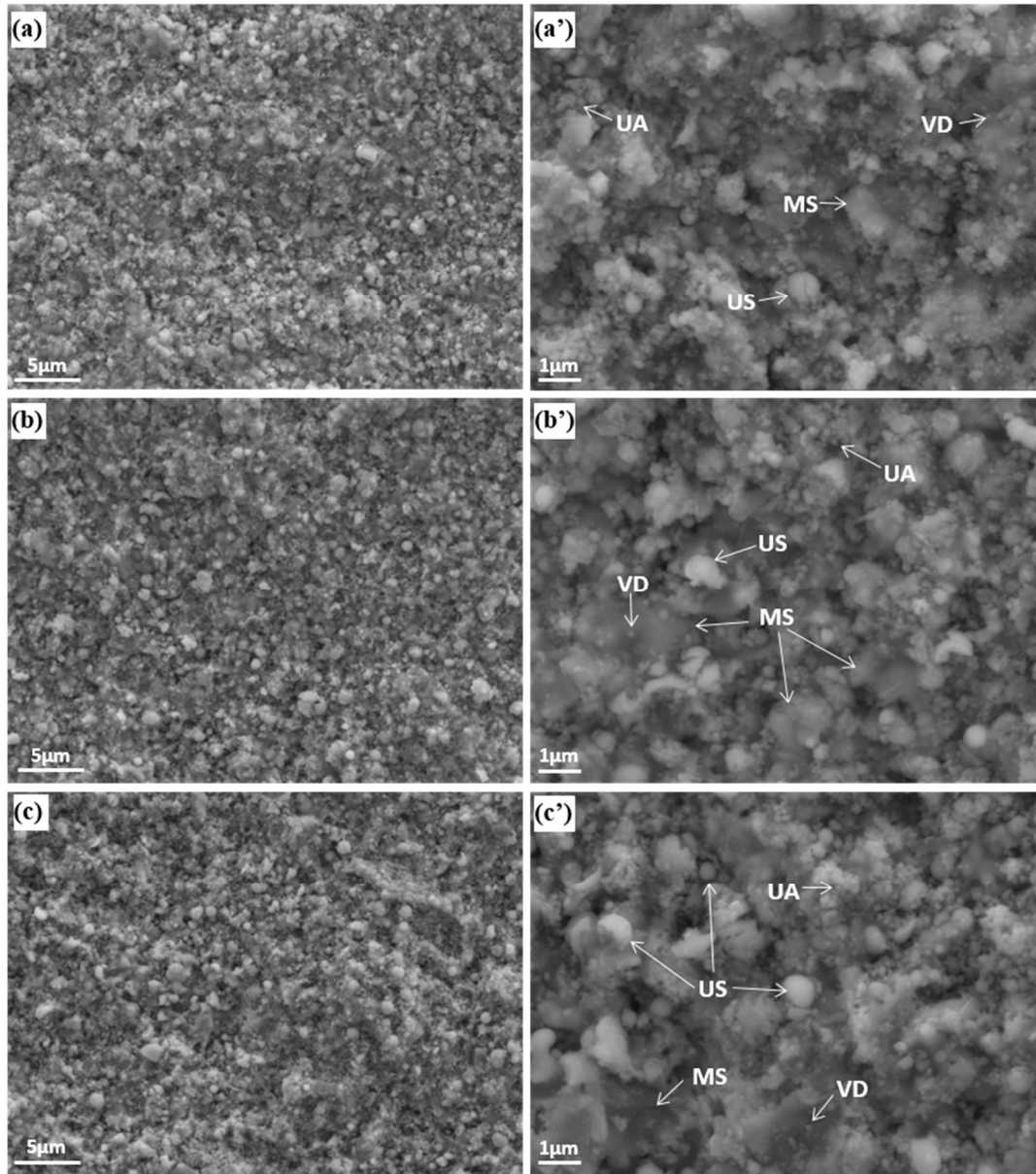


Figure 4.8 The surface morphologies of YSZ coatings deposited at different spraying distances of (a) 180, (b) 200, and (c) 220 mm using Set 1. Images (a')–(c') show the corresponding high magnification.

Since the SPS process using Set 1 has a low plasma power and a short plasma jet, it is difficult for all the agglomerates to be well melted as MS or VD, especially under the long spraying distance. Indeed, the four deposition states can be observed in all the Set 1 YSZ coatings, as illustrated in Figure 4.8. Among them, the 180mm YSZ coating has the highest number of VD, while the 200 and 220 mm YSZ coatings have the highest number of MS and US, respectively. This is because the plasma jet at 180 mm still has a high plasma temperature for vaporizing the YSZ powders.

However, as the spraying distance increases, the plasma temperature rapidly decreases. Thus, the melting state of YSZ powders worsens until the sintering occurs. Such low melting states will give rise to weak interparticle bonding and result in more pores or cracks in the YSZ coatings.

Figure 4.9 presents the cross-sectional morphologies of YSZ coatings deposited at different spraying distances using the Set 1 parameter. The mixed microstructures can be seen in all the coatings, with the nano-sized UA and VD embedded within the submicron-sized US and MS. As a result, the YSZ coatings exhibit a thin and uniform microstructure with a small number of pores in a diameter of smaller than 1.5 μm , and the thickness of the coatings is in the range of 20–30 μm . With longer spraying distance, increasing amounts of US and MS can be observed in the YSZ coating due to the partial heating of YSZ powders. Moreover, after a more extended period of heating, the sizes of the deposition UA, US, MS, VD tend to be larger. The partially molten deposits with increasing sizes cannot entirely flatten when striking the substrate, so the bonding strength between them is deficient. Therefore, more pores and even inter-lamellar cracks are generated in the YSZ coating at 200 mm. This microstructure can significantly lengthen the path of heat conduction through the phonons, which will reduce the thermal conductivity of YSZ as a thermal barrier coating [31,32].

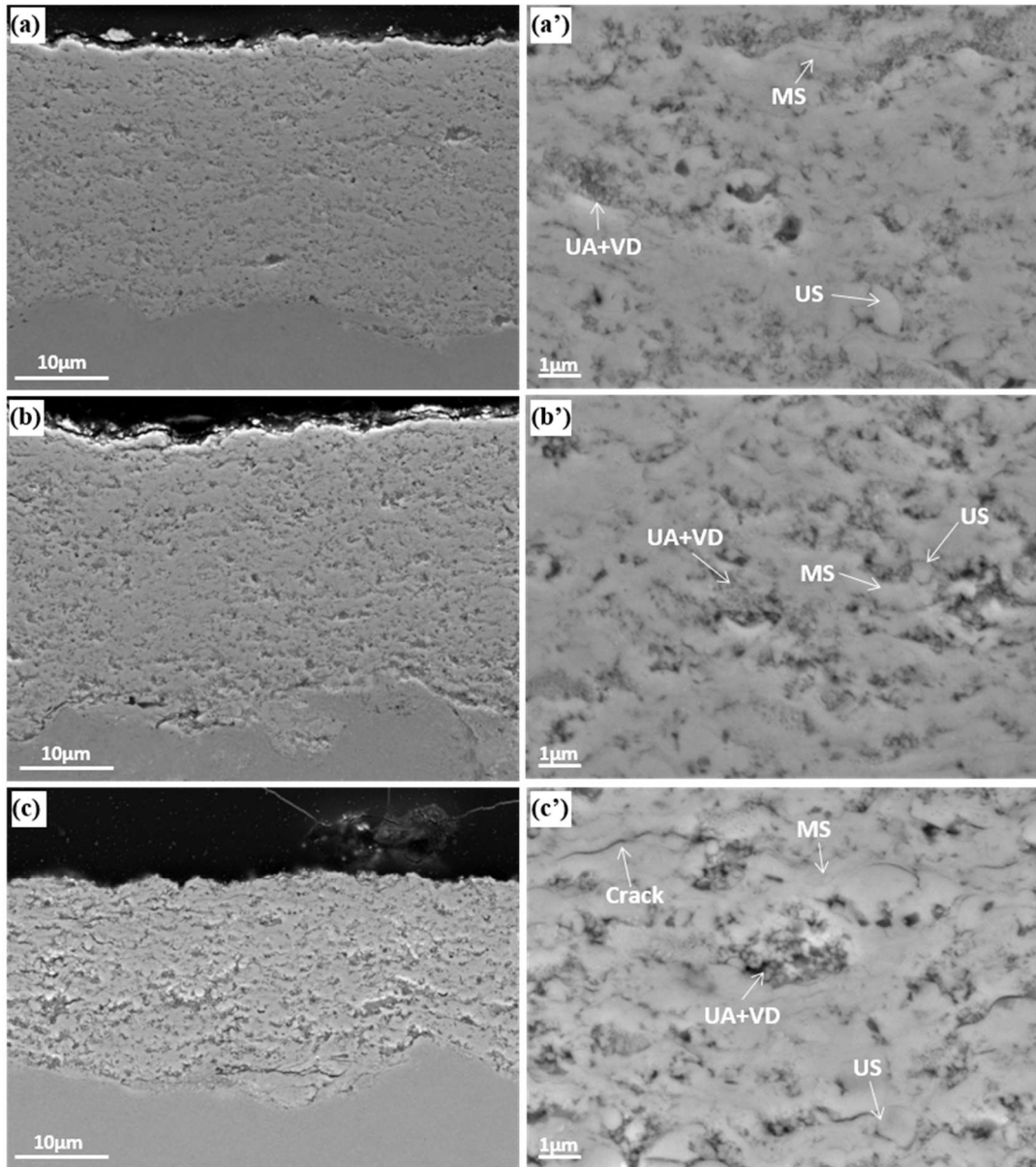


Figure 4.9 The cross-sectional morphologies of YSZ coatings deposited at different spraying distances of (a) 180, (b) 200, and (c) 220 mm using Set 1. Images (a')–(c') show the corresponding high magnification.

As a contrast, Figure 4.10 presents the surface morphologies of YSZ coatings deposited at different spraying distances using the Set 5 parameter. Unlike the mixed microstructures of the Set 1 YSZ coatings (see Figure 4.8), the Set 5 YSZ coatings deposited present a mostly granular nanostructure or at least a sub-micro one. There are almost no YSZ deposits with a size exceeding 1 μm. This benefits from the use of higher plasma power and a larger helium flow in Set 5, which is able to heat the YSZ suspension for a longer time and efficiently reduce the deposit size.

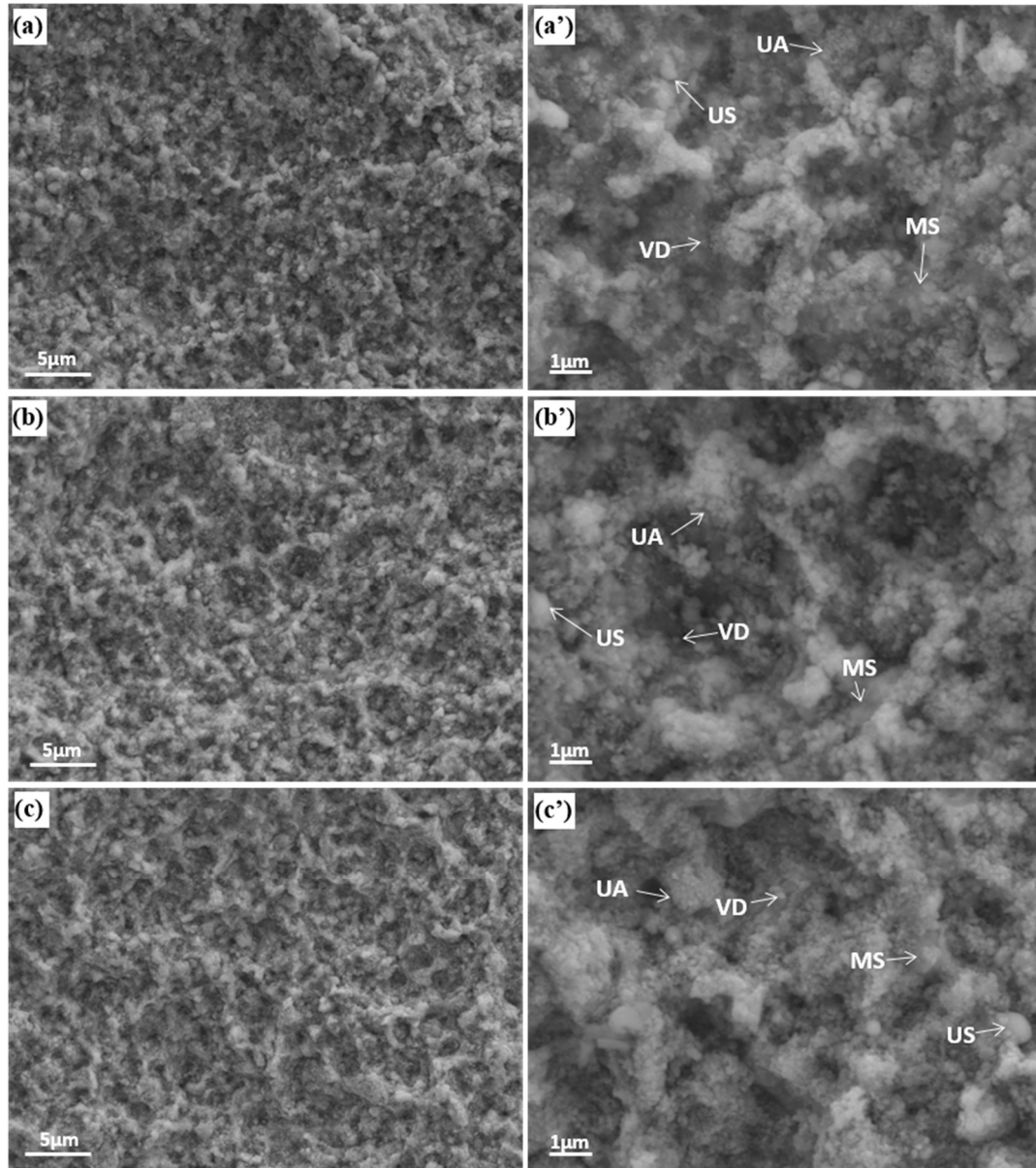


Figure 4.10 The surface morphologies of YSZ coatings deposited at different spraying distances of (a) 350, (b) 450, and (c) 550 mm using Set 5. Images (a')–(c') show the corresponding high magnification.

In addition, as the spraying distance increases, this phenomenon of size reduction becomes more pronounced. For example, the US and MS with large size are difficult to find in the 550 mm coatings. Moreover, more YSZ powders are possible to be vaporized at a longer spraying distance and deposited on the substrate as the VD. In general, compared with the Set 1 YSZ coatings, the Set 5 YSZ coatings possess more nano-sized particles because of the more extended plasma jet. The

stacking of these nano-sized particles forms nano-sized pores, which can further enhance the thermal barrier property of the YSZ coatings.

The cross-sectional morphologies of YSZ coatings deposited at different spraying distances using the Set 5 parameter are presented in Figure 4.11. Clearly, all the YSZ coatings are composed of the smaller-sized deposits UA, US, MS, and VD due to the longer spraying distance. Therefore, the proportion of the nanoparticles formed by the vapor phases is increased, which is consistent with the result measured by OES (see Figure 4.7 (b)). After that, these fine YSZ deposits are packed on the substrate, so a more porous microstructure containing fine pores and cracks is obtained. The thickness of the Set 5 coatings is in the range of 20–25 μm , similar to that of the Set 1 coatings. However, the average deposition rate of Set 5 is lower than that of Set 1, at about 0.9 $\mu\text{m}/\text{min}$ and 1.6 $\mu\text{m}/\text{min}$, respectively. With a longer spraying distance, the fine pores and cracks in the YSZ coatings gradually decrease due to the YSZ powders being better melted with the longer heating time. Thus, the denser YSZ coating with few cracks can be found at 550 mm, as shown in Figure 4.11 (c). The thin and dense Set 5 YSZ coatings are suitable for use as the electrolytes of SOFC since the structure can not only efficiently conduct the ions but also form a gas-tight seal between the gases from both the anode and cathode [33-35].

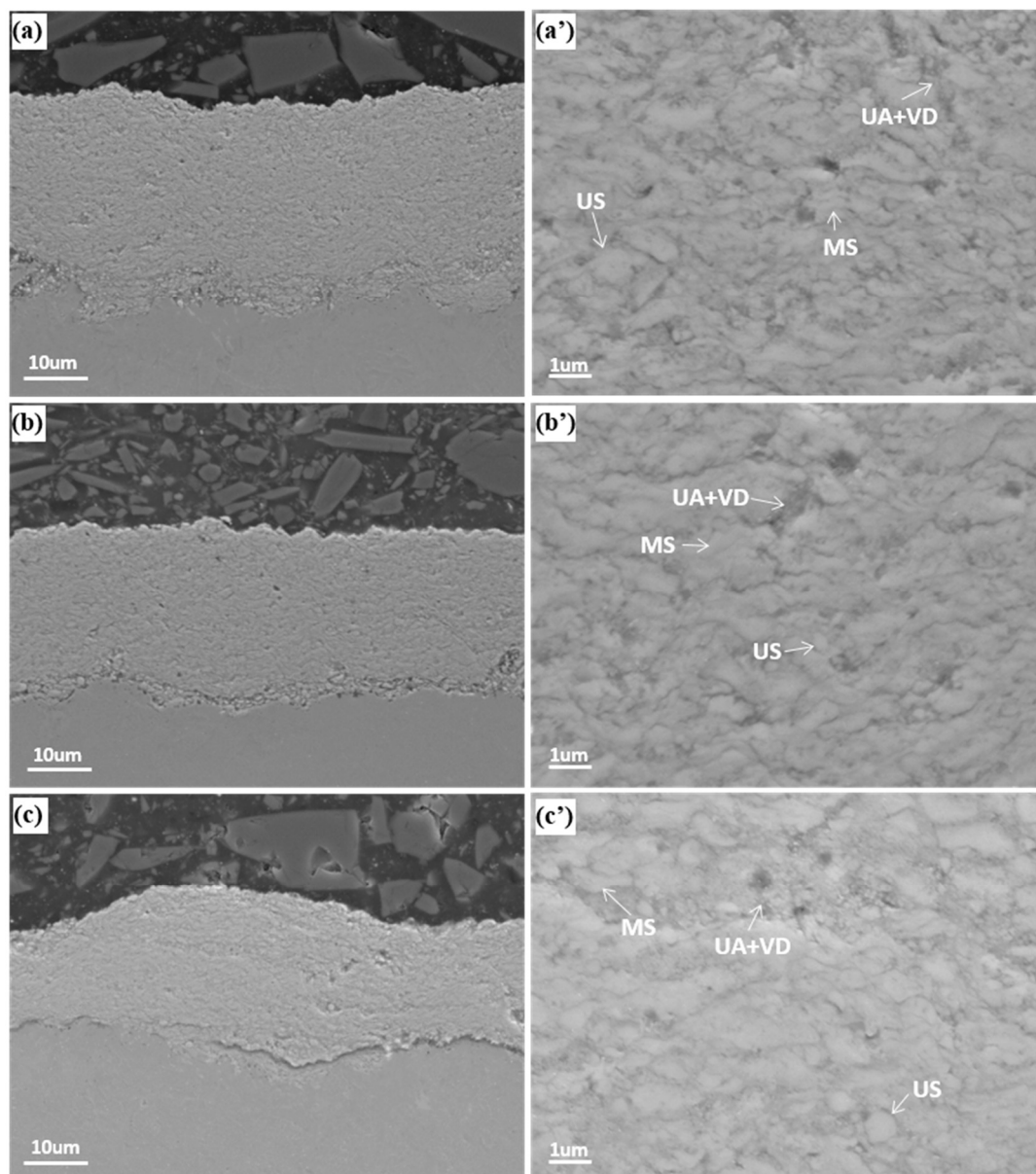


Figure 4.11 The cross-sectional morphologies of YSZ coatings deposited at different spraying distances of (a) 350, (b) 450, and (c) 550 mm using Set 5. Images (a')–(c') show the corresponding high magnification.

In addition to the substrate surface, it is worth noting that there are also YSZ coatings on the side and back of the substrate at each spraying distance using the Set 5 parameter. However, as illustrated in Figure 4.12, only the cross-sectional morphologies of the 450 mm coating are characterized because the others are easily peeled off and broken. As can be seen, the two YSZ coatings exhibit porous structures deposited from the vapor phase. The thickness of the coating on the side and back of the substrate is 20 and 60 μm, respectively, indicating that using Set 5 can achieve a

large amount of YSZ vapor. Surprisingly, the YSZ coating from the back of the substrate is even thicker than from the front. This may be because when the YSZ vapor impacts the substrate, it has a low velocity due to the Knudsen effect. The Stokes' number of vapor is less than 1, leading it to move with the plasma jet along the surface of the substrate. Thus, only the YSZ particles with a larger size can achieve sufficient velocity and deposit on the surface of the substrate. However, when the YSZ vapor passes with the plasma jet through the side and back of the substrate, its velocity has been dramatically reduced due to the obstruction of the substrate, especially arriving the back of substrate. Therefore, the YSZ vapor has more opportunities to deposit on the back. The result of EDS further proves that the porous coatings deposited on the back of the substrate are indeed YSZ coatings.

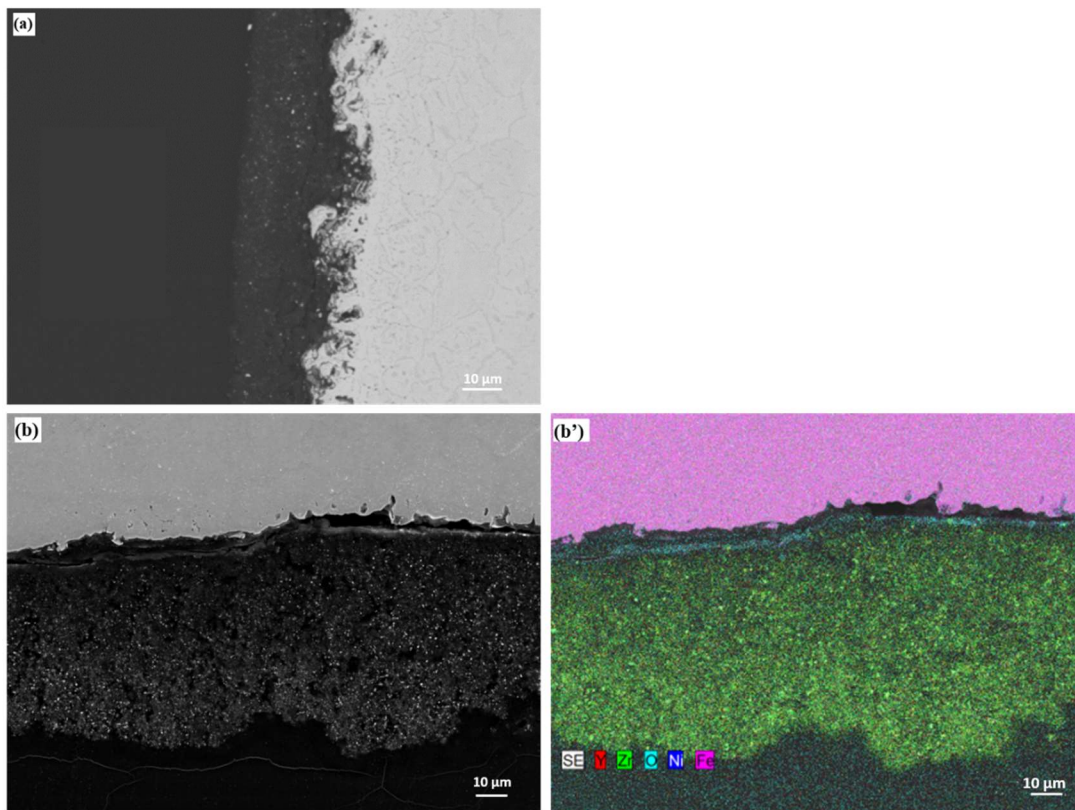


Figure 4.12 The cross-sectional morphologies of YSZ coatings on the (a) side and (b) back of the substrate deposited at the spraying distance of 450 mm using Set 5. Image (b') is the EDS result of (b).

4.3.2.3 XRD analysis

The XRD patterns of the YSZ powders and sprayed coatings deposited at different spraying distances using the Set 1 and Set 5 parameters are displayed in Figure 4.13. This reveals that the original YSZ powders consist of the low-temperature monoclinic phase (M) and the intermediate temperature tetragonal phase (T). After heating by the plasma jet of the LP-SPS process, the YSZ powders contained in the suspension are melted or even vaporized. As a consequence, the phase in the YSZ powders transforms from the low-temperature M phase to the intermediate temperature T phase. Then, the YSZ powders strike and solidify on the substrate with a rapid cooling, which turns the T phase into another non-equilibrium tetragonal phase (T'). The T' phase contains a high level of Y₂O₃ and is stable concerning the M phase, so it will not transform into the M phase even if the temperature drops to room temperature. As a result, all the YSZ coatings are composed of a combination of the T' phase and M phase.

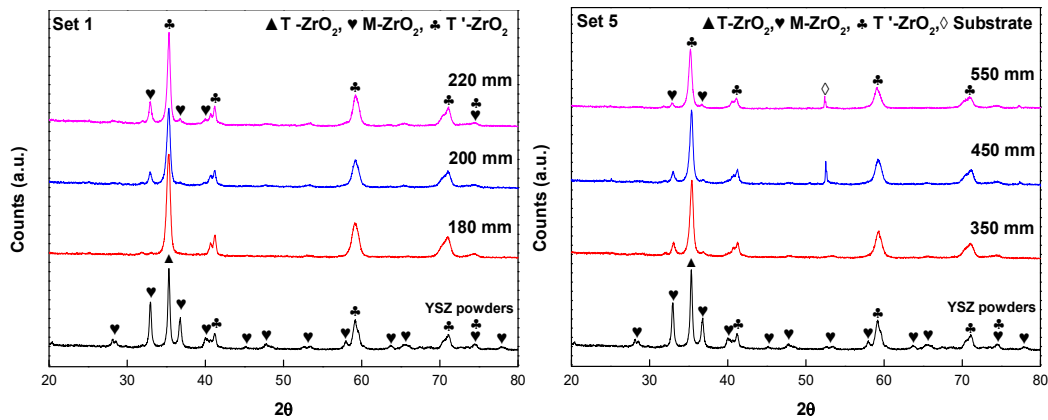


Figure 4.13 The XRD patterns of YSZ powders and sprayed coatings deposited at different spraying distances using Set 1 (top) and Set 5 (bottom).

Based on the above observations, it can be inferred that for the preparation of YSZ coatings by the LP-SPS process, the T' phase content is positively correlated with the melting state of the YSZ powders in the plasma jet. Therefore, in order to further analyze the melting state of the YSZ powders before deposition, the contents of the T and T' phase in the YSZ powders and the sprayed coatings were semi-quantitatively calculated based on the RIR method [36], as displayed in Figure 4.14.

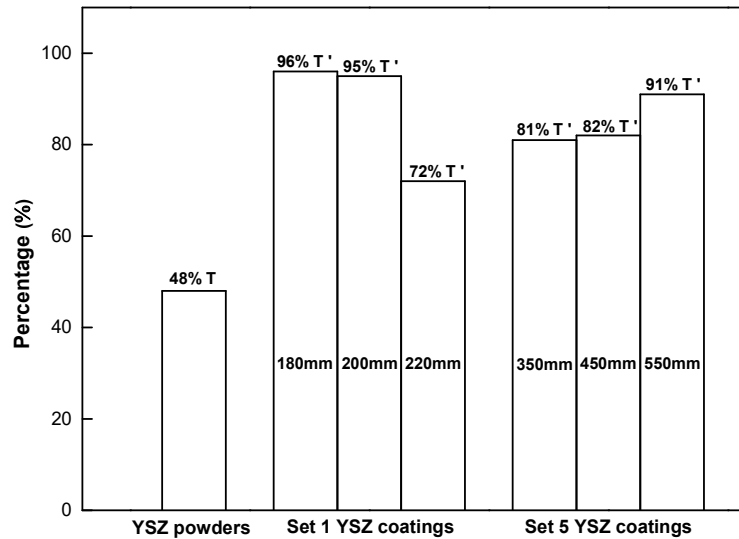


Figure 4.14 The contents of the T and T' phase in the YSZ powders and the sprayed coatings deposited at different spraying distances using Set 1 and Set 5.

The original YSZ powders contain 48% T phase and 52% M phase. After the treatment of the LP-SPS process using Set 1, the M phases of the 180 and 200 mm YSZ coatings almost disappear, while the T' phase content is as high as 96% and 95%, respectively. This indicates that the temperature of the plasma jet at 180 and 200 mm is high so that the YSZ powders are fully melted or even vaporized there, which leads to the complete transformation of the M phase into the T phase and then the formation of the T' phase after quenching. However, when the spraying distance increases to 220 mm, the T' phase of the 220 mm coating is reduced to 72% after quenching. This is because the temperature of the plasma jet rapidly drops at 200 mm. As a result, the previously formed metastable T phase is converted to the low-temperature M phase. By contrast, when the YSZ suspension is sprayed using Set 5, the variation of T' phase content with increasing spraying distance is opposite to that using Set 1. The T' phase of the 350 and 450 mm YSZ coatings is 81% and 82%, while that of the 550 mm YSZ coating is increased to 91%. This demonstrates that the M phase of YSZ powders is continuously transformed into the T phase with the increasing spraying distance. In other words, the use of helium and high power by Set 5 can achieve a high-temperature plasma jet over long spraying distances. Therefore, unlike sprayed using Set 1, the YSZ powders sprayed using Set 5 are heated for a longer time and exhibit a better melting state at a longer spraying distance.

Figure 4.15 presents the average crystallite sizes of the YSZ powders and the sprayed coatings, which were calculated by the Williamson-Hall equation [37-39]. The result illustrates that the average crystallite size of YSZ powders is 31.5 nm. After the LP-SPS process, all the average crystallite sizes of the YSZ coatings decreased. This could be attributed to the thorough melting of YSZ powders and their high cooling rates on the substrates.

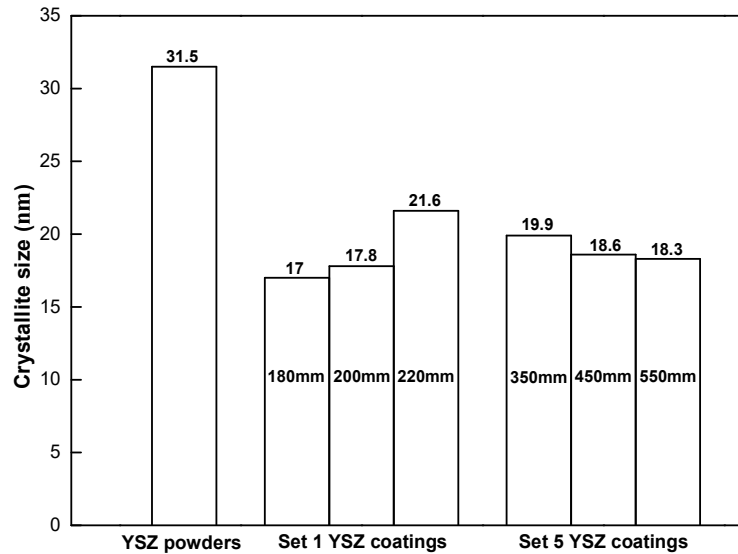


Figure 4.15 The crystallite sizes of the YSZ powders and the sprayed coatings deposited at different spraying distances using Set 1 and Set 5.

For the Set 1 YSZ coatings, the smallest average crystallite size of 17 nm appears at 180 mm, indicating that the YSZ powders are melted best there. As the spraying distance increases, the temperature of the plasma jet drops abruptly. Thus, the YSZ powders can no longer be melted efficiently but can only be sintered together by the plasma jet. As a result, the average crystallite size of YSZ coatings at 200 and 220 mm increases to 17.8 and 21.6 nm, respectively. However, for the Set 5 YSZ coatings, the average crystallite size changes in an opposite trend. The 350 mm YSZ coating has the largest average crystallite size of 19.9 nm, demonstrating that the melting of YSZ powders is insufficient there. As the spraying distance increases, the temperature of the plasma jet falls slowly through the use of the high plasma power and helium. Therefore, the YSZ powders are continuously heated in the plasma jet during the flight of 350–550mm, which leads to the average crystallite size of 450 and 550 mm

YSZ coatings decreasing to 18.6 and 18.3 nm, respectively. All the results of the average crystallite size are consistent with the corresponding microstructures of YSZ coatings, as illustrated in Figure 4.8 and 4.10.

4.3.2.4 Nanoindentation results

Figure 4.16 presents the typical load-displacement curves of cross-sectional YSZ coatings deposited using the Set 1 and Set 5 parameters. The load and the penetration depth into the polished cross-sections were continuously measured during the loading and unloading process. Additionally, all the test parameters for the YSZ coatings are the same. The results demonstrate that under the same indentation load, the displacement of the Set 1 YSZ coatings increases but that of the Set 5 YSZ coatings decreases with a longer spraying distance. Thus, the Set 1-180 mm coating displays the smallest displacement, while the Set 5-450 mm coating exhibits the largest displacement. This means that in general, the Set 5 YSZ coatings are softer than the Set 1 YSZ coatings. This can contribute to the fact that as a whole, the Set 5 YSZ coatings have a larger crystallite size and more nano-pores and inter-lamellar cracks.

Figure 4.17 shows the hardness and Young's modulus of cross-sectional YSZ coatings deposited using the Set 1 and Set 5 parameters. Among them, the 180 and 200 mm YSZ coatings of Set 1 have the best mechanical properties, with a hardness and Young's modulus of 7.5 ± 0.9 GPa, 139.5 ± 10.3 GPa, and 7.4 ± 0.7 GPa, 150.6 ± 3.9 GPa, respectively. By contrast, the 350 and 450 mm YSZ coatings of Set 5 have the worst mechanical properties, with a hardness and Young's modulus of 3.3 ± 0.4 GPa, 90.4 ± 5.7 GPa, and 2.6 ± 0.5 GPa, 153.8 ± 29.8 GPa, respectively. This is due to the structural differences caused by the melting state of YSZ powders. Since the 180 and 200 mm YSZ powders have the best melting state using the Set 1 parameter, the resulting coatings have the densest microstructure with good cohesion strength. Additionally, their crystallite sizes are the smallest, which further improves the mechanical properties of the coatings. This reason can also explain why the moderately melted YSZ powders can achieve middle mechanical properties at Set 1-

220 mm and at Set 5-550 mm, whose hardness and Young's modulus are 3.8 ± 0.7 GPa, 102.7 ± 10.5 GPa, and 4.5 ± 1.0 GPa, 91.1 ± 14.3 GPa, respectively.

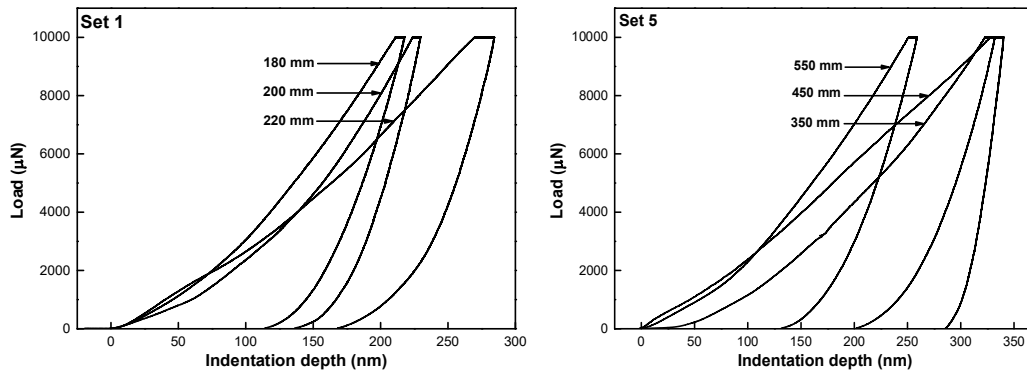


Figure 4.16 The load-displacement curves of cross-sectional YSZ coatings deposited by Set 1 and Set 5.

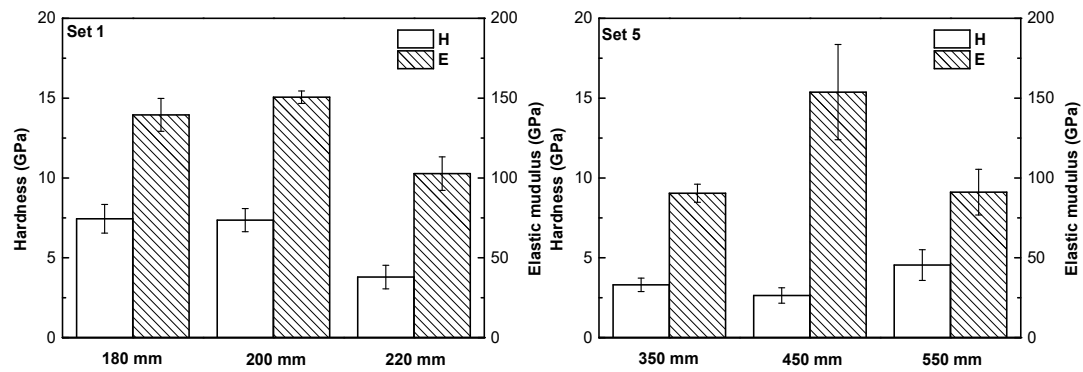


Figure 4.17 The hardness and Young's modulus of cross-sectional YSZ coatings deposited by Set 1 and Set 5.

A similar rule was found by Carpio et al. [40] when they studied a two-zone SPS-YSZ microstructure with fully molten areas and sintered-grains areas. In their study, the nanoindentation result showed two well-distinguished zones throughout the coatings, which displayed different hardness and elastic modulus. The molten zones also exhibited higher values of hardness and elastic modulus than those of the sintered-grain zones. In addition, the mechanical properties of the overall YSZ coating could be estimated from the average value between the mechanical properties of the two zones, as in the results of the present study.

4.4 Conclusions

With the design of a new bi-cathode plasma torch with an axial injection mode, the YSZ suspension was successfully deposited by the LP-SPS process. It not only overcame the difficulty of the radial powder feeding under low pressure but also enhanced the heat and mass transfer between the plasma jet and the YSZ powders. Various spraying parameters were studied in order to optimize the LP-SPS process. For the good spraying parameters, further analysis of the OES, SEM, XRD, and nanoindentation was performed. Some conclusions can be drawn as follows:

1) To obtain a high-quality LP-SPS YSZ coating at a relatively long spray distance, it is necessary to make the YSZ powders have the best melting state and impact velocity. In order to achieve this goal, it is advantageous to use higher power and larger He gas flow.

2) The YSZ vapor phase can be obtained in the LP-SPS process. The long plasma jet with high power and larger He gas flow is more beneficial for sustaining this vaporization.

3) The plasma jets under different operating pressures have different heating modes. The 100 mbar plasma jet can quickly melt the YSZ powders upstream, but only within a short spraying distance. The 6 mbar plasma jet can slowly melt the YSZ powders downstream but can maintain this over a wide spraying range.

4) The melting degree of the YSZ powders is a critical factor that affects their structure, phase, and performance. The fully melted YSZ powders make the resulting coating have a dense and uniform structure, high content of T' phase, and high hardness and Young's modulus.

References

- [1] X.Q. Cao, R. Vassen, D. Stoeber, Ceramic materials for thermal barrier coatings, *Journal of the European Ceramic Society* 24(1) (2004) 1-10.
- [2] J. Nielsen, J. Hjelm, Impedance of SOFC electrodes: A review and a comprehensive case study on the impedance of LSM:YSZ cathodes, *Electrochimica Acta* 115 (2014) 31-45.
- [3] A.B. Stambouli, E. Traversa, Solid oxide fuel cells (SOFCs): a review of an environmentally clean and efficient source of energy, *Renewable and sustainable energy reviews* 6(5) (2002) 433-455.
- [4] N.P. Padture, M. Gell, E.H. Jordan, Thermal barrier coatings for gas-turbine engine applications, *Science* 296(5566) (2002) 280-284.
- [5] K. Khor, Y. Gu, D. Pan, P. Cheang, Microstructure and mechanical properties of plasma sprayed HA/YSZ/Ti-6Al-4V composite coatings, *Biomaterials* 25(18) (2004) 4009-4017.
- [6] P.-j. He, S. Yin, C. Song, F. Lapostolle, H.-l. Liao, Characterization of Yttria-Stabilized Zirconia Coatings Deposited by Low-Pressure Plasma Spraying, *Journal of Thermal Spray Technology* 25(3) (2016) 558-566.
- [7] X. Chen, S. Kuroda, T. Ohnuki, H. Araki, M. Watanabe, Y. Sakka, Effects of processing parameters on the deposition of yttria partially stabilized zirconia coating during suspension plasma spray, *Journal of the American Ceramic Society* 99(11) (2016) 3546-3555.
- [8] P. Fauchais, Understanding plasma spraying, *Journal of Physics D: Applied Physics* 37(9) (2004) R86.
- [9] A. Vardelle, C. Moreau, N.J. Themelis, C. Chazelas, A perspective on plasma spray technology, *Plasma Chemistry and Plasma Processing* 35(3) (2015) 491-509.
- [10] L. Pawlowski, Suspension and solution thermal spray coatings, *Surface and Coatings Technology* 203(19) (2009) 2807-2829.
- [11] H. Kassner, R. Siegert, D. Hathiramani, R. Vassen, D. Stoeber, Application of suspension plasma spraying (SPS) for manufacture of ceramic coatings, *Journal of Thermal Spray Technology* 17(1) (2008) 115-123.
- [12] P. Fauchais, V. Rat, C. Delbos, J.F. Coudert, T. Chartier, L. Bianchi, Understanding of suspension DC plasma spraying of finely structured coatings for SOFC, *IEEE transactions on plasma science* 33(2) (2005) 920-930.

- [13] R. Rampon, F.L. Toma, G. Bertrand, C. Coddet, Liquid plasma sprayed coatings of yttria-stabilized zirconia for SOFC electrolytes, *Journal of Thermal Spray Technology* 15(4) (2006) 682-688.
- [14] P. Xu, J. Mostaghimi, T. Coyle, L. Pershin, Suspension Plasma Spray of Yttria Stabilized Zirconia Coatings, *Advances in High Temperature Ceramic Matrix Composites and Materials for Sustainable Development* 263 (2017) 451.
- [15] W. Fan, Y. Bai, Review of suspension and solution precursor plasma sprayed thermal barrier coatings, *Ceramics International* (2016).
- [16] N. Curry, Z. Tang, N. Markocsan, P. Nylén, Influence of bond coat surface roughness on the structure of axial suspension plasma spray thermal barrier coatings—Thermal and lifetime performance, *Surface and Coatings Technology* 268 (2015) 15-23.
- [17] M. Jadidi, M. Mousavi, S. Moghtadernejad, A. Dolatabadi, A Three-Dimensional Analysis of the Suspension Plasma Spray Impinging on a Flat Substrate, *Journal of Thermal Spray Technology* 24(1) (2015) 11-23.
- [18] A. Vardelle, C. Moreau, J. Akedo, H. Ashrafizadeh, C.C. Berndt, J.O. Berghaus, M. Boulos, J. Brogan, A.C. Bourtsalas, A. Dolatabadi, M. Dorfman, T.J. Eden, P. Fauchais, G. Fisher, F. Gaertner, M. Gindrat, R. Henne, M. Hyland, E. Irissou, E.H. Jordan, K.A. Khor, A. Killinger, Y.C. Lau, C.J. Li, L. Li, J. Longtin, N. Markocsan, P.J. Masset, J. Matejcek, G. Mauer, A. McDonald, J. Mostaghimi, S. Sampath, G. Schiller, K. Shinoda, M.F. Smith, A.A. Syed, N.J. Themelis, F.L. Toma, J.P. Trelles, R. Vassen, P. Vuoristo, The 2016 Thermal Spray Roadmap, *Journal of Thermal Spray Technology* 25(8) (2016) 1376-1440.
- [19] P.L. Fauchais, J.V. Heberlein, M.I. Boulos, *Thermal spray fundamentals: from powder to part*, Springer Science & Business Media 2014.
- [20] D. Zhou, O. Guillon, R. Vaßen, Development of YSZ Thermal Barrier Coatings Using Axial Suspension Plasma Spraying, *Coatings* 7(8) (2017) 120.
- [21] A. Ganvir, S. Joshi, N. Markocsan, R. Vassen, Tailoring columnar microstructure of axial suspension plasma sprayed TBCs for superior thermal shock performance, *Materials & Design* (2018).
- [22] A. Ganvir, V. Vaidhyanathan, N. Markocsan, M. Gupta, Z. Pala, F. Lukac, Failure analysis of thermally cycled columnar thermal barrier coatings produced by high-velocity-air fuel and axial-suspension-plasma spraying: A design perspective, *Ceramics International* 44(3) (2018) 3161-3172.
- [23] D. Waldbillig, O. Kesler, Characterization of metal-supported axial injection plasma sprayed solid oxide fuel cells with aqueous suspension plasma sprayed electrolyte layers, *Journal of Power Sources* 191(2) (2009) 320-329.

- [24] Y.X. Zhao, D.C. Li, X.H. Zhong, H.Y. Zhao, L. Wang, F. Shao, C.G. Liu, S.Y. Tao, Thermal shock behaviors of YSZ thick thermal barrier coatings fabricated by suspension and atmospheric plasma spraying, *Surface & Coatings Technology* 249 (2014) 48-55.
- [25] Z. Tang, H. Kim, I. Yaroslavski, G. Masindo, Z. Celler, D. Ellsworth, Novel thermal barrier coatings produced by axial suspension plasma spray, *International Thermal Spray Conference and Exposition (ITSC 2011)*, Hamburg, Germany, Sept, 2011, pp. 27-29.
- [26] P. Sokołowski, P. Nylen, R. Musalek, L. Łatka, S. Kozerski, D. Dietrich, T. Lampke, L. Pawłowski, The microstructural studies of suspension plasma sprayed zirconia coatings with the use of high-energy plasma torches, *Surface and Coatings Technology* 318 (2017) 250-261.
- [27] W.C. Oliver, G.M. Pharr, An improved technique for determining hardness and elastic modulus using load and displacement sensing indentation experiments, *Journal of materials research* 7(06) (1992) 1564-1583.
- [28] NIST Atomic Spectra Database Lines Form. https://physics.nist.gov/PhysRefData/ASD/lines_form.html.
- [29] G. Mauer, A. Hospach, R. Vaßen, Process development and coating characteristics of plasma spray-PVD, *Surface and Coatings Technology* 220 (2013) 219-224.
- [30] J. Aubreton, M. Elchinger, V. Rat, P. Fauchais, Two-temperature transport coefficients in argon–helium thermal plasmas, *Journal of Physics D: Applied Physics* 37(1) (2003) 34.
- [31] K. VanEvery, M.J. Krane, R.W. Trice, H. Wang, W. Porter, M. Besser, D. Sordelet, J. Ilavsky, J. Almer, Column formation in suspension plasma-sprayed coatings and resultant thermal properties, *Journal of thermal spray technology* 20(4) (2011) 817-828.
- [32] P. Klemens, Theory of thermal conduction in thin ceramic films, *International journal of thermophysics* 22(1) (2001) 265-275.
- [33] N. Shi, S. Yu, S. Chen, L. Ge, H. Chen, L. Guo, Dense thin YSZ electrolyte films prepared by a vacuum slurry deposition technique for SOFCs, *Ceramics International* 43(1, Part A) (2017) 182-186.
- [34] P. Fauchais, R. Etchart-Salas, C. Delbos, M. Tognonvi, V. Rat, J.-F. Coudert, T. Chartier, Suspension and solution plasma spraying of finely structured layers: potential application to SOFCs, *Journal of Physics D: Applied Physics* 40(8) (2007) 2394.
- [35] G. Schiller, R.H. Henne, M. Lang, R. Ruckdäschel, S. Schaper, Development of vacuum plasma sprayed thin-film SOFC for reduced operating temperature, *Fuel Cells Bulletin* 3(21) (2000) 7-12.

- [36] C.R. Hubbard, R.L. Snyder, RIR-measurement and use in quantitative XRD, *Powder Diffraction* 3(2) (1988) 74-77.
- [37] A.K. Zak, W.A. Majid, M.E. Abrishami, R. Yousefi, X-ray analysis of ZnO nanoparticles by Williamson–Hall and size–strain plot methods, *Solid State Sciences* 13(1) (2011) 251-256.
- [38] G. Williamson, W. Hall, X-ray line broadening from filed aluminium and wolfram, *Acta metallurgica* 1(1) (1953) 22-31.
- [39] V. Mote, Y. Purushotham, B. Dole, Williamson-Hall analysis in estimation of lattice strain in nanometer-sized ZnO particles, *Journal of Theoretical and Applied Physics* 6(1) (2012) 6.
- [40] P. Carpio, E. Rayón, L. Pawłowski, A. Cattini, R. Benavente, E. Bannier, M. Salvador, E. Sánchez, Microstructure and indentation mechanical properties of YSZ nanostructured coatings obtained by suspension plasma spraying, *Surface and Coatings Technology* 220 (2013) 237-243.

CHAPTER 5

Elaboration and Characterization of TiN Coatings Prepared by Low-Pressure Reactive Plasma Spray

Chapter 5 Elaboration and Characterization of TiN Coatings Prepared by Low-Pressure Reactive Plasma Spray

5.1 Introduction

Titanium and titanium alloys have been widely used in the aerospace, marine, chemical and medical industries, due to their strength-to-weight ratio weight ratio, excellent corrosion, and erosion resistance as well as unique biocompatibility [1-5]. However, they are rarely used in mechanical engineering applications due to their low surface hardness and poor tribological properties [6,7]. On the other hand, the interest in applying titanium and titanium alloys in automotive and other industries, where the tribological behavior of the system is a major influencing factor, is increasing. Improving their tribological performance is, therefore, the present challenge for materials scientists and engineers [8]. In fact, some surface treatments and coatings have been used to improve the wear properties of titanium and titanium alloys [9-14]. Among them, titanium nitride (TiN) coatings have been recognized as one of the most suitable materials, due to its high hardness and elastic modulus, similar thermal expansion coefficient, and excellent interfacial bonding with the matrixes of titanium and titanium alloys[15].

Currently, TiN coatings are mainly prepared by physical vapor deposition (PVD) or chemical vapor deposition (CVD) [16-18]. Nevertheless, due to the low efficiency of deposition, the obtained TiN coatings are usually very thin ($<10\ \mu\text{m}$), which limits their applications [19]. Previous studies show that the performance of TiN coating depends on its thickness; for example, the thicker the TiN coating, the better the wear resistance and corrosion resistance. Moreover, if the thickness of the TiN coating is less than $12\ \mu\text{m}$, it cannot resist the osmosis of corrosives. Therefore, making the TiN coating thick is an excellent way to obtain better performance [20].

Reactive plasma spray (RPS) technology is a promising method of preparing a thick TiN coating with a high deposition rate. The Ti powders are injected into a plasma jet, heated, melted, and they then react with reactive N₂ gas introduced into the plasma jet (sometimes as a working gas). The high-temperature plasma jet favors the conditions for the reactions so that the TiN coating can be formed despite the short dwell time and the steep temperature gradients in a DC plasma jet. As mentioned in previous research works, it is possible to synthesize thick TiN coatings by using the atmospheric or low-pressure RPS technology [20-25]. For example, Xiao et al. [20] prepared more than 300 μm nanostructured TiN coatings using the atmospheric RPS. The obtained coating had a primary phase of TiN as well as many Ti₃O phases. Besides, the oxidization was intensified with the increased input power. On the other hand, Vautherin et al. [23] fabricated a 27 μm TiN coating using the low-pressure RPS. Although the oxides were no longer present in the coating, the nitridation reaction of the coating was incomplete due to the insufficient plasma power, so it contained a large amount of TiN_{0.3}, Ti₂N, and unmelted Ti.

To overcome the disadvantages of the two RPS processes mentioned above, the present study applied an enhanced low-pressure reactive plasma spray (LP-RPS) to *in-situ* synthesize the TiN coatings on the Ti-6Al-4V alloy. The nitriding reaction was performed at a high plasma power (120 kW) and a very low pressure (150 Pa), which could offer sufficient activation energy for the nitridation and minimize the oxidation [26]. As a result, the relatively pure TiN coatings without oxides were successfully prepared by using the LP-RPS. The influences of the spraying distances on the vaporization degree, the nitriding effect and the microstructure of TiN coatings were discussed. The mechanical properties of the TiN coatings and the Ti-6Al-4V substrate were also investigated.

5.2 Experimental Procedures

5.2.1 Spraying Material

Commercially available Ti powders (AP&C Inc, Canada) with a particle size between 8 and 24 μm ($d_{50}=15 \mu\text{m}$) was used as the feedstock. These powders had a good sphericity and facilitated the feeding in the LP-RPS process. Their morphology and chemical composition are illustrated in Figure 5.1 and Table 5.1, respectively.

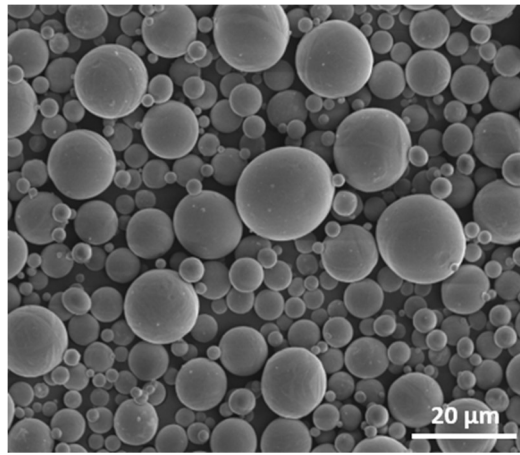


Figure 5.1 The morphology of the Ti powders.

Table 5.1 Chemical composition of the Ti powders.

Composition	Ti	O	Fe	C	N
Wt.%	Balance	0.07-0.18	< 0.20	0.02	0.02

5.2.2 Coating Preparation

The MultiCoat™ hybrid plasma coating system (Oerlikon Metco, Switzerland) equipped with an O3CP plasma torch was employed to prepare the TiN coatings, as shown in Figure 5.2. The reaction gas of N_2 was injected into the plasma jet by three ways, including working gas, carrier gas, and a perforated ring. The perforated ring was applied to inject additional N_2 into the plasma jet, which was positioned downstream of the nozzle at 150 mm away. The disks of Ti-6Al-4V alloy (26 mm diameter, 5 mm thick) were chosen as the substrates, which were polished until $R_a=0.1 \mu\text{m}$ and then ultrasonically cleaned in alcohol. All the substrates were

preheated up to 900°C using the plasma jet before spraying. The substrate temperature was recorded by an infrared thermometer. The detailed spraying parameters are listed in Table 5.2.

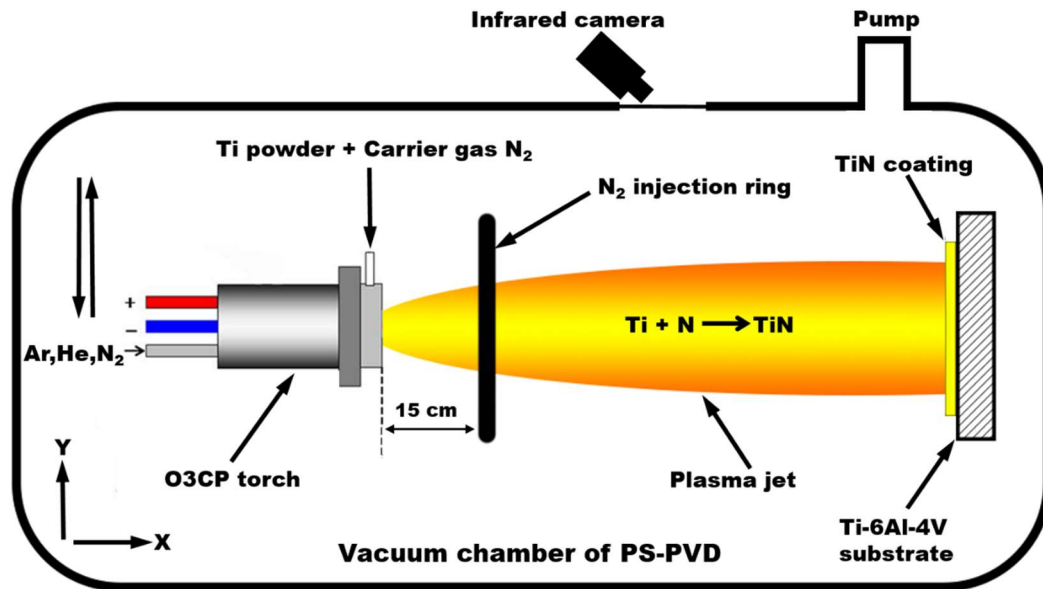


Figure 5.2 The schematic diagram for preparing TiN coating using LP-RPS.

Table 5.2 LP-RPS parameters.

Parameters	Value
Pressure (Pa)	150
Current (A)	2000
Voltage (V)	60
Power (kW)	120
Net power (kW)	60
Plasma gas (Ar) (slpm) ^a	30
Plasma gas (He) (slpm) ^a	45
Plasma gas (N ₂) (slpm) ^a	15
Carrier gas (N ₂) (slpm) ^a	17
N ₂ from perforated ring (slpm) ^a	18
Powder feed rate (g·min ⁻¹)	2.5
Spraying distance (mm)	500, 900
Substrates temperature (°C)	1250, 950

^a slpm: standard liter per minute.

5.2.3 Characterization

The plasma properties with Ti powders were characterized by optical emission spectroscopy (OES). An X-ray diffractometer (Rigaku, Japan) was used to determine the phases in the powders and the coatings. The microstructural characterization was performed using a Nova Nanosem 450 field emission scanning electron microscopy (FEI, Hillsboro, OR, USA) equipped with a “Hikari” EBSD camera (Ametek-EDAX) operating under an acceleration voltage of 20 kV and with a spot size of 6 and a step size of 6 nm. The cross-sectional nano-indentation test was conducted using a nano-indenter (Hysitron, USA) with a diamond Berkovich tip at a maximum load of 10 mN. The hardness and elastic modulus were calculated using the Oliver and Pharr method [26].

5.3 Results and Discussions

5.3.1 Plasma Jet Diagnostics

Figure 5.3 shows the OES spectrums of the plasma jets with Ti powders at 500 and 900 mm. For the two spraying distances, the spectrum of plasma gas intensively distributes in a wavelength range from 600 to 900 nm, while the major signal of Ti comes from 500 to 600 nm. Compared with the emissions of plasma gas, the intensities of Ti at the two spraying distances are relatively high, indicating that sufficient Ti powders had been vaporated. For a further study, the plasma electron temperatures T_e at two spraying distances are estimated using the relative intensity method [27,28]:

$$T_e = \frac{E_1 - E_2}{k} \left[\ln \left(\frac{A_1 g_1 \lambda_2 I_2}{A_2 g_2 \lambda_1 I_1} \right) \right]^{-1} \quad (5.1)$$

Here, E, k, A, g, λ , I, represent the excitation energy, the Boltzmann constant, the transition probability, the statistical weight, the wavelength, and the spectral intensity, respectively. Based on the relative intensity of N I (744.23 nm) and N I (868.34 nm) in Figure 5.3, the T_e calculated at 500 mm and 900 mm are 4016 K and

3851 K, respectively. The Te only decreases a little with increased spraying distance, suggesting that the Ti powders could be efficiently heated until 900 mm. Therefore, the vaporization degree of Ti powders at 900 mm would be higher than at 500 mm. It could also explain why the absolute intensity of Ti spectrum is reduced at 900 mm because of the low concentration, but the relative intensity of Ti spectrum is not weakened compared to the plasma gas.

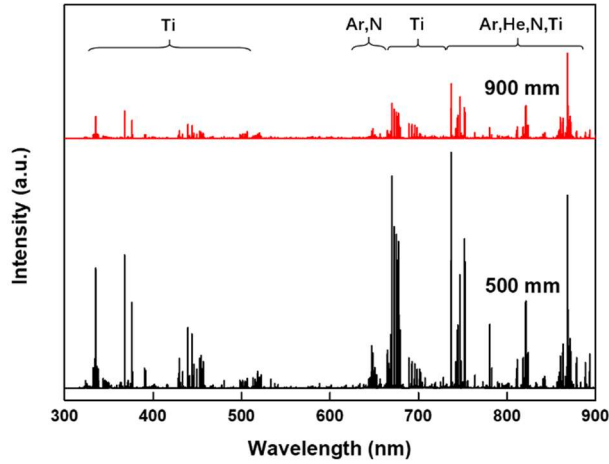


Figure 5.3 The OES patterns of the plasma jet with Ti powders at 500 and 900 mm

5.3.2 XRD Analysis

The X-ray diffraction patterns of Ti powders and as-sprayed coatings are presented in Figure 5.4. For the two spraying distances, the primary reaction products are TiN, $(\text{TiN})_{0.88}$ and small quantities of $\text{TiN}_{0.3}$. The absence of Ti peaks means the nitridation reaction is almost complete. Semiquantitative phase analysis is carried out based on the RIR method, showing that the 500 mm coating contains TiN (94.3%), $\text{TiN}_{0.3}$ (5.7%), whereas the 900 mm coating contains $\text{TiN}+(\text{TiN})_{0.88}$ (91%), $\text{TiN}_{0.3}$ (9%). The better nitridation occurs at 500 mm where it has a lower vaporization degree based on the OES results, which demonstrates that the vaporization degree is an important but not decisive factor for the nitriding reaction. In other words, the nitriding reaction occurs not only in the plasma jet but also on the substrate [23]. Because the concentrations of reactants and substrate temperature are higher at 500 mm, more N and Ti powders can react due to the higher activation energy.

Meanwhile, the higher substrate temperature will enhance the diffusion rate of N in the Ti lattice. Therefore, more N can be introduced into the Ti lattice at 500 mm, making its interplanar spacing greater than 900 mm, thus the 500 mm pattern shifts slightly to a lower angle. A further nitriding mechanism needs to be investigated in the future.

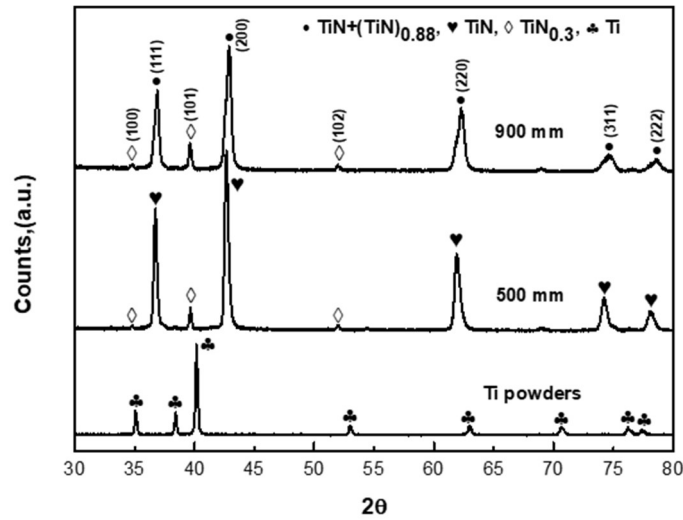


Figure 5.4 The XRD patterns of the raw Ti powders and as-sprayed coatings.

5.3.3 Microstructural Analysis

The SEM studies of the TiN coatings at two distances are shown in Figure 5.5 (a) and (b). The two coatings are composed of hybrid deposition from liquid splats, clusters, and vapor phases, which result from the medium vaporization. This is because the N₂ in working gas could broaden the plasma jet, and consume considerable plasma energy for its dissociation and partial ionization. Nevertheless, the hybrid structures of TiN coatings between the two spraying distances are different. The TiN coating at 500 mm is a denser lamellar structure while at 900 mm is a more porous columnar structure. This is a result of their different vaporization degrees, reactant concentrations and substrate temperatures. For the 500 mm, when the splats impinge on the substrate, they are well-flattened and form disc-shaped lamellas. The following clusters and vapor will adhere, diffuse and nucleate on the splats or substrate. If without disturbance, the nuclei will grow into columnar crystals by three-

dimensional island growth [29]. However, owing to the high reactant concentrations and low vaporization degree at 500 mm, lots of splats will cover the columns and fill their gaps, thus interrupting the column growth. Moreover, the high substrate temperature at 500 mm will intensify the surface diffusion and weaken the shadowing effect. Therefore, a packed laminar structure with few defects will be formed. Nevertheless, this splat growth will be inhibited at 900 mm due to its low reactant concentrations and high vaporization degree, so the growth of clusters and vapor could be developed to form columnar crystals. Besides, the low substrate temperature at 900 mm makes the shadowing effects predominate in the surface diffusion, which favors the clusters and vapor nucleating on the existing column. Thus a porous columnar structure with more defects will form.

The microstructural differences between the two TiN coatings are more visible by EBSD technique, as shown in Figure 5.5 (c) and (d). The deposition of TiN coating at 500 mm is mainly composed of the splats with equiaxed grains, in addition to a small part of vapor with the columnar grains. As the spraying distance increases to 900 mm, more clusters and vapor would be deposited to form columnar grains due to the enhanced vaporization degree. It not only loosens the coating structure at 900mm but also reduces its grain size. Consequently, while the spraying distance increases from 500 mm to 900 mm, the average grain size of TiN coating decreases from 260 nm to 50 nm. Clearly, the low substrate temperature at 900 mm is another critical factor in keeping the grain small because of the higher condensate depression and cooling velocity. Besides, according to the inverse pole figures, the two TiN coatings do not exhibit distinct preferred orientation, as grown in the case of PVD or CVD [30,31], which could be attributed to the partial vaporization. The droplets and clusters are randomly orientated and difficult to diffuse or reorient during deposition.

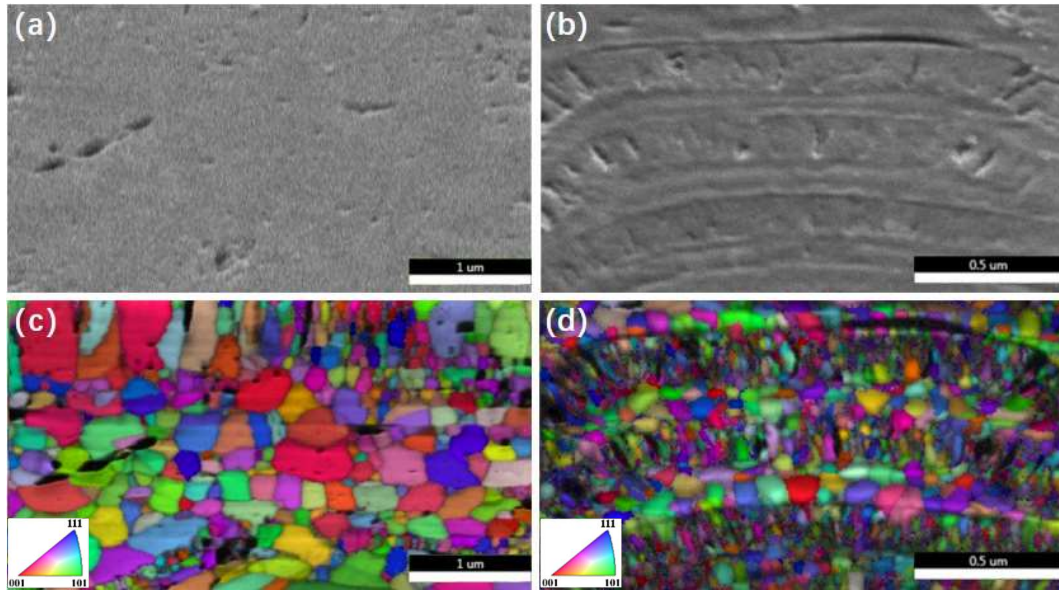


Figure 5.5 The cross-sectional morphologies of the coatings at (a) 500mm and (b) 900 mm. The corresponding inverse pole figure (IPF) + image quality (IQ) maps at (c) 500mm and (d) 900 mm.

5.3.4 Nanoindentation Results

The typical load-displacement curves for the cross-sectional TiN coatings and the Ti-6Al-4V substrate are illustrated in Figure 5.6. All the loading and unloading curves are smooth without a visible platform and abrupt change, indicating that the coatings have microstructural uniformity and no sudden fracture. In addition, through depositing the TiN coating on the Ti-6Al-4V substrate, the penetration depth of the indenter is significantly decreased, demonstrating that the Ti-6Al-4V substrate is reinforced by the TiN coating. The mechanical properties of the TiN coating and the Ti-6Al-4V substrate are summarized in Table 2. Compared with the unreinforced substrate, a significant increase in the average microhardness (H) and Young's modulus (E) can be found in the two TiN coatings. Besides, the TiN coating at 500 mm possesses higher H and E, which could be attributed to its better nitridation reaction and denser hybrid structure. Recent studies have shown that elastic strain to failure, which is related to the ratio of hardness (H) and elastic modulus (E), is a more suitable parameter for predicting wear resistance than using hardness alone [32]. Therefore, the average H/E ratios of the TiN coatings and the Ti-6Al-4V substrate

were calculated as reliable indicators of good wear resistance. The results show that the wear resistance of the Ti-6Al-4V substrate could be improved by depositing TiN coating, and the TiN coatings at 500 mm have better wear resistance, which means it could remain elastic under higher stresses.

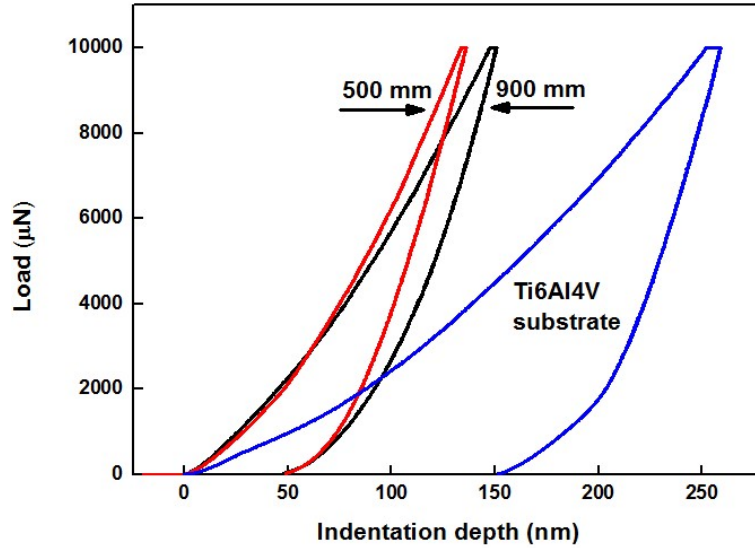


Figure 5.6 Load-displacement curves of the TiN coatings at 500 mm, 900 mm and the Ti-6Al-4V substrate.

Table 5.3 Mechanical properties of the TiN coatings and the Ti-6Al-4V substrate.

Samples	H (GPa)	E (GPa)	H/E ratio
500mm-TiN	16.3±1.9	234.2±17.8	0.070
900mm-TiN	13.4±3.4	202.9±26.5	0.066
Ti-6Al-4V	5.81±0.4	132.3±4.3	0.044

5.4 Conclusions

In summary, the hybrid-structured TiN coatings were successfully synthesized by using an enhanced LP-RPS process, which was not previously achieved with other thermal spraying processes. The nitriding reaction occurred not only in the plasma jet but also on the substrate. With increasing spraying distance, the nitriding effect was weakened, and the hybrid structure of TiN coating changed from dense laminar to porous columnar, according to the higher vaporization degree, decreasing reactant concentrations and lower substrate temperature. As a result, the average hardness and

Young's modulus of TiN coatings decreased from 16.3 ± 1.9 to 13.4 ± 3.4 and from 234.2 ± 17.8 GPa to 202.9 ± 26.5 GPa, respectively. Nevertheless, they can also improve the mechanical properties of the Ti-6Al-4V substrate, whose average microhardness and Young's modulus are 5.81 ± 0.4 and 132.3 ± 4.3 GPa, respectively.

References

- [1] C. Leyens, M. Peters, Titanium and titanium alloys: fundamentals and applications, John Wiley & Sons 2003.
- [2] I. Gurrappa, Characterization of titanium alloy Ti-6Al-4V for chemical, marine and industrial applications, *Materials Characterization* 51(2) (2003) 131-139.
- [3] C. Elias, J. Lima, R. Valiev, M. Meyers, Biomedical applications of titanium and its alloys, *Jom* 60(3) (2008) 46-49.
- [4] D.M. Brunette, P. Tengvall, M. Textor, P. Thomsen, Titanium in medicine: material science, surface science, engineering, biological responses and medical applications, Springer Science & Business Media 2012.
- [5] M. Peters, J. Kumpfert, C.H. Ward, C. Leyens, Titanium alloys for aerospace applications, *Advanced Engineering Materials* 5(6) (2003) 419-427.
- [6] A. Zhecheva, W. Sha, S. Malinov, A. Long, Enhancing the microstructure and properties of titanium alloys through nitriding and other surface engineering methods, *Surface and Coatings Technology* 200(7) (2005) 2192-2207.
- [7] X.-B. Liu, X.-J. Meng, H.-Q. Liu, G.-L. Shi, S.-H. Wu, C.-F. Sun, M.-D. Wang, L.-H. Qi, Development and characterization of laser clad high temperature self-lubricating wear resistant composite coatings on Ti-6Al-4V alloy, *Materials & Design* 55 (2014) 404-409.
- [8] L. Zhao, E. Lugscheider, Reactive plasma spraying of TiAl6V4 alloy, *Wear* 253(11) (2002) 1214-1218.
- [9] H.C. Man, M. Bai, F.T. Cheng, Laser diffusion nitriding of Ti-6Al-4V for improving hardness and wear resistance, *Applied Surface Science* 258(1) (2011) 436-441.
- [10] D.G. Bansal, O.L. Eryilmaz, P.J. Blau, Surface engineering to improve the durability and lubricity of Ti-6Al-4V alloy, *Wear* 271(9-10) (2011) 2006-2015.
- [11] A.F. Saleh, J.H. Abboud, K.Y. Benyounis, Surface carburizing of Ti-6Al-4V alloy by laser melting, *Optics and Lasers in Engineering* 48(3) (2010) 257-267.
- [12] Y.F. Liu, J.S. Mu, X.Y. Xu, S.Z. Yang, Microstructure and dry-sliding wear properties of TiC-reinforced composite coating prepared by plasma-transferred arc weld-surfacing process, *Materials Science and Engineering: A* 458(1-2) (2007) 366-370.

- [13] X. Liu, P.K. Chu, C. Ding, Surface modification of titanium, titanium alloys, and related materials for biomedical applications, *Materials Science and Engineering: R: Reports* 47(3–4) (2004) 49-121.
- [14] M. Das, V.K. Balla, D. Basu, S. Bose, A. Bandyopadhyay, Laser processing of SiC-particle-reinforced coating on titanium, *Scripta Materialia* 63(4) (2010) 438-441.
- [15] D. Nolan, S.W. Huang, V. Leskovsek, S. Braun, Sliding wear of titanium nitride thin films deposited on Ti–6Al–4V alloy by PVD and plasma nitriding processes, *Surface and Coatings Technology* 200(20–21) (2006) 5698-5705.
- [16] L. Ceschini, E. Lanzoni, C. Martini, D. Prandstraller, G. Sambogna, Comparison of dry sliding friction and wear of Ti6Al4V alloy treated by plasma electrolytic oxidation and PVD coating, *Wear* 264(1) (2008) 86-95.
- [17] H.E. Rebenne, D.G. Bhat, Review of CVD TiN coatings for wear-resistant applications: deposition processes, properties and performance, *Surface and Coatings Technology* 63(1) (1994) 1-13.
- [18] C. Martini, L. Ceschini, A comparative study of the tribological behaviour of PVD coatings on the Ti-6Al-4V alloy, *Tribology International* 44(3) (2011) 297-308.
- [19] F. Lang, Z. Yu, The corrosion resistance and wear resistance of thick TiN coatings deposited by arc ion plating, *Surface and Coatings Technology* 145(1–3) (2001) 80-87.
- [20] L. Xiao, D. Yan, J. He, L. Zhu, Y. Dong, J. Zhang, X. Li, Nanostructured TiN coating prepared by reactive plasma spraying in atmosphere, *Applied Surface Science* 253(18) (2007) 7535-7539.
- [21] A. Kobayashi, Formation of TiN coatings by gas tunnel type plasma reactive spraying, *Surface and Coatings Technology* 132(2–3) (2000) 152-157.
- [22] E. Galvanetto, F.P. Galliano, F. Borgioli, U. Bardi, A. Lavacchi, XRD and XPS study on reactive plasma sprayed titanium–titanium nitride coatings, *Thin Solid Films* 384(2) (2001) 223-229.
- [23] B. Vautherin, M.P. Planche, A. Quet, L. Bianchi, G. Montavon, Manufacturing of composite titanium-titanium nitride coatings by reactive very low pressure plasma spraying (R-VLPPS), *Journal of Physics: Conference Series* 550(1) (2014) 12035-12044.
- [24] T. Bacci, L. Bertamini, F. Ferrari, F.P. Galliano, E. Galvanetto, Reactive plasma spraying of titanium in nitrogen containing plasma gas, *Materials Science and Engineering: A* 283(1–2) (2000) 189-195.

- [25] G. Ingo, S. Kaciulis, A. Mezzi, T. Valente, F. Casadei, G. Gusmano, Characterization of composite titanium nitride coatings prepared by reactive plasma spraying, *Electrochimica Acta* 50(23) (2005) 4531-4537.
- [26] W.C. Oliver, G.M. Pharr, An improved technique for determining hardness and elastic modulus using load and displacement sensing indentation experiments, *Journal of materials research* 7(06) (1992) 1564-1583.
- [27] J. Cui, Z. Xu, J. Zhang, Q. Nie, G. Xu, L. Ren, Online diagnosis of electron excitation temperature in CH₄+H₂ discharge plasma at atmospheric pressure by optical emission spectra, *Science in China Series G: Physics, Mechanics and Astronomy* 51(12) (2008) 1892-1896.
- [28] N. Zhang, F. Sun, L. Zhu, M.P. Planche, H. Liao, C. Dong, C. Coddet, Electron Temperature and Density of the Plasma Measured by Optical Emission Spectroscopy in VLPPS Conditions, *Journal of Thermal Spray Technology* 20(6) (2011) 1321-1327.
- [29] J. Venables, G. Spiller, M. Hanbucken, Nucleation and growth of thin films, *Reports on Progress in Physics* 47(4) (1984) 399.
- [30] M.I. Jones, I.R. McColl, D.M. Grant, Effect of substrate preparation and deposition conditions on the preferred orientation of TiN coatings deposited by RF reactive sputtering, *Surface and Coatings Technology* 132(2) (2000) 143-151.
- [31] G. Abadias, Stress and preferred orientation in nitride-based PVD coatings, *Surface and Coatings Technology* 202(11) (2008) 2223-2235.
- [32] A. Leyland, A. Matthews, On the significance of the H/E ratio in wear control: a nanocomposite coating approach to optimised tribological behaviour, *Wear* 246(1-2) (2000) 1-11.

Conclusions and Perspectives

Conclusions and Perspectives

Conclusions

The purpose of this work was to further improve and develop the LPPS process by combining it with the emerging suspension plasma spray and reactive plasma spray processes. To realize them, two LPPS equipment was used, and a bi-cathode plasma torch was designed. The YSZ and TiN coatings were fabricated by using the combined processes, and the main conclusions were as following:

1) The bi-cathode plasma torch with axial injection mode was able to inject either the very fine-particle suspension or the micro-sized powders into the plasma center under low pressures. As a result, the heat and mass transfer between the plasma jet and the sprayed materials could be enhanced, and the feedstock could be vaporized under low pressure. However, the amount of vaporization is limited for ceramic powders.

2) The YSZ coatings were prepared from the powders and suspensions, respectively, by using this bi-cathode plasma torch. Both of the feedstock could be partially vaporized. The results indicated that all the YSZ coatings exhibited relatively dense structures due to the high velocity of particles under low pressures. The coatings were composed of the melted particles, the agglomerated particles as well as the vapor deposition. It was found that the vaporization degree of YSZ was increased by using smaller particle size, lower ambient pressure, longer spraying distance and higher plasma power. In addition, all the YSZ coatings underwent a significant phase transformation from a monoclinic phase to a tetragonal phase, and the transformation degree was proportional to the vaporization degree. However, the mechanical properties of the resulting coatings had the opposite behaviors. The YSZ coatings prepared from the agglomerated particles, which had a bigger droplet size and less vapor deposition, showed a higher hardness and Young's modulus than the YSZ coatings fabricated from fine suspension did.

3) The relatively pure TiN coatings with hybrid microstructure were successfully synthesized by using an enhanced LP-RPS, which was not previously achieved with other thermal spraying processes. The nitriding reaction occurred not only in the plasma jet but also on the substrate. With increasing spraying distance, the nitriding effect was weakened, and the hybrid structure of TiN coating changed from dense laminar to porous columnar, according to the higher vaporization degree, decreasing reactant concentrations and lower substrate temperature. As a result, the average hardness and Young's modulus of TiN coatings decreased from 16.3 ± 1.9 to 13.4 ± 3.4 and from 234.2 ± 17.8 GPa to 202.9 ± 26.5 GPa, respectively. Nevertheless, they can also improve the mechanical properties of the Ti-6Al-4V substrate, whose average microhardness and Young's modulus are 5.81 ± 0.4 and 132.3 ± 4.3 GPa, respectively.

Perspectives

Although the two combined process can produce high-quality ceramic coatings, there are still some problems that need to be solved, as follows:

1) The LPPS system with the bi-cathode plasma torch should be improved, as the water-cooling system takes much energy away during the spraying process. Moreover, the expansion portion of the anode nozzle in the bi-cathode plasma torch should be modified since the resulting plasma jet is not long enough under low pressure.

2) For the YSZ coatings prepared by the low-pressure suspension plasma spray, the YSZ powders with a larger particle size (e.g., $0.5\text{--}1\ \mu\text{m}$) should be essayed because they are easier to achieve $St > 1$. In addition, the content of YSZ powders in the suspension should be increased appropriately to obtain higher deposition efficiency.

3) For the TiN coatings prepared by the low-pressure reactive plasma spray, under the premise of ensuring complete nitriding, the plasma power of 120 kW and the He gas flow of 45 slpm should be reduced to lower the operating cost of PS-PVD. Moreover, other kinds of coatings such as TiC and AlN should be attempted by using the LP-RPS method.

4) Finally, other physical or chemical properties of the YSZ and TiN coatings should be further characterized to examine the feasibility of their application. For example, the thermal and electrical conductivity of the YSZ coatings, and the wear and corrosion resistance of the TiN coatings. The further characterization will also help to better understand the correlation between spraying parameters and coating properties.

Abstract

As an advanced thermal spray technology, low-pressure plasma spray (LPPS) allows obtaining high-quality coatings and can bridge the thickness gap between conventional thermal spray technologies and standard thin film processes. Moreover, LPPS permits to build uniform coatings with various microstructures; deposition takes place not only from liquid splats but also from nano-sized clusters as well as from the vapor phase depending on operational conditions. To further improve and develop the LPPS process, this research aims to combine it with the emerging suspension plasma spray and reactive plasma spray processes. It was expected to both provide two novel integrated processes and achieve fine-structured coatings with unique microstructures and high performance.

A bi-cathode plasma torch (the LERMPS lab, UTBM, France) with an axial injection mode was designed and built for LPPS, whose maximum input plasma power was able to reach 81 kW. By using this new torch, either the very fine-particle suspension or the micro-sized powders was able to be injected into the plasma center under low pressures. As a result, the heat and mass transfer between the plasma jet and the sprayed materials were enhanced.

The axial bi-cathode plasma torch was applied firstly to spray two kinds of YSZ feedstock, including the YSZ suspension and the YSZ agglomerated powders. The results indicated that all the YSZ coatings exhibited relatively dense structures due to the high velocity of particles under low pressures. The coatings were composed of the melted particles, the agglomerated particles as well as the vapor deposition. It was found that the vaporization degree of YSZ was increased by using smaller particle size, lower ambient pressure, longer spraying distance and higher plasma power. In addition, all the YSZ coatings underwent a significant phase transformation from a monoclinic phase to a tetragonal phase, and the transformation degree was proportional to the vaporization degree. However, the mechanical properties of the resulting coatings had the opposite behaviors. The YSZ coatings prepared from the agglomerated particles, which had a bigger droplet size and less vapor deposition,

showed a higher hardness and Young's modulus than the YSZ coatings fabricated from fine suspension did.

Another high-energy plasma torch O3CP (Oerlikon Metco, Switzerland) was employed to in-situ synthesize the TiN coatings on Ti-6Al-4V alloys by reactive plasma spray under very low pressure. The pure Ti powders were sprayed into an N₂ atmosphere under an input plasma power of 120 kW. The hybrid structured TiN coatings were synthesized, which was not previously achieved with other thermal spraying processes. It was known that the nitriding reaction occurred not only in the plasma jet but also on the substrate. Additionally, with increasing spraying distance, the nitriding effect was weakened, and the hybrid structure of TiN coating changed from dense laminar to porous columnar, according to the higher vaporization degree, lower reactant concentration and colder substrate. Nevertheless, they also were able to improve the mechanical properties of the Ti-6Al-4V substrate.

Keywords: Suspension plasma spray at low pressure; Reactive plasma spray at low pressure; Axial bi-cathode plasma torch; Yttria-stabilized zirconia coating; Titanium nitride coating.

Résumé

En tant que technologie de projection thermique avancée, la projection plasma sous basse pression (LPPS) permet d'obtenir des revêtements de haute qualité et peut combler l'écart d'épaisseur entre les technologies de projection thermique conventionnelles et les procédés de couche mince standard. En outre, LPPS permet de construire des revêtements uniformes avec diverses microstructures; le dépôt a lieu non seulement à partir des éclaboussures liquides, mais aussi à partir des amas nanométriques ainsi que de la phase vapeur en fonction des conditions opérationnelles. Afin de continuer à améliorer et à développer le procédé LPPS, cette recherche vise à le combiner avec les procédés émergents de projection plasma en suspension et de projection plasma réactif. Il devait à la fois fournir deux nouveaux processus intégrés et réaliser des revêtements à structure fine avec des microstructures uniques et des performances élevées.

Une torche à plasma bi-cathode (laboratoire de LERMPS, UTBM, France) à mode d'injection axiale a été conçue et construite pour le LPPS, dont la puissance maximale en entrée du plasma a pu atteindre 81 kW. En utilisant cette nouvelle torche, soit la suspension à très fines particules, soit les poudres micrométriques ont pu être injectées dans le centre du plasma à basse pression. En conséquence, le transfert de chaleur et de masse entre le jet de plasma et les matériaux pulvérisés a été amélioré.

La torche à plasma bi-cathode axiale a été appliquée d'abord pour pulvériser deux types de charges de YSZ, y compris la suspension de YSZ et les poudres agglomérées de YSZ. Les résultats ont indiqué que tous les revêtements YSZ présentaient des structures relativement denses en raison de la grande vitesse des particules sous faibles pressions. Les revêtements ont été composés des particules fondues, des particules agglomérées ainsi que du dépôt en phase vapeur. Il a été constaté que le degré de vaporisation de YSZ a été augmenté en utilisant une taille de particule plus fine, une pression ambiante plus basse, une distance de pulvérisation plus longue et une puissance de plasma plus élevée. En outre, tous les revêtements YSZ ont subi une transformation de phase significative d'une phase monoclinique à

une phase tétragonale, et le degré de transformation était proportionnel au degré de vaporisation. Cependant, les propriétés mécaniques des revêtements résultants ont des comportements opposés. Les revêtements YSZ préparés à partir des particules agglomérées, qui avaient une plus grande taille de gouttelettes et moins de dépôt en phase vapeur, présentaient une dureté et un module de Young plus élevés que les revêtements YSZ fabriqués à partir d'une suspension fine.

Une autre torche à plasma à haute énergie O3CP (Oerlikon Metco, Suisse) a été utilisée pour synthétiser in situ les revêtements de TiN sur des alliages de Ti-6Al-4V par projection de plasma réactive à très basse pression. Les poudres de Ti pur ont été pulvérisées dans une atmosphère de N₂ sous une puissance de plasma d'entrée de 120 kW. Les revêtements TiN hybrides structurés ont été synthétisés, ce qui n'était pas le cas auparavant avec d'autres procédés de projection thermique. Il est connu que la réaction de nitruration se produisait non seulement dans le jet de plasma mais aussi sur le substrat. De plus, avec l'augmentation de la distance de pulvérisation, l'effet de nitruration a été affaibli et la structure hybride du revêtement de TiN a changé de laminaire dense en colonne poreuse, en fonction du degré de vaporisation supérieur, de la concentration de réactive inférieure et du substrat plus froid.. Néanmoins, ils ont également permis d'améliorer les propriétés mécaniques du substrat Ti-6Al-4V.

Mots-clés: Projection plasma en suspension à basse pression; Projection de plasma réactive à basse pression; Torche à plasma bi-cathode axiale; Revêtement de zircon stabilisé à l'yttria; Revêtement de nitrure de titane.

SPIM

■ École doctorale SPIM - Université de Technologie Belfort-Montbéliard
F - 90010 Belfort Cedex ■ tél. +33 (0)3 84 58 31 39
■ ed-spim@univ-fcomte.fr ■ www.ed-spim.univ-fcomte.fr

